The multi-wavelength properties of galaxies embedded in the Cosmic Web

Dane Kleiner

Supervisors:

Dr. Kevin A. Pimbblet

Dr. D. Heath Jones

Dr. Bärbel S. Koribalski

MONASH University Science   CSIRO

"From there to here, and here to there, funny things are everywhere."

– Dr. Suess

"You win again, gravity!"

– Zapp Brannigan

Acknowledgments

First and foremost I would like to thank Kevin Pimbblet, Heath Jones and Bärbel Koribalski for shaping me into the astrophysicist I am today. I am grateful for their supervision, encouragement and mentoring as well as pushing me when needed and asking the challenging questions throughout my PhD. I would also like to thank Matt Owers and Paolo Serra, who proved to be valuable collaborators that contributed essential research and insight to my work.

I would personally like to thank the friends that I have made on this journey, particularly Jake Crossett, Amelia Fraser-McKelvie, Tim Dolley, David Palamara and Nic Bonne as I was lucky enough to share an office with them. They provided a stellar environment for bouncing ideas off each other and never turned down an offer of much needed distraction or procrastination. There are too many friends that I have made during my candidature to list, but thank you for being a part of it, you know who you are.

I treasure the support from family, especially my mother, father and sister who always took an interest in what I was doing. I would also like to thank my Dragon, Nero, for walking across my keyboard at the most inconvenient times.

Lastly, I am grateful beyond measure to my partner Caroline Luchow. Thank you for being by my side through this difficult journey, I appreciate the countless support in its many forms you have given me.

I am humbled by the marvels and mysteries of the Universe. I am grateful that I am one of the lucky few who are trying to unravel and understand its secrets...

Monash University
General Declaration

I hereby declare that this thesis contains no material which has been accepted for the award of any other degree or diploma at any university or equivalent institution and that, to the best of my knowledge and belief, this thesis contains no material previously published or written by another person, except where due reference is made in the text of the thesis.

This thesis includes two original papers published in peer reviewed journals, respectively entitled:

'Photometric studies of Abell 1664: The subtle effect a minor merger has on cluster galaxies' (Kleiner et al., 2014) and

'Evidence for H I replenishment in massive galaxies through gas accretion from the cosmic web' (Kleiner et al., 2017).

The core theme of the thesis is to constrain the mechanisms that regulate galaxy transformations in a cosmological framework. The ideas, development and writing of all papers in the thesis were my responsibility, the student, working within the School of Physics and Astronomy under the supervision of Dr. Kevin A. Pimbblet, Dr. D. Heath Jones and Bärbel S. Koribalski at the CSIRO Astronomy and Space Science division.

In the case of Chapter 2 and 4 my contributions to the work involved the following:

The writing of the publication, the sample selection, analysis, and all other work contained therein (which is not referenced), excepting collection of the survey data and development of the data products that were used such as: photometry, redshifts, and spectroscopy. I have renumbered sections, equations and figures of the published paper in order to generate a consistent presentation within the thesis.

Candidate's Signature:

Date: May 23, 2017

ABSTRACT

There are many factors that shape the evolution of a galaxy. One recent experimental proposal is to determine if galaxies interact with the baryons of the cosmic web. If detectable, the interactions could lead to gas accretion or star formation quenching and would need to be incorporated into a fuller prescription for galaxy evolution. In this thesis, we use multi-wavelength data to search for evidence of galaxies interacting with their cosmological environment in order to explain their observable properties starting with galaxy clusters and proceeding to filaments of galaxies.

We show a higher fraction of morphologically disturbed galaxies reside in the inner, dense region of Abell 1664. Using 2D adaptive smoothing techniques, we find significant substructure that is most likely the remnant core of a merging group that has been responsible for triggering a cold front in the cluster core. Radial colour profiles with BRI photometry and blue fractions show the cluster galaxies to be consistent with the morphology-density relation. We conclude the star formation of all cluster galaxies, including the merging group, has been quenched. The favoured scenario is pre-processing of the merging group, where star formation is quenched prior to interacting with the cluster galaxies.

We present two mock catalogues of the 6 degree Field Galaxy Survey (6dFGS) for calibrating the parameters required to create a group and filament catalogue. We measure the projected clustering and find the Sub Halo Abundance Matching (SHAM) mock underestimates the clustering at all scales, turning over at a projected distance of 0.3 Mpc h^{-1}. The Semi-Analytic Galaxy Evolution (SAGE) mock has excellent agreement with the 6dFGS projected clustering up until 0.3 Mpc h^{-1}, where it turns over and underestimates the clustering. This highlights important discrepancies between observation and simulation with uncertain origin that we will pursue in future work.

We delineate filaments of the cosmic web in 6dFGS and define filament and non-filament galaxy samples. By stacking HI Parkes All Sky Survey (HIPASS) spectra we contrast the HI-to-stellar mass ratio (HI fraction), fraction of star forming galaxies and Star Formation Rate (SFR)-to-HI mass ratio (star formation efficiency; SFE) of these samples. The effects of stellar mass and projected galaxy density are normalized to disentangle what influences cold gas and star formation quenching in galaxies. We find the fraction of star forming galaxies as a function of projected density to be the same between filament and non-filament galaxies. For galaxies with stellar

mass $\log(M_\star / M_\odot) \geq 11$, filament galaxy H I fractions are systematically higher and SFEs are systematically lower. These trends provide evidence for filament galaxies accreting cold gas from the intergalactic medium (IGM) that is too diffuse to collapse into stars without an external mechanism.

We propose a scenario where galaxies attached to cosmic web filaments can accrete cold gas from the IGM. The gas only forms stars with an external trigger, such as strong tidal interactions, resulting in a brief starburst similar to those observed in filaments feeding clusters. This can explain galaxy pre-processing in groups prior to entering clusters. The interactions would detach the galaxy from the cosmic web and ultimately quench its star formation.

Table of Contents

List of Figures

List of Tables

CHAPTER 1

Introduction

In the 1920s when astronomers first realised that the faint 'nebulae' observed in the night sky were other galaxies beyond the Milky Way, their differing shapes raised immediate questions about their origins and founded the study for galaxy formation and evolution (e.g. Messier, 1781; Hubble, 1926). Understanding the formation and evolution of galaxies remains a key goal of modern astronomy, where the ultimate aim is to determine the physics that explains the distribution of galaxies and their properties observed throughout the Universe (e.g. Committee for a Decadal Survey of Astronomy and Astrophysics, 2010; National Committee for Astronomy, 2016).

The majority of galaxies can be classified into two broad populations – spiral (disc or late type) and elliptical (or early type) (e.g. Wolf, 1908; Reynolds, 1920; Hubble, 1936). Spirals contain a thin disc, are typically gas rich, blue in colour and forming new stars. Ellipticals have no obvious structure, are typically gas poor, red in colour with little or no star formation.

The current consensus in the literature is that the mass and immediate environment of a galaxy are responsible for the physics that drives these two populations (e.g. Balogh et al., 2004; Kauffmann et al., 2004; Baldry et al., 2006; Poggianti et al., 2006; Park et al., 2007; Bamford et al., 2009; von der Linden et al., 2010, and references within). However, there are many pathways a galaxy can take in its evolution and the complexities of these pathways mean that not all galaxies fit into these two populations neatly. Additional factors and variables are required to explain the full distribution of galaxies and their properties.

The relation between a galaxy and its cosmological environment (i.e. its location in the cosmic web) has been largely overlooked in galaxy evolution. One of the key questions this thesis addresses is whether galaxy position within the cosmic web is required in addition to mass and immediate environment to explain the observed properties of galaxies.

To understand the complexities surrounding the issue, it is necessary to give an overview of the cosmological framework of the Universe, the Lambda Cold Dark Matter (ΛCDM) formalisation. This is provided in the next section and followed up by the remaining chapters (1.2 to 1.5) to explore the shortcomings of ΛCDM.

1.1   A Cold Dark Matter Universe

The properties of present day galaxies are due to processes that started with the formation of the very first protogalaxies. The ΛCDM cosmology is the well-accepted framework for galaxy formation and evolution. This paradigm invokes a Universe consisting of non-relativistic cold dark matter, baryonic matter, radiation and dark energy (e.g. Blumenthal et al., 1984; Komatsu et al., 2011). In the epoch of inflation, small density perturbations in the matter distribution grow through the gravitational build up of dark matter haloes over cosmic time. Within a ΛCDM cosmology, dark matter and thus baryonic matter follow hierarchical 'bottom-up' formation (White & Rees, 1978). Dark matter haloes grow by merging with other dark matter haloes. During this process, gas accretes into the gravitational potential of the halo and with efficient cooling, the gas collapses to form the earliest stars. These stars merge and form a disc that spins up to conserve angular momentum (Springel et al., 2005a). The hierarchical processes continue such that dark matter halos (and the galaxies contained within them) build mass over cosmic time. A cartoon depicting the main steps of hierarchical formation is shown in Fig. 1.1. The matter distribution traces the dark matter distribution and forms a cosmic web with galaxy clusters at the nodes, connected by filaments that circumvent voids.

Hierarchical formation and evolution provides a solid platform that explains how dark and baryonic matter interact in the Universe and is able to explain how disc galaxies merge to form massive ellipticals. While this broadly describes the evolutionary path for galaxies, there are significant shortcomings where additional baryonic physics is required to reproduce the observed properties of galaxies. One fundamental example is the luminosity function (LF) that describes the number of galaxies per unit volume in a luminosity interval (Press & Schechter, 1974; Schechter, 1976). Hierarchical formation and evolution overproduces the number of star forming galaxies and mechanisms that prevent or suppress star formation need to be incorporated to reproduce the observed luminosity functions (e.g Silk, 2011; Silk & Mamon, 2012). We first link the physics that drives the observable properties of galaxies (Chapter 1.2) and later
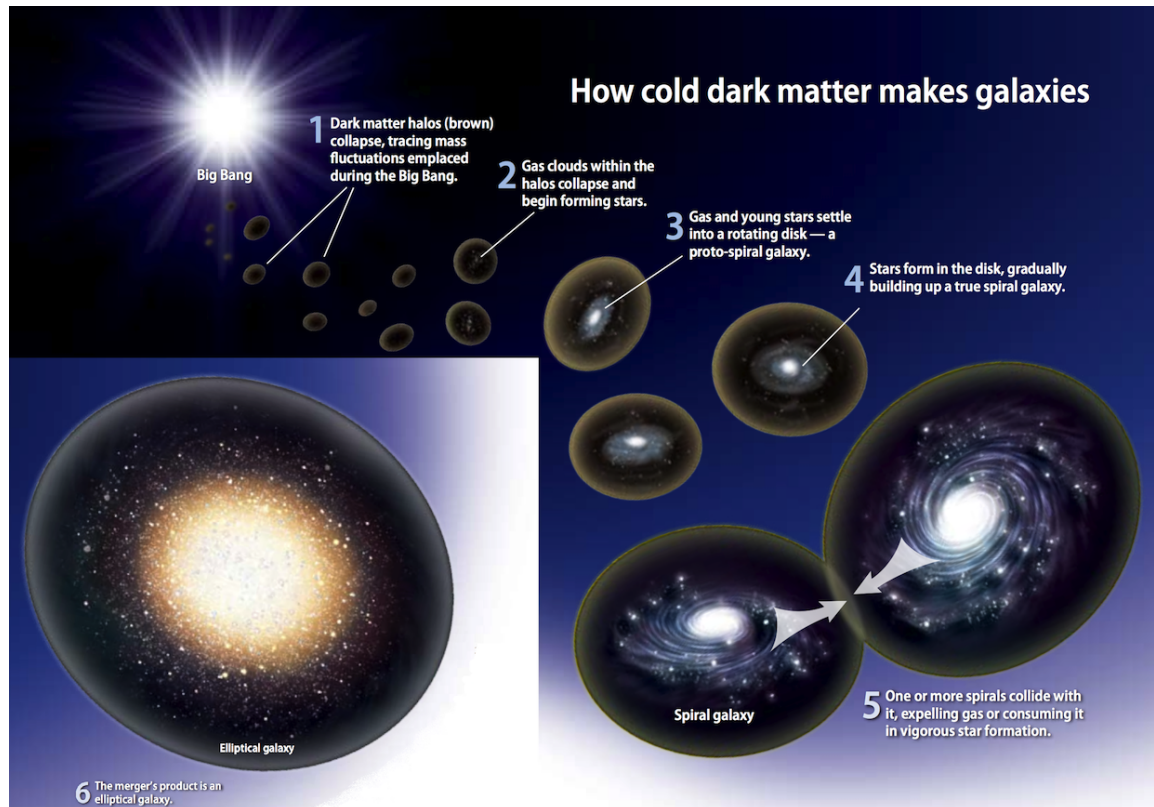
Fig. 1.1: A cartoon showing the main steps of hierarchical formation in the ΛCDM Universe. Initially, small dark matter halos form and accrete gas that form the first stars. Due to the conservation of angular momentum, the protogalaxies rotate and the continual accretion of gas forms a disk. Over time, these halos (and galaxies contained within them) merge to form more massive halos that result in the galaxies observed at $z \sim 0$. Image credit: Roen Kelly, http://www.astronomy.com/.

explore the physical processes beyond hierarchical formation and evolution required to describe galaxy evolution (Chapter 1.3).

1.2 Observable properties of galaxies

Commonly measured properties of nearby galaxies include: morphology, colour, mass both of gas and stars, velocities including rotation, dispersion and peculiar, and star formation rate (SFR). Determining meaningful or natural correlations between these properties gives insight to the physics responsible for the observations and allows us to test the physics that drives galaxy evolution. The observed correlations does not necessarily mean causation and connecting the physics to the correlations underpins our understanding of galaxy evolution. In the subsections below, we detail the main observations of galaxies used describe their evolutionary pathways.

1.2.1 Galaxy morphology and colour

Formal optical classifications schemes of galaxy morphology began with the Hubble tuning fork (Hubble, 1936) and refined by de Vaucouleurs (1959) (Fig. 1.2). The Hubble classification identifies two main groups: elliptical and spiral. Ellipticals have spheroidal shapes and are numbered according to axis ratio (E0 for spherical to E7 for elongated). Spirals have a central bulge and disc. The spirals are further split into two sub-classes based on the presence of a bar (B). All spiral galaxies are classified by the size of the bulge and how tightly wound the spiral arms are (with 'a' as the tightest and 'd' as the loosest). Lenticular (S0) galaxies reside between ellipticals and spirals with a disc but no spiral structure. Any galaxy that could not be classified into these categories was considered to an irregular (Irr) galaxy. The Hubble classification scheme is still used today, although it is over simplified given the more recent quantitative approaches to classify galaxy morphology.

In the modern era of supercomputers and machine learning algorithms, reliably classifying galaxies using visual schemes (e.g. Hubble, 1936; de Vaucouleurs, 1959) presents a significant challenge. The differences between the subdivisions is most reliably achieved by the human eye, however, this technique is subjective and lacks quantification. The single biggest limitation is inclination, which can render important features such as spiral arms unseen. It is also impractical for large galaxy samples,
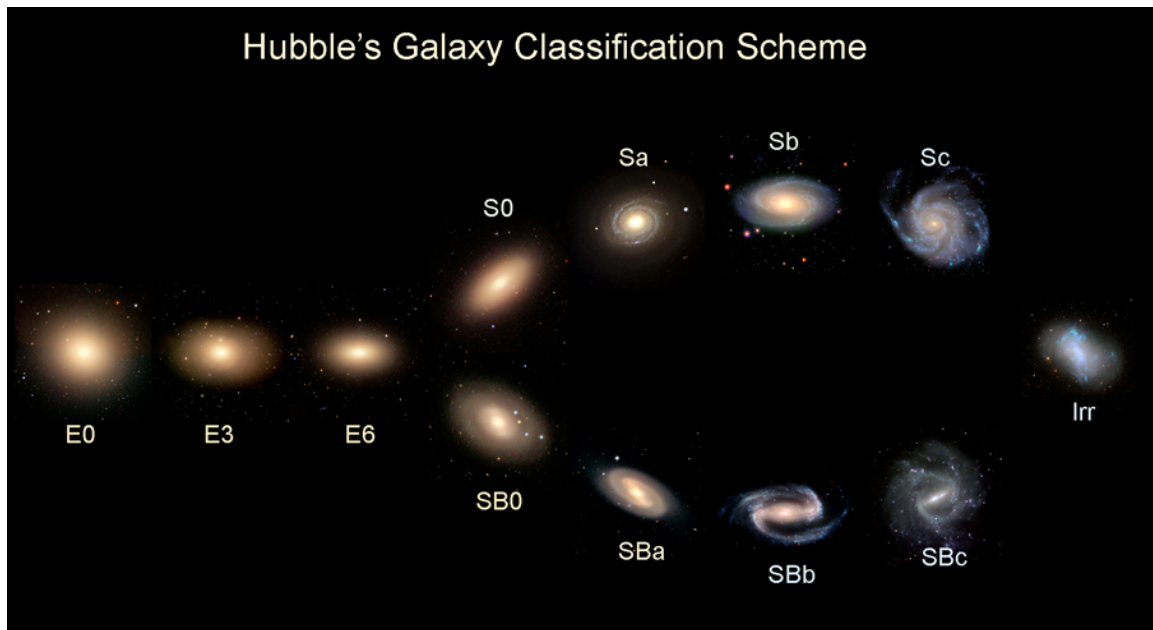
Fig. 1.2: A modern revision of the Hubble tuning fork (Hubble, 1936). The classification is separated in two main groups; early-type elliptical (E) galaxies and late-type spiral (S) galaxies. Galaxies that did not fall into these groups were considered irregular (Irr). The ellipticals are classified in accordance with its ellipticity and spirals are classified by the presence of a bar, the size of its bulge and how tightly wound the spiral arms are (http://www.pics-about-space.com/).

unless large numbers of classifiers are used (e.g. Galaxy Zoo[1]; Lintott et al., 2008), which in turn compromises consistency.

A quantitative alternative to visual morphological classification for galaxy samples is the Sérsic index, n, which models the surface brightness as a function of radius, $I(R) \propto e^{Rn^{-1}}$ (Sérsic, 1963). Surface brightness profiles with n=1 correspond to disc dominated galaxies and n=4 trace the bulge dominated (i.e. elliptical) galaxies. The Concentration-Asymmetry-clumpinesS (CAS; Abraham et al., 1994; Conselice, 2003), second order moment of brightness (M_{20}) and Gini (G) (Gini, 1912; Lotz et al., 2004) method extends this idea by using parameters to quantify morphology. The CAS, M_{20} and Gini system are used in Chapter 2.3.2 and we describe the features of each morphological parameter.

Fig. 1.3 displays the processes used to measure the CAS parameters from Conselice (2003). Concentration is the ratio of light enclosed in the $80\% - 20\%$ curve of growth radii. It is useful for distinguishing elliptical (high concentration) and disc (low concentration) galaxies however it utilises a circular aperture to measure the galaxy flux, making it unsuitable for irregular galaxies. Asymmetry is defined as the residual flux of a galaxy that has been rotated 180° and subtracted from the original image. It is best at identifying irregular and interacting galaxies. Clumpiness is defined as the ratio of the light contained in high frequency structures to the total amount of light in the galaxy. It is computed by subtracting a smoothed version of the galaxy from the original image. Clumpiness is able to extract the irregular substructure contained within galaxies (i.e. knots of star formation) but is highly sensitive to the chosen smoothing length (B in Fig. 1.3). M_{20} is similar to the concentration index but does not impose circular symmetry and therefore is more sensitive to merger signatures such as multiple nuclei. The Gini coefficient quantifies the relative distribution of flux within the pixels associated with a galaxy. It also correlates with the concentration index, but unlike the latter, it does not assume that the brightest pixels are in the geometric centre of the galaxy.

Galaxy morphology plays an important role in revealing signatures of morphological transformation, dynamical state and recent interaction history. However, it is insufficient to understand all the processes that can transform a galaxy. The properties of the stellar population, age and metallicity, gas and star formation activity (past and present) are also key for deducing if any evolution is happening.

---

[1]https://www.galaxyzoo.org/

$$A = \frac{abs(I-R)}{I}$$

$$S = \frac{I-B}{I}$$

$$C = 5 \log(\frac{r_{80}}{r_{20}})$$
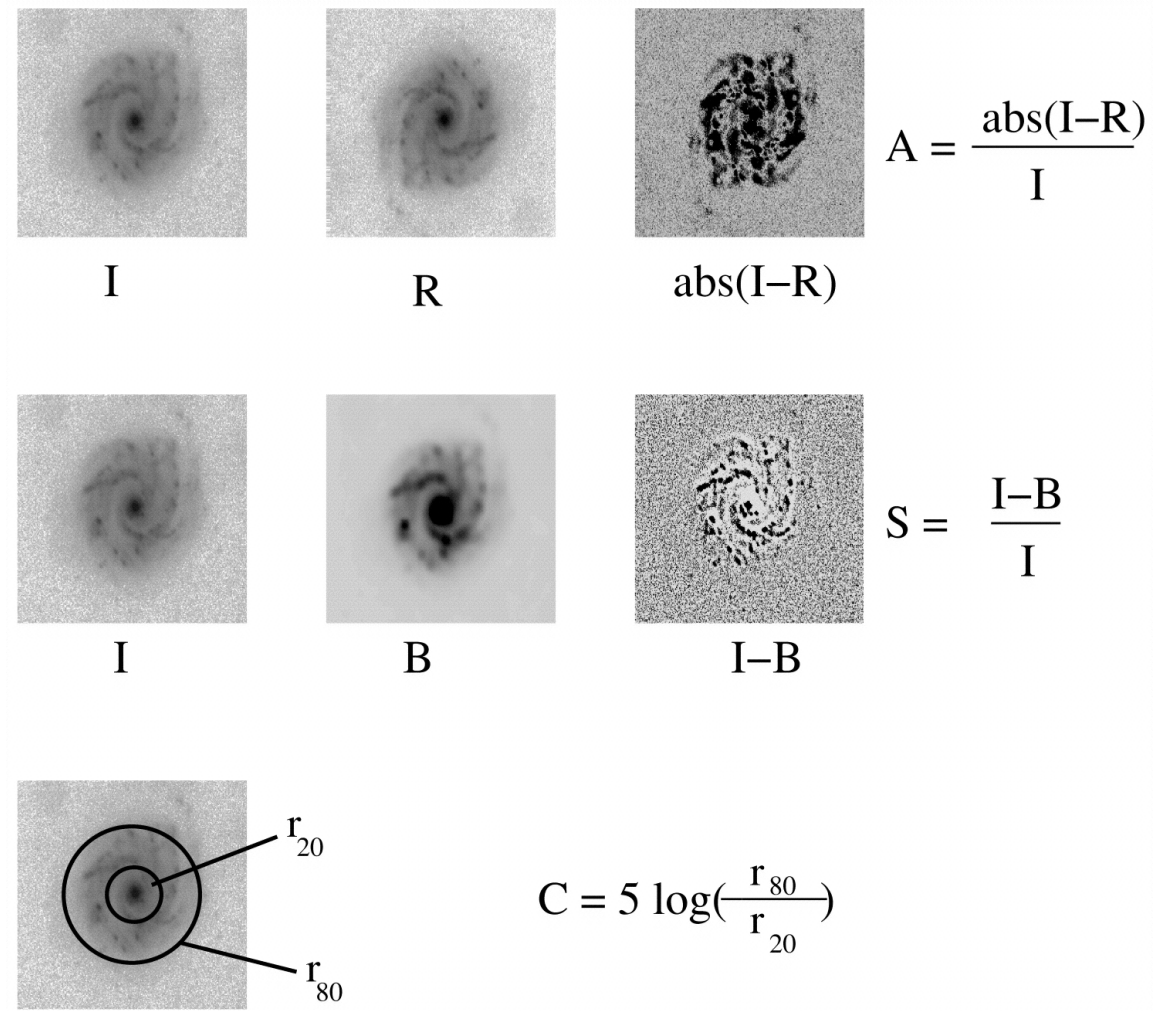
Fig. 1.3: The processes defined in Conselice (2003) showing how the Asymmetry (A), clumpinesS (S) and concentration (C) are measured. To measure the asymmetry, the original galaxy image (I) is rotated 180° (R) and subtracted to reveal any asymmetric features in the residual image (right panel). To measure the clumpiness, the original image (I) is smoothed (B) and any clumpy regions (e.g. knots) will be revealed in the residual image (right panel). The concentration is defined by the light measured at 20% and 80% as shown by the two circles. These parameters are used to search for signatures of recent interactions or morphological transformations.

Rest frame stellar emission is strongest in the near infrared (NIR), optical and ultraviolet (UV) wavelengths. The peak wavelength is a function of the stellar mass, age and star formation activity in the galaxy (e.g. Kauffmann et al., 2003; Bruzual & Charlot, 2003; Taylor et al., 2011). Galaxy colour is a proxy for SFR and is correlated with mass, morphology and local environment (e.g. Faber et al., 2007). The local/immediate environment of a galaxy can be thought as a nearby galaxy density and we discuss the details in Chapter 1.3.2. The generalisation of passive, red early-type galaxies and active, blue late-types arise from observations of their stellar population. Hot, high mass (O and B type) stars are short lived and predominately emit blue and UV photons. Hence blue galaxies (typically late types) signify on-going star formation in the galaxy. Conversely, cooler, low mass (K and M type) stars with long lifetimes predominately emit red and NIR photons, indicative of no current star formation. The relation between galaxy morphology and colour gives rise to the colour bimodality that most galaxies generally adhere to (e.g. Baldry et al., 2004; Brammer et al., 2009).

Galaxy colour-magnitude relations (CMR) exhibit a colour bimodality of a narrow 'red sequence' and broader 'blue cloud' (Fig. 1.4; Visvanathan & Sandage, 1977). Galaxies are also found in a third region known as the 'green valley' (Fig. 1.4), believed to be a transition region for galaxies quickly moving from blue to red (e.g. Bell et al., 2004; Wyder et al., 2007; Schiminovich et al., 2007; Faber et al., 2007; Mendez et al., 2011; Schawinski et al., 2014).

The CMR (specifically the red sequence) has been measured out to very high redshifts and to produce the CMRs observed at $z \sim 0$, galaxy colour must have evolved as a result of continual star formation at fixed mass (e.g. Noeske et al., 2007). Over cosmic time, the bulk of star formation occurs in progressively lower mass galaxies, a phenomenon known as "downsizing" (Cowie et al., 1996).

Modern galaxy surveys have furnished colours for large galaxy samples that have successfully enabled a deeper understanding of the bimodal colour distribution (e.g. Hogg et al., 2003; Baldry et al., 2004, 2006; Balogh et al., 2004; Faber et al., 2007). They have revealed that morphology does not necessarily correspond with galaxy colour (e.g. Schawinski et al., 2014). As shown in Fig. 1.4, when separated by morphology, there is a significant portion of early-type galaxies that populate the blue cloud and vice versa. Multiple studies have confirmed the presence of galaxies that do not conform to early-type late-type colour bimodality such as blue ellipticals (e.g. McIntosh et al., 2014; Taylor et al., 2015) and red spirals (e.g. Masters et al., 2010;
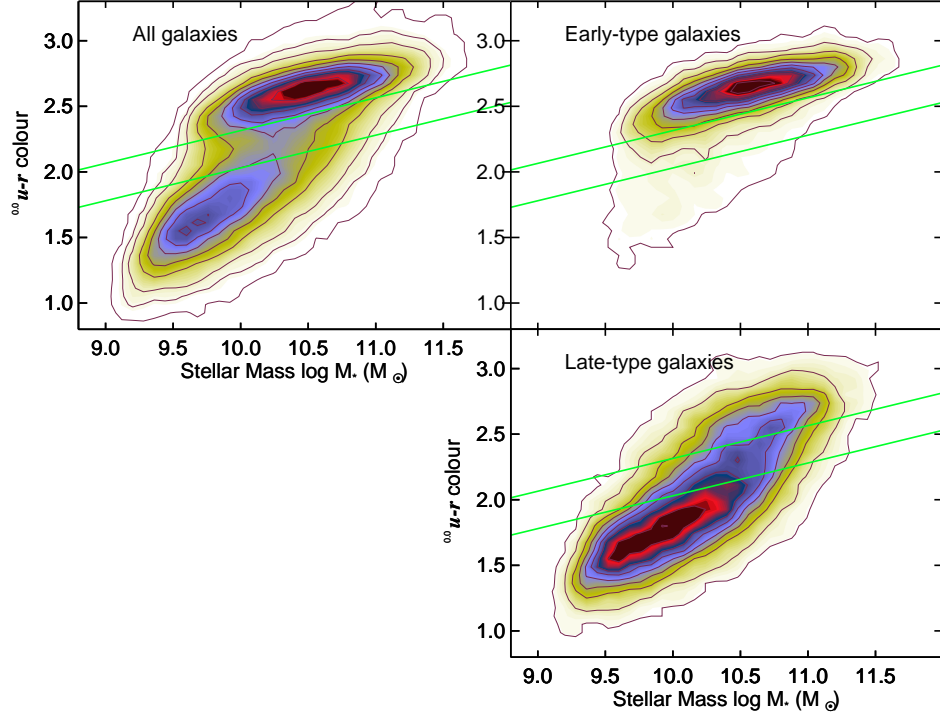
Fig. 1.4: The colour-mass (equivalent to colour-magnitude) relation from Schawinski et al. (2014) for all galaxies in the sample (top left), early-types (top right) and late-types (bottom right). The blue cloud, red sequence and green valley are clearly distinguishable for the full galaxy sample. The early types dominate the red sequence but also spill into the blue cloud and the late types mostly reside in the blue cloud but a significant fraction float up into the red sequence. This demonstrates that generally colour bimodality is a produce of morphological type. However, it does not hold true for all galaxies and there are many complex paths a galaxy can take through its evolution.

Fraser-McKelvie et al., 2016). The current consensus is that the majority of galaxies move from the blue cloud to the red sequence via the green valley through multiple evolutionary channels (e.g. Schawinski et al., 2014; Taylor et al., 2015). For example, it is possible for a blue galaxy to have its star formation quenched (and so reddens) without disturbing its morphology, just as it is possible for a blue galaxy to undergo a morphological transformation without a significant change in colour (e.g. Faber et al., 2007; Mutch et al., 2011; Taylor et al., 2015). In order to make sense of the star formation history of an individual galaxy through its galaxy colours, we must first understand the gas supply and gas reserves of the galaxy (e.g. Schawinski et al., 2014).

1.2.2   HI gas and star formation

Neutral hydrogen (HI) is the building block for matter to collapse into stars and is largely responsible for stellar mass growth. Dense concentrations of HI gas can condense into massive molecular clouds that collapse and form stars. This provides an inextricable link between the HI content and star formation of the galaxy. Simply put, galaxies rich in HI have the ability to form new stars continually while these conditions exist and galaxies without HI can not (e.g. Doyle & Drinkwater, 2006; Fabello et al., 2011a; Catinella et al., 2010, 2013; Cortese et al., 2011; Brown et al., 2015; Dénes et al., 2014, 2016).

HI is the neutral atomic hydrogen gas traced via the 21-cm spectral line, resulting from the spin flip of the electron in the hydrogen atom. The main component of the molecular clouds that collapse into stars is molecular hydrogen (H_2), although it is not directly detectable in its cold state. The carbon monoxide molecule (CO) is directly detectable and traces H_2 regions, however there is only 1 CO molecule for every $\sim 10^4$ H_2 molecules. Therefore, HI is the most abundant and preferred tracer of cool gas in galaxies. It is critical to measure the HI content in galaxies if we are to formulate a theory of galaxy evolution.

HI in galaxies extend to larger radii (typically 2-3 times but up to 6) than the stellar population making it useful for tracing the dynamical history of the galaxy, measuring rotation curves and total dark matter content (e.g. Warren et al., 2004). HI is a powerful probe of the interaction between a galaxy and its environment as HI is more easily disrupted (than stars) from tidal interactions and can display a disturbed morphology long after the initial disruption (e.g. Koribalski & Dickey, 2004; Holwerda
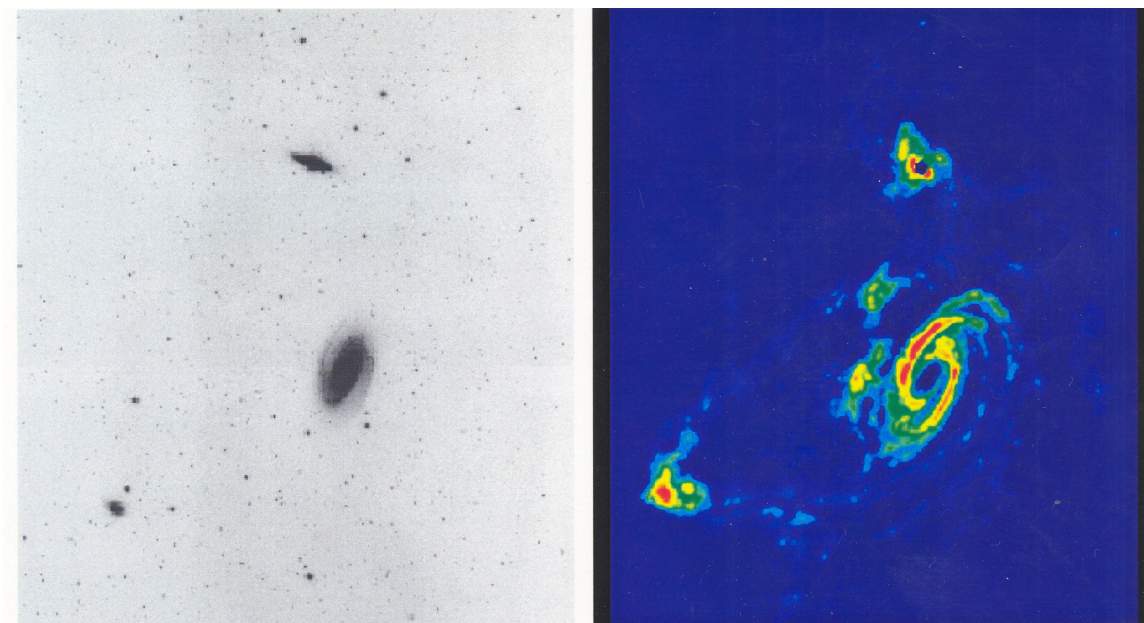
Fig. 1.5: A comparison of the optical emission from the stellar population (left) and the H I emission (right) in the M81 group, adapted from Yun et al. (1994). There is no evidence of interactions between the galaxies in the optical image. However, the H I emission extends far beyond the optical disk and clearly shows interaction between the galaxies via tidal tails and bridges.

et al., 2011). An excellent example of this can be seen in Fig. 1.5 that highlights the difference between the stellar and H I emission in the M81 group.

The H I mass of a galaxy generally correlates with the morphology, colour and star formation activity of the galaxy. H I rich galaxies are typically star forming late-types that are blue in colour (e.g. Gouguenheim, 1969; Gallagher, 1972; Rogstad & Shostak, 1972; Roberts & Rots, 1973; Knapp et al., 1978). Traditionally, early-type galaxies were thought to be completely devoid of H I but recent works have shown that significant H I (sometimes in a disc) can be detected with column densities $n_{HI} < 10^{20}$ cm^{-2} (Serra et al., 2012; Young et al., 2014).

The H I content of a galaxy is related to its stellar mass and immediate environment (e.g. Giovanelli & Haynes, 1985; Chung et al., 2009; Kilborn et al., 2009; Cortese et al., 2011; Serra et al., 2012; Rasmussen et al., 2012b; Catinella et al., 2013; Hess & Wilcots, 2013). Massive galaxies have deep potential wells that enable them to retain more H I than their less-massive counterparts. Low density environments (such as isolated galaxies and loose galaxy groups) are known to contain H I rich galaxies, as opportunities to be dynamically disturbed are rare. H I poor galaxies arise through

the gas being stripped or heated via a variety of interactions (as discussed in chapter 1.3.3). These factors result in galaxies with H<small>I</small> masses ranging between $10^5 - 10^{11}$ M$_\odot$ defining the H<small>I</small> mass function (e.g. Zwaan et al., 2005) where galaxy H<small>I</small> mass span several orders of magnitude for a given stellar mass (Maddox et al., 2015). The H<small>I</small>-to-stellar mass ratio (H<small>I</small> fraction) strongly anti-correlates with stellar mass and weakly anti-correlates with local galaxy density (e.g. Baldry et al., 2008; Catinella et al., 2010; Cortese et al., 2011; Brown et al., 2015, 2016).

This thesis uses the H<small>I</small> mass and subsequent H<small>I</small> fraction of galaxies to search for evidence of H<small>I</small> replenishment in galaxies through accreting cold gas from filaments. This tests the connection between galaxies and the intergalactic medium (IGM) in a cosmological framework. Spectral stacking provides a statistical detection of the average H<small>I</small> content of galaxies without relying on direct detection. It is being used more frequently in large H<small>I</small> surveys such as the H<small>I</small> Parkes All Sky Survey (HIPASS – Staveley-Smith et al., 1996; Barnes et al., 2001) and the Arecibo Legacy Fast ALFA survey (ALFALFA – Giovanelli et al., 2005). Stacking provides superior signal-to-noise and enables the detection of H<small>I</small> at redshifts inaccessible to a current individual spectrum (e.g. Lah et al., 2007, 2009; Pen et al., 2009). This technique will play a vital role in measuring the H<small>I</small> content of galaxies with the Australian Square Kilometre Array Pathfinder (ASKAP – Johnston et al., 2008; Hotan et al., 2014) and the Karoo Array Telescope (MeerKAT – Jonas, 2009), and their surveys such as the Widefield ASKAP L-band Legacy All-sky Blind surveY (WALLABY – Koribalski, 2012) and the Deep Investigation of Neutral Gas Origins (DINGO).

The star formation in a galaxy gives a present-day snapshot of how rapidly the gas is processed into stars (e.g. Tinsley, 1968; Searle et al., 1973; Sandage, 1986; Kennicutt, 1998; Heavens et al., 2004; Noeske et al., 2007). Hot, high mass stars are short lived (< 100 Myr) and their presence in a galaxy indicates there is (or recently was) sufficient cold gas to sustain the star formation process.

Given the direct link between H<small>I</small> and SFR, it is not surprising that the SFR correlates with the same properties (morphology, colour and H<small>I</small> mass). Star forming galaxies are typically H<small>I</small> rich late-types that are blue in colour (e.g. Sandage, 1986; Kennicutt et al., 1994; Kennicutt, 1998). Furthermore, SFR is connected to the stellar mass and immediate environment of the galaxy (e.g. Park et al., 2007; Bamford et al., 2009; von der Linden et al., 2010; Evoli et al., 2011; Lemonias et al., 2013; Lin et al., 2016). The deep potential well of massive galaxies enables them to form and retain more stars. Low density environments usually preserve the discs of star forming galaxies

by minimising dynamical interactions (as discussed in chapter 1.3.3). The SFR-to-stellar mass ratio, also generally known as the specific star formation rate (SSFR), is a direct way of comparing the SFR of galaxies with different stellar masses and is useful for revealing weaker environmental trends that can affect the SFR of a galaxy.

There exist a variety of photometric and spectroscopic measures to estimate SFR. These include the stellar continuum in the UV rest frame (Calzetti, 2013) as well as spectroscopic measurements of Hα and [OII]. UV photons can be largely attenuated by dust, introducing significant scatter in UV derived SFRs (e.g. Kennicutt, 1998; Hopkins et al., 2003; Salim et al., 2007).

In the case of Hα and [OII] emission, UV photons from hot massive stars ionise the surrounding molecular material (i.e. H$_2$) that recombines to emit the Hα spectral lines. Only OB stars with masses > 10 M$_\odot$ can produce these ionising UV photons and survive for < 20 Myr making this SFR indicator a good measure of current star formation. Many Hα and [OII] SFR calibrations have been presented although the Hα and [OII] photons also experience attenuation from dust (e.g. Kennicutt et al., 1994; Madau et al., 1998; Calzetti, 2001; Hopkins et al., 2003).

In contrast, radio continuum emission can be used to estimate SFRs and is unattenuated by dust. It is detected from thermal bremsstrahlung radiation originating from hot young stars ionising H$_2$ regions and non-thermal synchrotron emission originating from cosmic rays accelerating around the magnetic field of a galaxy. Non-thermal emission is responsible for 90% of radio continuum flux at 1.4 GHz (Condon, 1992) and the direct correlation with IR luminosity enables SFRs to be estimated that is typically sensitive to ~ 50 Myr timescales (e.g. Bell et al., 2003).

Furthermore, the SFR that can be estimated from mid-IR emission is largely unaffected by dust attenuation. The UV photons from the young, hot OB stars is often absorbed by the surrounding H$_2$ that is heated and emits thermal mid-IR photons. Polycyclic aromatic hydrocarbons (PAHs) are present throughout the region that hot young stars cause photodissociation and also emit at mid-IR wavelengths (Tielens et al., 2004). This SFR indicator is sensitive on the order of ~ 100 Myr.

These far infrared regions are only accessible from above the atmosphere of the Earth. The Wide-Field Infrared Survey Explorer (WISE – Wright et al., 2010) space mission surveyed the whole sky in four infrared bands (W1-W4) centred on 3.4, 4.6, 12 and 22 μm. The 12μm (W3) band covers the optimal wavelength range to detect the warm H$_2$ and PAH emission from nearby galaxies. SFRs using the W3 band are estimated
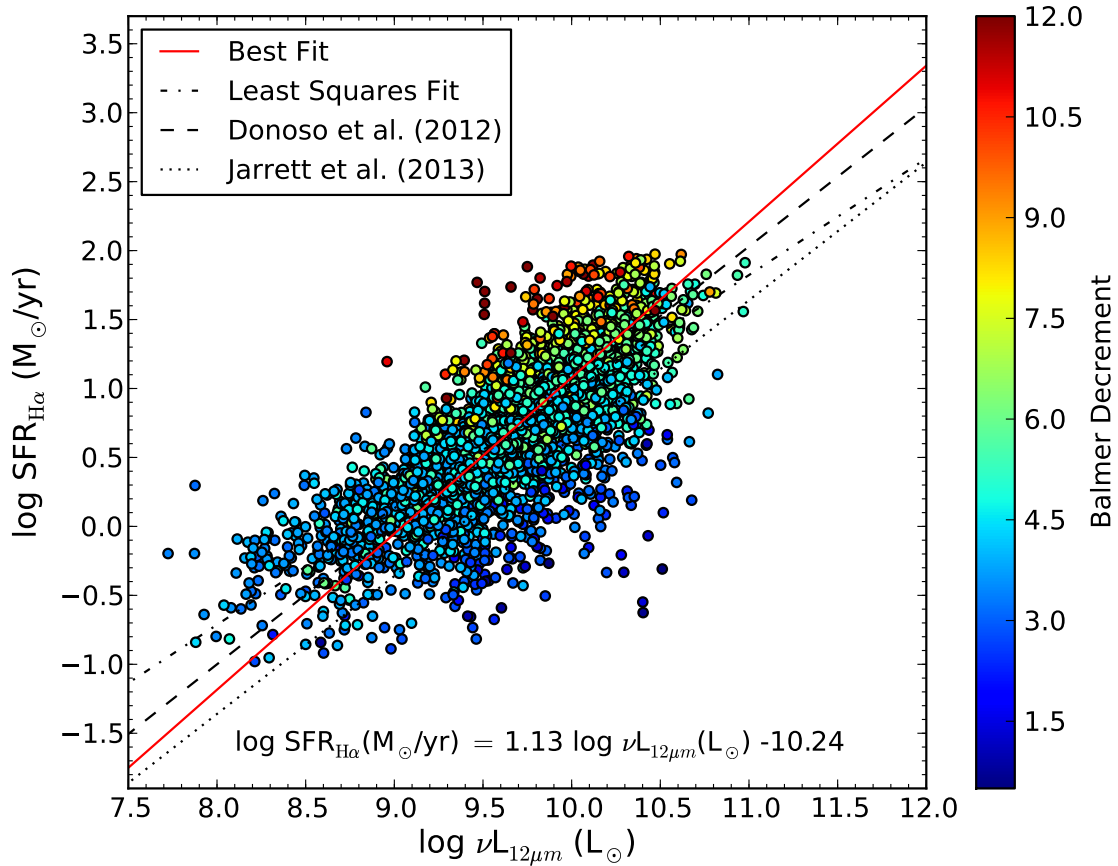
Fig. 1.6: The W3 (12 μm) SFR relation as estimated by Cluver et al. (2014). The relation was achieved by calibrating the W3 luminosities with the Hα SFRs measured by Gunawardhana et al. (2013). There is significant scatter in this relation that may be a result of undesired mid-IR photons from old stars or the presence of strong PAH emission lines.

in Cluver et al. (2014) by calibrating to Hα SFRs derived from Gunawardhana et al. (2013). The W3 SFR relation of Cluver et al. (2014) can be seen in Fig. 1.6 and there is significant scatter in the SFR relation. This scatter may originate from the old (i.e. red giant) stellar population contributing mid-IR photons (Sauvage et al., 2005) and strong PAH emission lines (e.g. Smith et al., 2007; Jarrett et al., 2013).

Not all SFR indicators are equal. While all the estimates directly or indirectly measure the SFR, they trace different physical mechanisms. This makes them sensitive to star formation on different time scales where the origin of the scatter and uncertainty in the estimates arise from different phenomena (Davies et al., 2015). An important part of this thesis is to estimate SFRs to measure the SSFR and star formation efficiency (SFE) for galaxies. We achieve this in Chapter 5, where we use the WISE

W3 SFR indicator ([Cluver et al., 2014](#)) to estimate these quantities and search for evidence that galaxies in filaments are having their star formation regulated.

Measuring SFRs (or some proxy of) has been a key constraint on the build up of stellar mass through galaxy evolution. It traces an underlying physical process that can be used to understand the current state and ultimate fate of a galaxy. Eventually, all galaxy star formation will be quenched. Determining how and when quenching occurs are two of the most important questions in galaxy evolution.

1.3 Galaxy evolution

Galaxy evolution is a complex process as many physical mechanisms are thought to play a (frequently simultaneous) role. These corresponding contributions to galaxy transformations are relatively unconstrained, and can operate on fast or slow timescales and be internal or external to the galaxy. A summary of a number of these processes and how they relate to each other is shown in Fig. 1.7 (adapted from Kormendy & Kennicutt, 2004).

Of these, mass and environment are thought to be the two primary drivers of galaxy evolution (e.g. Balogh et al., 2004; Kauffmann et al., 2004; Baldry et al., 2006; Poggianti et al., 2006; Park et al., 2007; Bamford et al., 2009; von der Linden et al., 2010; Pimbblet & Jensen, 2012; Alpaslan et al., 2015). Using Integral Field Units (IFUs) to measure the internal kinematics of galaxies, recent studies have found that mass and angular momentum are primary drivers of galaxy evolution where the scatter in the correlations relate to the galaxy's optical morphology (e.g. Cortese et al., 2016; Lagos et al., 2017; Swinbank et al., 2017). In this thesis, no analysis was conducted using IFUs. Therefore we have refrained from speculating on any direct connection to angular momentum and concentrate specifically on mass and environment.

Neither mass nor environment are not separate from each other as galaxy mass (and its growth) depend on its environment. In the following sections, we describe those processes most relevant to the work of this thesis.

1.3.1 Stellar mass growth and regulation

Galaxies grow in stellar mass by increasing their stellar populations, either through processing cold gas through new star formation, or gravitational capture of stars
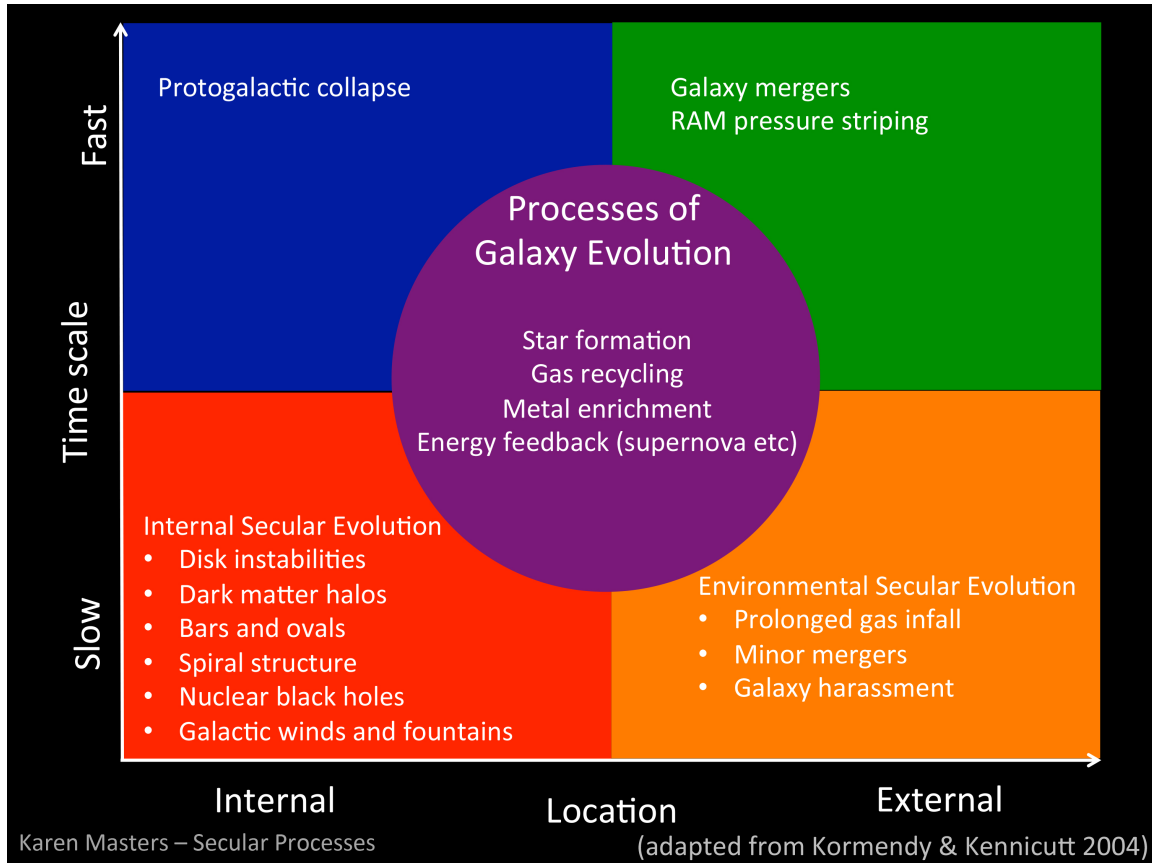
Fig. 1.7: A summary of the galaxy evolution processes, how they work together and on what timescale, modified from Kormendy & Kennicutt (2004). The processes that contribute to all galaxy evolution are shown in the centre. Internal and external processes to the galaxy are displayed on the left and right. The relative timescale for the processes are shown with slow on the bottom and fast on the top. Image credit: K. Masters from the 'Evolutionary Pathways in Galaxy Morphology' conference (http://gzconf.galaxyzoo.org).

during a galaxy merger. While the rate that galaxies build up stellar mass depends on environment, massive galaxies have large potential wells that host the largest Hɪ mass and produce the highest SFRs. However, internal mechanisms (scaling to galaxy mass) can regulate and prevent star formation. The result is that most massive galaxies are usually the least efficient at converting cold gas to stars.

The characteristic stellar mass of $\sim 3 \times 10^{10}$ M$_\odot$ has been shown to divide galaxies into two groups (e.g. Kauffmann et al., 2003; Peng et al., 2010). Galaxies below this threshold tend to be disc-dominated, with young stellar populations. Galaxies above are bulge dominated with old stellar populations. Hierarchical evolution alone can not explain these differences within typical timescales. Internal mechanisms that regulate star formation have been invoked to account for the differences (e.g. Kauffmann et al., 2003; Peng et al., 2010; Geha et al., 2012).

To reduce the efficiency of stars forming in a galaxy, energy must be injected into the interstellar medium (ISM). This reduces the rate of cold gas accretion or prevents some cold gas collapsing into stars. Supernovae, active galactic nuclei (AGN) and virial shock heating are mass driven effects that contribute to injecting energy into the ISM.

Supernovae in galaxies are an end product of current star formation that can also be responsible for decreasing overall star formation efficiency. They can heat the ISM with shocks and winds that ionise or eject molecular gas, resulting in a decreased SFR of the galaxy (e.g. Kauffmann et al., 1993; Springel & Hernquist, 2003; Croton et al., 2006; Scannapieco et al., 2008). The cumulative energy injected into the ISM from supernova can make an appreciable difference on a galaxy's star formation efficiency but it is not enough to explain the star formation history of the Universe (e.g. Kauffmann et al., 1993; Springel & Hernquist, 2003; Croton et al., 2006).

AGN are powered by accretion-fed supermassive black holes. The radiation emitted from AGN can heat or remove gas in the galaxy, truncating star formation (e.g. Tabor & Binney, 1993; Fabian et al., 1994; Wyithe & Loeb, 2003). AGN feedback occurs in two modes (quasar and radio) and despite radio-mode being less energetic than quasar-mode, it heats the halo gas and prevents it from cooling, cutting off the galaxy's access to star formation fuel (e.g. Tabor & Binney, 1993; Fabian et al., 1994; Fabian, 2012; Croton et al., 2006). AGN feedback scales with galaxy mass and has the power to shut down star formation in massive galaxies completely (e.g. Wyithe & Loeb, 2003; Croton et al., 2006; Fabian, 2012).

In the ΛCDM framework, gas funnelled onto dark matter halos gets shock heated and therefore must cool in order to collapse and form stars (White & Rees, 1978; Fall & Efstathiou, 1980; Birnboim & Dekel, 2003; Kereš et al., 2005, 2009). Shock heating becomes more efficient for high mass halos, making it more difficult for massive galaxies to accrete cold gas to fuel star formation. The shocked gas can still be cooled but the cooling time may exceed the Hubble time and can result in regulated or truncated SFRs (e.g. Dekel & Birnboim, 2006; Cen, 2011).

As galaxies build mass, internal effects from supernovae, AGN and virial shock heating become more efficient at driving galaxy evolution. Working together they are able reproduce the galaxy colour bimodality and SFRs observed in the local Universe. However, they are unable to explain morphological transformations and external environmental mechanisms are required to explain how a spiral galaxy can transform into an elliptical.

1.3.2 The local environment of a galaxy

Through the hierarchical growth of structure in the Universe, we can describe the environment in which a galaxy resides on a range of scales. There are multiple techniques for measuring galaxy environment and there is no universal measure suited to all scales. However, all techniques relate to some measure of galaxy *density* (Muldrew et al., 2012).

It is natural that the evolution of a galaxy will be guided by external mechanisms set by its immediate surroundings. The morphology-density relation discovered by Dressler (1980) found that spiral galaxies preferentially reside in low density environments while elliptical and lenticular galaxies preferentially reside in high density environments. It was proposed that spiral galaxies are transformed into elliptical galaxies as they progress to denser environments (Dressler, 1980). As density correlates with mass, an analogous morphology-mass relation can be invoked with low mass galaxies typically being late types and massive galaxies typically being early types (Dressler, 1980). These ideas have been extended to stellar population, Hɪ mass and SFR; where the blue, Hɪ rich (spiral) galaxies with high SFRs transition to red, Hɪ poor, passive (elliptical) galaxies as they advance to denser environments (e.g. Balogh et al., 2004; Baldry et al., 2006; von der Linden et al., 2010; Lemonias et al., 2013, and references within).

Many studies have proposed environmental mechanisms that operate at different strengths and timescales. The mass (internal) and environmental (external) mechanisms work together to transform galaxies and are used to describe the many complex pathways of galaxy evolution.

Tidal interactions

When galaxies come in close proximity of each other they gravitationally interact which can disturb the gas content and stellar population (Toomre & Toomre, 1972). These factors cause the gas to be shocked (inducing a starburst), heated (truncating star formation) or stripped (preventing star formation). The stellar population can be disturbed or stripped, or the galaxies can merge. Galaxies typically undergo a rapid starburst that is eventually followed by quenched star formation through internal feedback or restricted access to cold gas (e.g. Barnes & Hernquist, 1991; Barnes, 1992; Mihos & Hernquist, 1996; Bekki et al., 2001; Hopkins et al., 2006, 2010). Tidal interactions occur in all environments but are more likely to occur in high density environments and play a significant role in the quenching of star formation.

Galaxy Harassment

Galaxy harassment is a strong tidal interaction that occurs between a massive galaxy, (usually the brightest group/cluster galaxy), and a less massive one (Moore et al., 1996). A disc galaxy experiences multiple high speed encounters with the massive galaxy that leads to significant stripping of the gas and stellar population, only leaving the bulge intact after a few Gyrs (Moore et al., 1998; Smith et al., 2010). Galaxy harassment is believed to be a main cause for producing dwarf elliptical galaxies that are observed throughout galaxy clusters (e.g. Aguerri & González-García, 2009). Galaxy harassment operates over long timescales and the interactions are strong enough to transform a spiral galaxy into an elliptical.

Ram pressure stripping

When a galaxy is accreted onto a cluster, it experiences a pressure from the hot intracluster medium (ICM) that is powerful enough to strip gas out of the disc (Gunn & Gott, 1972; Nulsen, 1982). Even with a typical infall velocity, the entire ISM can be stripped within a crossing time ($\sim$100 Myr) of the cluster (Gunn & Gott, 1972;

19

Abadi et al., 1999; Quilis et al., 2000). The effects of ram pressure stripping have been observed in clusters where 'tailed' radio galaxies reveal their trajectory (Miley et al., 1972) and directly in the Virgo cluster where HI imaging show the gas being bent and pushed away from the direction of infall (Cayatte et al., 1990; Vollmer et al., 1999; Crowl et al., 2005; Abramson et al., 2011).

The rapid removal of the cold gas reservoir quenches star formation (e.g. Gunn & Gott, 1972; Bekki et al., 2010). However, compressed stripped gas can lead to star formation in 'jellyfish tails', but this does not prevent quenching (e.g. Owers et al., 2012). As the stellar disc remains undisturbed, ram pressure is thought to be a mechanism responsible for transforming spiral galaxies into lenticular galaxies (e.g. Quilis et al., 2000; Weinmann et al., 2006). Ram pressure stripping requires a hot ICM to strip gas and is therefore most efficient in dense environments such as massive galaxy clusters. Although, ram pressure is also believed to played a role in groups where the intra-group medium is responsible for stripping gas, albeit less efficiently (e.g. Rasmussen et al., 2006).

Strangulation

Strangulation (also known as starvation) is when hot halo gas is prevented from cooling and settling in the galaxy (Larson et al., 1980). It occurs when dynamical friction (e.g. falling into a cluster) removes the loosely bound hot halo gas. As strangulation does not intervene with the cold gas, the galaxy can sustain star formation with its cold gas reservoir. Once exhausted, star formation ceases. This process can take up to 4 Gyr to quench star formation (Treu et al., 2003; Peng et al., 2015). Strangulation is a (comparatively) gentle process that can transform a spiral galaxy into a lenticular galaxy (Weinmann et al., 2006).

1.3.3 Galaxy evolution in clusters

Galaxy clusters are located at the nodes of the cosmic web, making them the largest, densest and rarest virialised structures in the Universe. This presents an opportunity to test galaxy evolution by measuring the properties of hundreds of galaxies in a tightly-packed area. While the environmental mechanisms mentioned above operate in a range of galaxy densities, they are most efficient in clusters. An example of this are the brightest cluster galaxies (BCGs), the most massive galaxies in the Universe.

BCGs reside at the bottom of the cluster potential and have grown through numerous galaxy mergers made possible by the high galaxy density (e.g. von der Linden et al., 2007).

Galaxy clusters build mass through (major) merging with other equal mass clusters and by (minor) merging with lower mass groups or clusters. Major mergers rarely occur, but can violently reassemble the cluster and produce a large number of bluer, disturbed galaxies (e.g. Bekki, 1999; Markevitch et al., 1999; Chung et al., 2009). Minor mergers however, occur frequently and are a more gentle process responsible for most cluster mass growth (e.g. McGee et al., 2009). Both observations and simulations have shown that merging clusters are able to transform galaxies more efficiently than dynamically relaxed ones (e.g. Caldwell & Rose, 1997; Bekki, 1999; Poggianti et al., 2004; Hwang & Lee, 2009; Owers et al., 2011, 2012; Vijayaraghavan & Ricker, 2013).

Irrespective of cluster merger status, the galaxies contained in clusters are subject to frequent mass and environmental mechanisms that can strip gas, stars, quench star formation and transform morphology (e.g. Toomre & Toomre, 1972; Gunn & Gott, 1972; Dressler, 1980; Larson et al., 1980; Nulsen, 1982; Barnes & Hernquist, 1991). The resulting population of cluster galaxies are dominated by passive early-types and lenticulars that are HI poor and red in colour. (e.g. Balogh et al., 2004; Poggianti et al., 2006).

It was originally believed that the mechanisms operating in the dense cluster environment were largely responsible for efficiently transforming HI rich, star forming spirals to HI poor, quiescent early types. However, current thinking is that a galaxy can be stripped of its gas, have its SFR quenched and even undergo a morphological transformation prior to crossing the virial radius of a cluster (e.g. Lewis et al., 2002; Gómez et al., 2003; McGee et al., 2009; Wolf et al., 2009; Lu et al., 2012; Rasmussen et al., 2012b). This phenomenon is known as 'pre-processing' and is most likely to occur in two key locations; on the outskirts of clusters in galaxy groups (e.g. Rines et al., 2005; Mahajan et al., 2012; Verdugo et al., 2012; Konstantopoulos et al., 2013), and beyond the cluster outskirts in filament galaxies (e.g. Porter & Raychaudhury, 2007; Edwards et al., 2010; Biviano et al., 2011). Galaxy pre-processing is believed to have an integral role in galaxy evolution although its contribution to galaxy transformations is currently poorly constrained. In this thesis (Chapter 2), we present evidence for galaxy pre-processing in a detailed case study of the merging galaxy cluster Abell 1664 (Kleiner et al., 2014).

Groups of galaxies are usually funnelled along filaments of the cosmic web and gravitationally drawn towards galaxy clusters. It is unclear the extent to which filaments play a role in galaxy pre-processing. In the next section we explore the connection between the properties of a galaxy and its position in the wider cosmic web.

1.4   The cosmic web

The cosmic web is the name given to the underlying cosmological structure of dark and baryonic matter in the Universe. Initially seeded by the small density perturbations in the early Universe, the cosmic web at $z \sim 0$ consist of nodes, filaments and voids (Smoot et al., 1992; Bond et al., 1996). Galaxy clusters reside at the nodes and are intricately connected via a tenuous network of galaxy filaments that circumvent underdense voids. These features naturally arise in n-body and hydrodynamical simulations (e.g Springel et al., 2006; Popping et al., 2009; Angulo et al., 2012; Schaye et al., 2015; Nelson et al., 2015) and an example from the Illustris simulation is shown in Fig. 1.8. These features can also be observed when tracing the galaxy distributions in large galaxy surveys such as the 2 degree Field Galaxy Redshift Survey (2dFGRS), the Sloan Digital Sky Survey (SDSS), the 6 degree Field Galaxy Survey (6dFGS), the Galaxy And Mass Assembly survey (GAMA) and the 2MASS Redshift Survey (2MRS) (Colless et al., 2001; Abazajian et al., 2009; Jones et al., 2009; Driver et al., 2011; Huchra et al., 2012).

1.4.1   Filaments of galaxies

Simulations predict that up to 50% of galaxies (40% of the total baryonic mass) resides in cosmic filaments (e.g. Aragón-Calvo et al., 2010b; Tempel et al., 2014a). Does the cosmic web therefore have any influence on galaxies and their evolution? This idea has recently been in contention and testing it is non-trivial.

Despite the large baryonic mass in filaments, it is diffuse and below the detection threshold of current telescopes. It may be possible to directly detect the HI in filaments when the Square Kilometre Array (SKA) is fully operational but until then other methods must be used to define the cosmic web (Popping et al., 2009). This can be achieved by delineating the various components of the cosmic web in galaxy redshift data. As the cosmic web spans many orders of magnitude, the boundaries
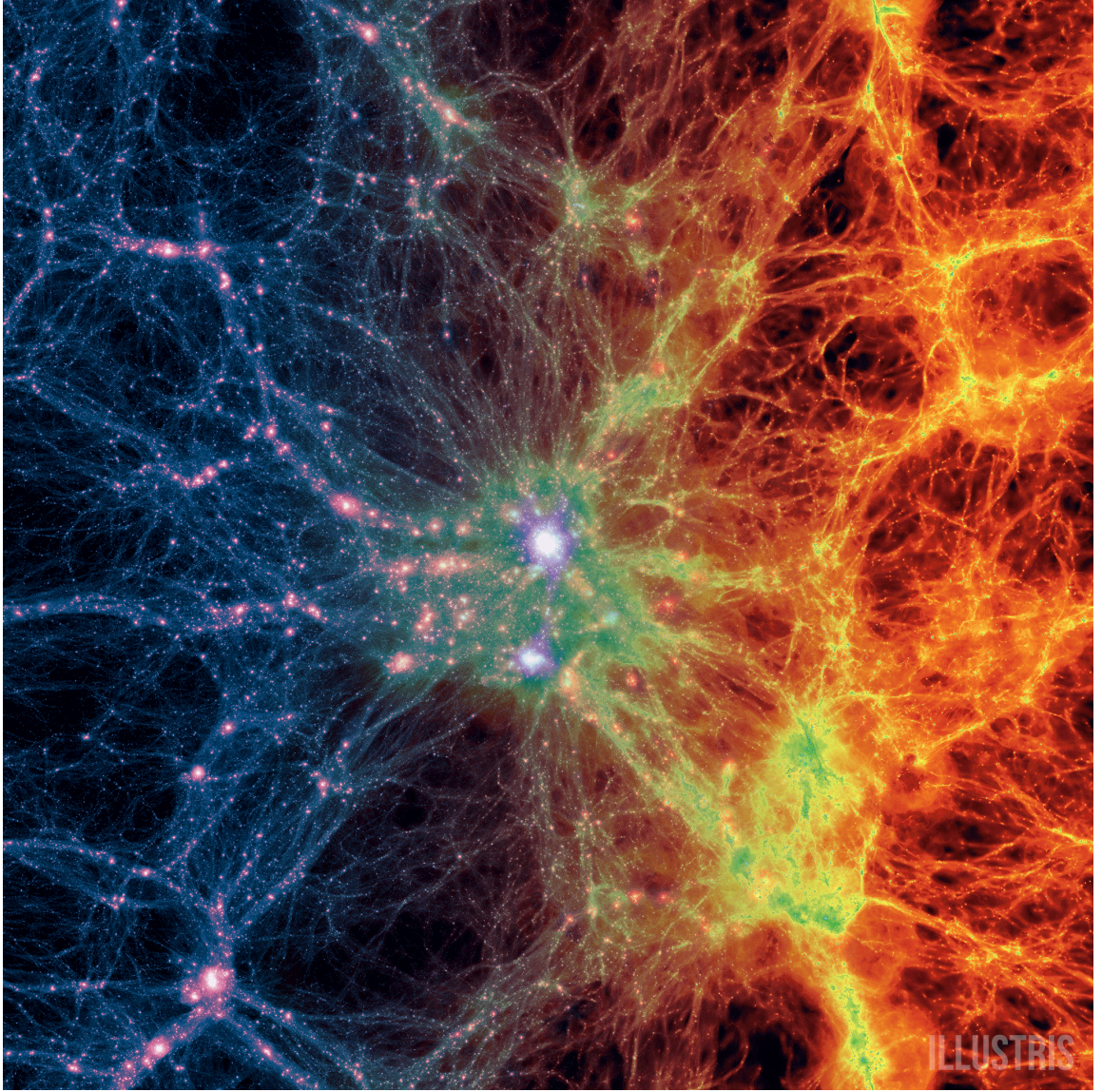
Fig. 1.8: Large scale projection from the Illustris simulation at z=0, centred on the most massive cluster (at 15 Mpc h^{-1}). The dark matter density starts on the left and transitions into the gas density on the right (Haider et al., 2016). As the baryonic matter (gas) traces the non-baryonic matter (dark matter), the features of the cosmic web are clearly seen throughout the whole image. Dense clusters are situated at the nodes, that are connected by tenuous filaments circumscribing underdense voids (http://www.illustris-project.org/media/).

between the features of the web are not clearly defined and delineating the features is complex. In addition to the astrophysical challenges, redshift survey data is often sparse, incomplete and provide inaccurate distances from redshift-space distortions (finger-of-god effect; Kaiser, 1987). Despite these difficulties, numerous attempts have been presented in the literature that are separated by a set of assumptions based on the physical, probabilistic and geometric treatment of the cosmic web (e.g. Pimbblet, 2005; Platen et al., 2007; Hahn et al., 2007; Aragón-Calvo et al., 2010a; Murphy et al., 2011; Sousbie, 2011; Cautun et al., 2013; Alpaslan et al., 2014; Dehghan & Johnston-Hollitt, 2014; Tempel et al., 2014b; Leclercq et al., 2015; Chen et al., 2015a). In Chapter 4.3 we discuss the pertinent details and differences between these algorithms.

Filaments are environments of intermediate density and act as pathways for individual and groups of galaxies to be deposited on galaxy clusters at the nodes. They are ideal sites for galaxy pre-processing to occur although it has not yet been determined if pre-processing is purely related to a galaxy's local (i.e. group) environment or if there are interactions between a galaxy and the baryonic content of filaments.

1.4.2   Galaxy evolution in filaments

Incorporating the galaxy's cosmological environment in models of galaxy evolution has been difficult to achieve with the necessary numerical precision. Only in the past few years have there been studies that connect the filamentary environment to the properties of galaxies.

Galaxies can accrete gas from filaments in a 'cold mode' (Kereš et al., 2005, 2009). This is achieved by gas from the IGM first being accreted onto the hot halo and then cooling via the emission of thermal radiation such that the gas can settle in the galaxy. In the early Universe, the IGM was much denser than the present epoch and gas accretion from filaments was the primary mechanism for building mass and replenishing the gas supply of a galaxy (e.g. Cantalupo et al., 2014). In the present epoch, the gas density of the IGM is significantly lower and not thought to be a dominant mechanism of mass build up. It is unclear if nearby galaxies have any significant interaction with the IGM and a key goal of this thesis is to disentangle the HI content (Chapter 4) and star formation activity (Chapter 5) from known stellar mass and environmental trends in filament galaxies.

Many ideas have been proposed in recent literature that include mechanisms that operate in filaments to explain galaxy evolution. However, it is not clear what the detailed physical mechanisms are or how efficiently they operate on the galaxies. The cosmic web detachment (CWD) model links the properties of galaxies in a natural cosmological framework (Aragon-Calvo et al., 2016). The CWD model can reproduce galaxy evolution features such as the colour dependence on mass and environment but it is challenging to test observationally. In CWD, galaxies with ongoing star formation accrete cold gas from filaments while they are part of the cosmic web. Once detached (via non-linear interactions), the gas supply is severed and star formation is quenched. Non-linear interactions cover a broad range of scenarios that can be applied to galaxies in all local densities. For example, galaxy clusters detach from the cosmic web when the ICM is heated, galaxy groups detach from the cosmic web via strong tidal interactions and void galaxies detach from the cosmic web when they exhaust their gas supply from the IGM in the immediate surroundings. A toy model showing three different scenarios of cosmic web detachment can be seen in Fig. 1.9.

In this framework, galaxy star formation is quenched when it detaches from the web, but the quenching timescale depends on the nature of detachment. In Chapter 4 and 5 we observationally test the CWD model by measuring the H I content and star formation activity of filament galaxies. Recent observational evidence of galaxy quenching in filaments has been presented in the literature. These studies are limited to measuring the properties of the stellar population (optical and UV) and we describe the key points below. No comprehensive framework (like the CWD model) is provided, however the quenching strength and relation to the filamentary environment are suggested.

Poudel et al. (2016) find more luminous central group galaxies in filaments. They are redder with lower SSFRs than a comparison sample not residing in filaments. An efficient mechanism other than galaxy density alone is suggested to explain these trends. Filament galaxies are observed to have lower SSFRs than mass matched samples outside filaments (Alpaslan et al., 2016; Martínez et al., 2016). A suggested scenario was that stellar mass was the primary discriminator for SFR and a gentle, weaker second order mechanism operates in filaments to quench star formation. Filaments are also described by Chen et al. (2015b) as an extension of the morphology-density relation (Dressler, 1980). The cosmic web traces the intermediate environment that is dominated by galaxy groups and red (high-mass) galaxies tend to reside closer to filaments than blue (low-mass) galaxies (Chen et al., 2015b). The observational evidence points
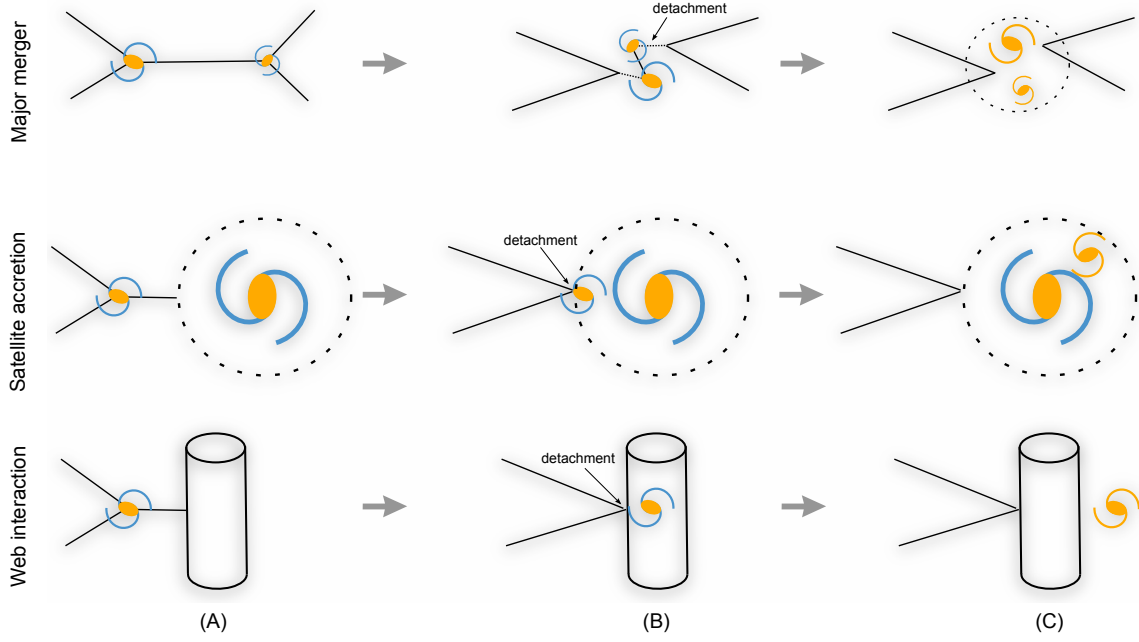
Fig. 1.9: Three toy models from Aragon-Calvo et al. (2016) showing CWD events where non-linear interactions detach a galaxy from the cosmic web. From top to bottom: major galaxy merger, accretion of a satellite galaxy and filament crossing. The broad steps of CWD events occur as follows: A) The galaxy is attached to the cosmic web and is accreting cold gas from the IGM. B) The galaxy then suffers a violent detachment event from either a merger, accretion into a larger halo or pushed through a filament. C) The detached galaxy no longer has access to cold gas and subsequently undergoes quenching. CWD events are not limited to these three examples but the end result is the same where a galaxy's star formation is quenched due to the ceased accretion of IGM cold gas.

to the common finding of a quenching mechanism operating in filaments. It is unclear what drives the mechanism(s) and there is disagreement between the strength of the proposed mechanism(s).

To date, there have not been any direct findings between the gas content of filament galaxies and their interaction with the IGM permeating filaments in the nearby Universe. Determining if galaxies in filaments are able to access the diffuse IGM of filaments will help constrain the proposed quenching mechanisms suggested in the recent studies.

1.5   Thesis goals

This thesis searches for signatures of galaxy pre-processing and interactions between the H I content and star formation activity of a galaxy with filaments of the cosmic web. We achieve this through two separate but complementary approaches to study the mechanisms driving galaxy evolution in the cosmic web.

The first approach focuses in detail on a galaxy cluster and asks:

- What are the properties of cluster galaxies during a minor merger?

- Can a minor merger transform cluster galaxies?

The second approach utilises a geometric technique to identify filaments in a nearby galaxy survey and asks:

- Can we detect evidence for H I interactions between a galaxy and the gaseous medium of filaments?

- What role do filaments play with the galaxy H I reservoir?

- What fraction of filament galaxies are forming stars and how efficiently does it convert H I to stars?

This thesis is organised as follows: Chapter 2 presents the case study of a galaxy cluster undergoing a minor merger. We do this by quantifying substructure in the cluster, and trends in galaxy colour are used to determine the effect of the merger on cluster galaxies. In Chapter 3 we create two mocks using abundance matching

and semi-analytic models and compare their spatial distribution to observations in preparation of creating a group and filament catalogue. Chapter 4 delineates those filaments in a nearby galaxy survey and compares the H I content of filament galaxies to a control sample with the same mass and galaxy density. We extend this work in Chapter 5 by measuring the SFR of the same galaxies and search for evidence of quenching in the star formation activity and efficiency. In Chapter 6, we summarise the work done in this thesis and describe future work.

Monash University
Declaration for Thesis Chapter 2

Declaration by candidate:

I declare that my contribution to the work in Chapter 2 that is published in the Monthly Notices of the Royal Astronomical Society as Kleiner et al. (2014), involved the following:

The writing of the publication, the sample selection, analysis, and all other work contained therein (that is not referenced otherwise), excepting collection of the survey data and development of the data products that were used, such as: photometry, redshifts, spectroscopy.
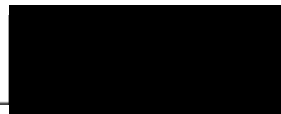
Extent of contribution by candidate: 85%

Co-author names: Kevin A. Pimbblet, Matt S. Owers, D. Heath Jones, Andrew P. Stephenson

Nature of co-author's contribution: The collection of the survey data, image reduction assistance, production of the X-ray temperature map and original substructure algorithm along with comments and feedback during writing of the paper. I have renumbered sections, equations and figures of the published paper in order to generate a consistent presentation within the thesis.

The undersigned hereby certify that the above declaration correctly reflects the nature and extent of the student's and co-authors' contributions to this work.
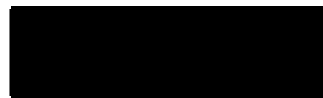
Candidate's signature:

Date: May 23, 2017

Main Supervisor's signature:

Date: May 23, 2017

CHAPTER 2

Photometric studies of Abell 1664: The subtle effect a minor merger has on cluster galaxies

Dane Kleiner, Kevin A. Pimbblet, Matt S. Owers, D. Heath Jones and Andrew P. Stephenson

Abstract

A combination of *BRI* photometry and archival Chandra X-ray data have been used to analyse the effects a minor merger has on the galaxy population of A1664. We utilise adaptive smoothing techniques in the 2D spatial distribution of cluster galaxies to reveal substructure $\sim$ 800 kpc South of the cluster core. We identify this substructure as most likely the remnant core of a merging group which has passed pericentre and responsible for triggering a cold front in the cluster core. We define two samples to represent two different environments within A1664 in accordance with the location of the substructure. We apply a morphological analysis using CAS, M_{20} and Gini to these samples to deduce if there has been any significant effect on the cluster galaxies due to this interaction. We find there are more asymmetric galaxies found in the inner sample (at the 3.7σ level) which is likely due to galaxy-galaxy interactions as the merging group passed through core passage. No other differences were found between the inner and outer cluster in our morphological analysis, which we attribute to the limited resolution of our imagery. The colour profiles of the galaxies are found to be consistent with the morphology-density relation suggesting there is no unique environmental effect in A1664 that has enhanced galaxy transformations. This study favours the star formation of cluster galaxies being quenched well before it is able to interact with the merging group and demonstrates that a minor cluster merger has

little effect on the observable parameters of cluster galaxies such as morphology and colour.

2.1   Introduction

In a Universe where structure forms through hierarchical growth, galaxy clusters are the largest structures which are virialised at the current epoch. Individual clusters can offer the opportunity to study the properties of hundreds of galaxies in the densest environment in the Universe. It has been well documented that the cores of low redshift clusters are heavily populated by red early type galaxies and display significantly different properties to galaxies found in less dense environments (Dressler, 1980; Balogh et al., 2004; Poggianti et al., 2006). The rich cluster environment hosts a number of interactions (both galaxy-galaxy and cluster-galaxy) that offer the potential to explain the difference in observed galaxy properties between galaxies found in over- and under-dense environments. For example galaxies that are close enough to gravitationally interact can destroy spiral discs and induce an episode of star formation (Toomre & Toomre, 1972). Strong tidal interactions between galaxies can strip gas from the interacting galaxies in long tidal tails (Barnes & Hernquist, 1991) and dwarf galaxies that interact with much more massive galaxies can be gravitationally shocked, removing up to 50% of its gas content (Moore et al., 1996). As galaxies travel through the ICM, the impact with the hot intra-cluster gas can strip the gas contained in the disc (Gunn & Gott, 1972; Nulsen, 1982) or remove the reserve gas supply in the halo preventing the reservoir of halo gas to condense in the disc and form new stars (Larson et al., 1980).

One important result in this area is that cluster galaxies at large cluster-centric radii are found to have a observable properties such as colour, morphology and star formation rate (SFR) that have already been truncated (Lewis et al., 2002; Gómez et al., 2003; McGee et al., 2009; Wolf et al., 2009; Lu et al., 2012; Rasmussen et al., 2012a). This conclusion shifted the focus away from transformations in the dense cluster environments being the only reason that explains the difference of galaxy properties in different environments. Less dense environments such as galaxy groups in the outskirts of clusters (Rines et al., 2005; Mahajan et al., 2012; Verdugo et al., 2012) and filaments of galaxies (Porter & Raychaudhury, 2007; Edwards et al., 2010; Biviano et al., 2011) are now considered favourable sites for first-time tidal interactions and are thought to play a vital role in explaining the difference in galaxy population.

Through these interactions, the star formation fuel of a galaxy can be used up in a starburst (i.e. Porter et al., 2008) or through quenching (i.e. Lu et al., 2012) at these sites. Galaxies that have experienced these transformation have been "preprocessed" prior to accreting to the cluster potential.

There exists alternative evidence to suggest that preprocessing is not the main cause for the difference in galaxy populations. von der Linden et al. (2010) and Haines et al. (2013) show that a galaxy's SFR can be quenched slowly within the cluster and the morphology-density relation is weak or non-existent beyond the clusters virial radius. Berrier et al. (2009) show that preprocessing is not efficient enough to explain the full observed difference between cluster and non-cluster galaxies where physical cluster mechanisms must play a significant role in explaining the high fraction of red early types in dense environments. It is not well known how efficient preprocessing is and what fractions of galaxies are transformed through cluster mechanisms.

An additional ingredient in this discussion about cluster galaxy evolution is the merger of galaxy clusters themselves. It is a rare occurrence for two clusters of equal mass to merge. However, when a major merger occurs the result is a violent reassembly of the cluster (Markevitch et al., 1999). Minor mergers (i.e. a group merging with a cluster) are more 'gentle' and common. A significant fraction of a clusters final galaxy population is therefore accreted through groups merging with the cluster (McGee et al., 2009). Compared to more dynamically relaxed clusters, a merging cluster provides a more hostile environment for the resident galaxies. Previous studies (e.g. Caldwell & Rose, 1997; Poggianti et al., 2004; Hwang & Lee, 2009; Owers et al., 2011, 2012) have shown that merging clusters have the ability to transform galaxies much more efficiently than a cluster in relative isolation and calm environs. Numerical simulations have shown that group-cluster mergers can cause a secondary starburst in cluster galaxies (Bekki, 1999) and while the merging group is traveling through pericentre, galaxy-galaxy collisions and ram pressure stripping are enhanced (Vijayaraghavan & Ricker, 2013). As the nature of cluster mergers is complex, the full effect that this reconfiguration has on individual galaxies is yet to be fully understood.

In this paper we analyse Abell 1664 (hereafter A1664), a nearby ($z = 0.128$; Allen et al., 1995) post-merger galaxy cluster that offers a rare opportunity to study galaxy evolution afforded by its merger status. It has an Abell richness of 2 (Abell et al., 1989) with a velocity dispersion of $\sigma_v = 1069^{+75}_{-62}$ km s^{-1} (Pimbblet et al., 2006). A1664 is very bright in the $0.1 - 2.4$ keV band with an X-ray luminosity of 4.1×10^{44} erg

s^{-1} (Allen et al., 1992) where the X-ray morphology is elongated in the South (Figure 2.1). As the X-ray emission traces the hot intra-cluster gas, the asymmetry in the morphology reveals that A1664 is not a relaxed cluster and the extension in the gas is likely to have once belonged to the merging group. When a cluster undergoes a minor merger, the gravitational disturbance can trigger gas "sloshing" in the cluster core. If the cluster hosts a dense cool core, this sloshing can generate contact discontinuities at the interface of the displaced cool core gas and the hotter, less dense gas at larger radius (Ascasibar & Markevitch, 2006). These contact discontinuities, otherwise known as cold fronts can be used to identify recent cluster mergers (Owers et al., 2009). Kirkpatrick et al. (2009) show there to be a sloshing cold front in the core of A1664. They further show the brightest cluster galaxy (BCG) with an unusually high SFR can be explained by a flow of cold gas being deposited on the BCG.

In this case study, our goal is to determine how different environments in a post merger cluster have affected the properties of the galaxies in A1664. Section 2.2 describes the data analysis and sample selection of the BRI photometric data and *Chandra* image. In Section 2.3, we present the analysis of the galaxy properties in different environments. In Section 2.4, we present the discussion and interpretation of our results on the effect a merging group has on cluster galaxies. Lastly, in Section 2.5 we summarise our findings.

Throughout this paper, we use a ΛCDM cosmology where $H_0 = 70$ km s^{-1} Mpc^{-1}, $\Omega_m = 0.3$ and $\Omega_\Lambda = 0.7$. At this redshift of the cluster ($z = 0.128$), the assumed cosmology gives $1'' = 2.287$ kpc.

2.2 Observations and Data Reduction

2.2.1 Optical data

Our observations of A1664 were made in the I-band at the Australian National University 40$''$ telescope at Siding Spring Observatory. At the redshift of this cluster ($z = 0.128$), this bandpass is sensitive to the old stellar populations and dusty galaxies, making it ideal for observing cluster galaxies and their properties. The observations were taken using the wide field imager (WFI). WFI is a mosaic imaging camera that consists of eight 2k $\times$ 4k pixel charged coupled device (CCD) arranged to give a final image that is 8k $\times$ 8k pixel. The pixel size of WFI is approximately $0.376'' \times 0.376''$
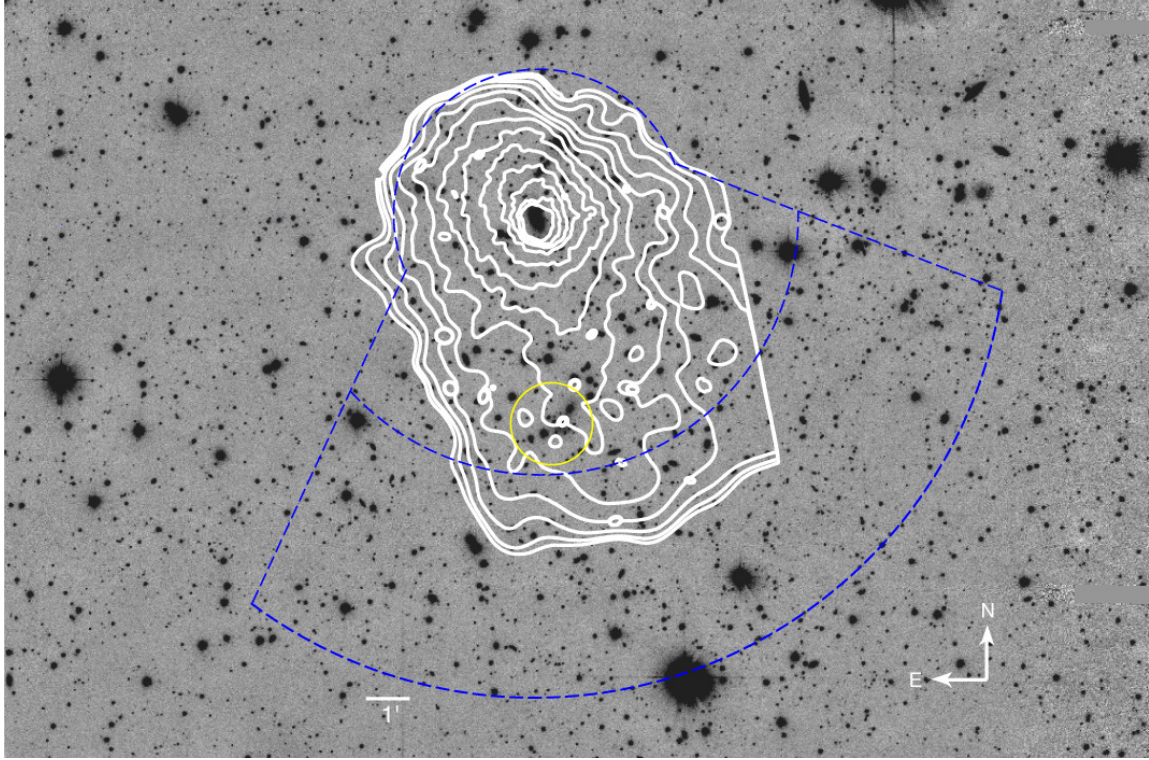
Fig. 2.1: Coadded *I*-band image of A1664 showing gaussian smoothed X-ray surface brightness contours from an archival Chandra X-ray image in the 0.5 - 7 keV range. The X-ray emission traces the hot intra-cluster gas and shows an elongated morphology which extends to the South-West. The blue dashed regions outline the limits used to define the inner and outer samples in the photometric analysis. The yellow circle encloses a group of galaxies which we identify as the most likely merging group responsible for the elongated X-ray emission.

near the optical axis of the 40″ which gives an impressive field of view of 52 square arcmin (1.2 degree on the diagonal)[1]. The eight individual CCDs are non-linear by ∼ 5 per cent over their dynamic range.

Reduction is performed in the standard manner using the MSCRED package in IRAF. Briefly, the steps involved include a bias subtraction, a linearity correction followed by flat-fielding of the data using twilight flats. Since WFI is operated at a relatively warm temperature ($\approx$ 183 Kelvin), a dark subtraction is also performed. After processing, our science images are flat to better than 1 per cent of the sky background across the entire mosaic.

A world coordinate system (WCS) was created from scratch by matching an average of 5 stellar positions to US Naval Observatory (USNO; Monet et al., 2003) stellar catalogue per WFI CCD. The WCS were refined by matching up bright, non-saturated stars using the MSCTPEAK task and eliminating stars with high proper motions. Our residual fits for the WCS are typically much better than 0.6 arcsec; rms $\approx$ 0.2 arcsec. By employing this WCS, our multi-extension fits file imaging is then converted into single fits file imaging using MSCIMAGE which corrects for the radial distortion present in the raw data. After the elimination of bad pixels using the FIXPIX routine, we register our observations with MSCZERO and combine them utilising MSCSTACK

The final science images are aligned in each passband and trimmed to the same size. Cataloguing of the cluster is performed with SExtractor (Bertin & Arnouts, 1996) to permit the detection and photometry of objects in the I-band. The final photometry is calibrated from at least 15 sets of standard star observations selected from Landolt (1992) scattered throughout each night. Despite some unstable seeing conditions for our observing run each night was photometric with a seeing of $\lesssim$ 2 arcsec where the seeing was measured as the median from the point spread function of the stars as measured with SExtractor (Bertin & Arnouts, 1996). Zeropoint and colour term equations used to calibrate our observations yield a final average error of ∼ 0.05 mags. We consider this calibration error to be the dominant source of photometric error.

To create a coadded I-band image, a bad pixel mask was created and assigned to each individual image such that no additional noise was added in the stacking process. We were selective with images used in the stacking processes such that only the images with a seeing of less than 2.5 arcseconds were combined using the *Swarp* package

---

[1]Given the wide field of view afforded by WFI, the pixel scale varies by up to 9 per cent from the optical axis to the edge of the CCD array.

(Bertin et al., 2002). The photometry from a Hubble space telescope (HST) I-band image that contained overlapping objects in our field was used to calibrate the RA, DEC and magnitudes. Between $16 < I_{HST} < 20$ the calibrated RMS is 0.15 mags. The image and corresponding catalogue that we present has detected all galaxies not subject to stellar confusion down to a magnitude of $I = 20.0$.

Star-galaxy separation is achieved through the size of the object and the use of the CLASS_STAR parameter within SEXTRACTOR which, following Pimbblet et al. (2001), objects greater than 2 arcsec with a CLASS_STAR < 0.1 are classified as galaxies. Further, we use the MAG_BEST magnitude as our estimate of the total magnitude of a given object.

To include colour information B (sensitive to the young stellar population - late type galaxies) and R-band (sensitive to the older stellar population - early type galaxies) photometry from the LARCS catalogue (Pimbblet et al., 2006) was matched to objects in the I-band throughout the overlapping field. The colour information was computed by using equi-sized apertures in each filter with a radius equal to 2.5 arcsec, which is worse than the seeing in any of the science images.

The BCG of A1664 was identified as the brightest spectroscopically confirmed cluster member (Pimbblet et al., 2006). Kirkpatrick et al. (2009) identified the BCG in A1664 by correlating their optical image with the observed cold gas flow and the co-ordinates of the BCG (J2000 13:03:42 -24:14:42) match those in our calibrated I-band image (Figure 2.1).

Cluster galaxy identification

With a sufficient number of spectroscopically-confirmed cluster galaxies then cluster member identification can be formulated using their redshift, magnitude and colour. However, if sufficient spectroscopic data is lacking, foreground and background interloping galaxies must be eliminated as best as possible through another method in order to minimise contamination in the cluster analysis. We use two different methods using the available spectroscopy and photometry to identify cluster galaxies for two different types of analysis. For the analysis of 2d spatial and luminosity density of the cluster (Section 2.3.1), we include galaxies from the scatter around red sequence and the available spectroscopy (method (i) below). For the analysis that quantifies the properties of individual galaxies (Sections 2.3.2), we use a Monte Carlo style statistical correction in colour-magnitude space (method (ii) below).

i) There exists a well-established correlation between the colour of early-type galaxies and their corresponding luminosity (Sandage & Visvanathan, 1978; Larson et al., 1980). Due to the high number of viralised early-type and S0 galaxies contained in clusters, the majority cluster galaxies will form a tight red sequence relation in colour - magnitude space (known as the colour magnitude relation - CMR). This well defined relation can be used to define which are likely cluster galaxies and which are obvious interlopers. At the same redshift as the cluster, no galaxy can be significantly redder than the cluster's CMR (dust reddening will redden a galaxy by a minimal amount) which means that much redder galaxies must be background objects. Similarly, at the redshift of the cluster all galaxies brighter than the BCG can be excluded as no galaxy which is a part of the cluster can be brighter than the BCG. Figure 2.2 shows the CMR of A1664 and using these relations, we are able to constrain which galaxies are a part of the cluster.

We define galaxies within 2 standard deviations of the scatter of the red sequence down to a luminosity of M* + 1.5 to be cluster galaxies. We also include spectroscopically confirmed cluster members which are too blue to be included in our red envelope. Some background blue galaxies will be redshifted into our sample but their contribution will be minimal as there are many more cluster galaxies that lie within the limits of the red sequence (Lu et al., 2009).

ii) Although we have 72 spectroscopically-confirmed galaxies (Pimbblet et al., 2006), there are many galaxies that belong to A1664 that do not have spectroscopic measurements. We use a combination of the spectroscopically-confirmed galaxies and the photometric characteristics to apply a statistical field correction similar to Pimbblet et al. (2002). Equation 2.1 assigns the probability $P(C)$ of being a cluster member to each galaxy. $N(C + F)$ is the number of galaxies in colour-magnitude space known to contain both cluster and field galaxies. $N(F)$ is the number of galaxies in colour-magnitude space known to contain purely field galaxies. The field region must be a true representation of a large sample of field galaxies. This is achieved by the selected region containing no cluster galaxies and no other known clusters or dense environments[2]. The area ratio A scales the selected Field region to the same size as the Cluster + Field region.

$$P(C)_{col,mag} = \frac{N(C + F)_{col,mag} - N(F)_{col,mag} \times A}{N(C + F)_{col,mag}} \qquad (2.1)$$

---

[2]Our field region was selected in an analogous method to Pimbblet et al. (2002) to be 0.131 deg^2 at a large clustercentric radius.
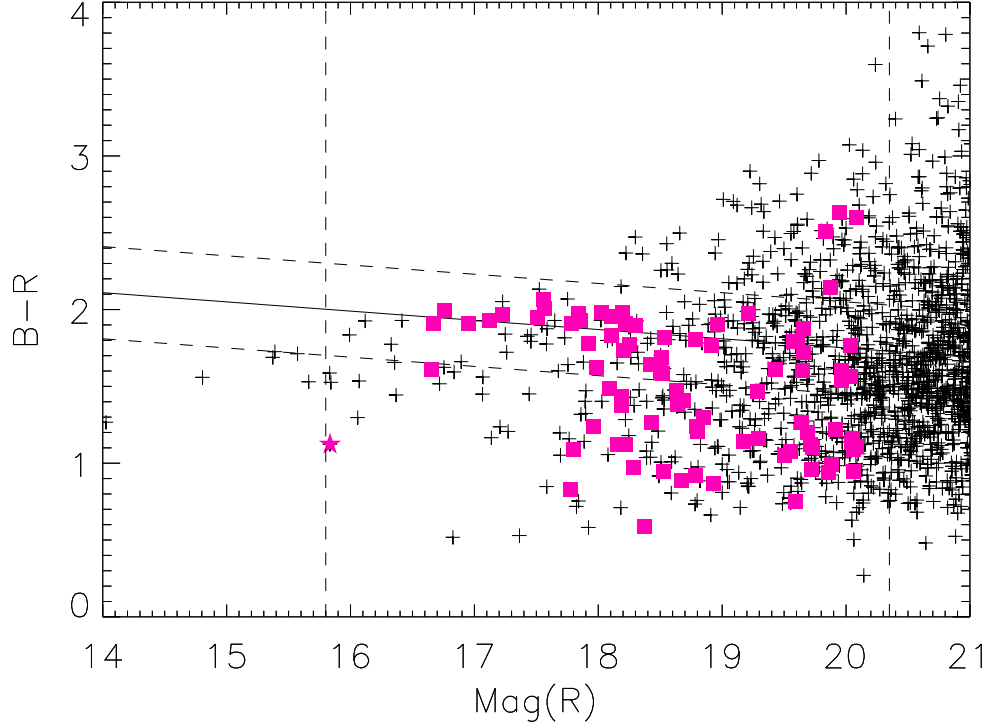
Fig. 2.2: The colour magnitude relation for A1664. The solid line represents the cluster red sequence which has been defined through spectroscopically confirmed-galaxies (over-plotted magenta squares). The dashed parallel lines to the CMR are the 2σ limits used to define an envelope for the galaxies to be included in the adaptive smoothing analysis. The BCG is shown with an over-plotted magenta star and galaxies fainter than the BCG down to a magnitude of $M^* + 1.5$ as well as spectroscopically-confirmed blue galaxies have been selected as the input for the adaptive smoothing.

38

The probability of each galaxy is compared to a random number generated between 0 and 1. If $P(C) > $ P(random) then the galaxy is retained as a cluster member for the analysis. This process is repeated 100 times in a Monte Carlo fashion to generate the random numbers. As we have limited velocity information available, we denoted the velocity dispersion of the cluster as 1σ where any galaxy with a recessional velocity within 3σ is assigned a probability of 1, automatically including them as cluster galaxies for every trial. Conversely, galaxies with a recessional velocity outside 3σ are assigned a probability of 0 for each trial, ensuring they are never classified as a cluster galaxies. See the appendix in Pimbblet et al. (2002) for the full method of the statistical field correction without velocity information.

2.2.2 Chandra data

A1664 has been observed twice with *Chandra*; a 10 ks exposure in June 2001 (ObsID 1648) and a 37 ks exposure in December 2006 (ObsID 7901). The *Chandra* data were reprocessed using the CHANDRA_REPRO script within the CIAO software package (version 4.4; Fruscione et al., 2006). The script applies the latest calibrations to the data (CALDB 4.5.1), creates an observation-specific bad pixel file by identifying hot pixels and events associated with cosmic rays (utilising VFAINT observation mode) and filters the event list to include only events with *ASCA* grades 0, 2, 3, 4, and 6. The DEFLARE script is then used to identify periods contaminated by background flares and no significant contamination was found. For the imaging analyses, exposure maps which account for the effects of vignetting, quantum efficiency (QE), QE non-uniformity, bad pixels, dithering, and effective area were produced using standard CIAO procedures[3]. The energy dependence of the effective area is accounted for by computing a weighted instrument map with the SHERPA make_instmap_weights script using an absorbed MEKAL spectral model with $N_{\mathrm{HI}} = 8.95\times10^{20}\mathrm{cm}^{-2}$ (Dickey & Lockman, 1990), the average cluster values of $kT = 3.65\,\mathrm{keV}$ and abundance 0.46 times solar (Kirkpatrick et al., 2009) and $z = 0.128$. Background subtraction for both imaging and spectroscopic analyses was performed using the blank sky backgrounds[4]which were processed in the same manner as the observations. The blank sky backgrounds were reprojected to match the tangent point of the observations, and were normalised to match the $10 - 12\,\mathrm{keV}$ counts in the observations.

---

[3]cxc.harvard.edu/ciao/threads/expmap_acis_multi/
[4]cxc.harvard.edu/contrib/maxim/acisbg/
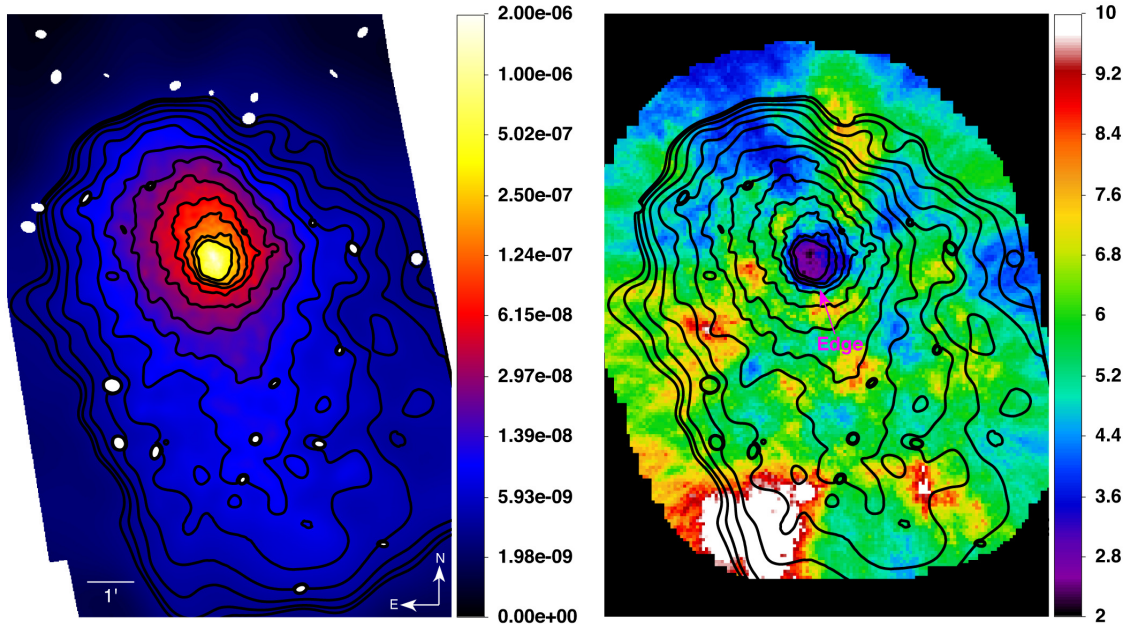
Fig. 2.3: Left is the background subtracted and exposure corrected 0.5-7keV Chandra image. The colour-bar shows the number of photons s^{-1} cm^{-2} and the extension of the ICM emission in the South is clearly visible. On the right is the temperature map where the edge in the cluster core reveal the cold front. The colour-bar is in units of keV and the presence of cold front confirm that A1664 has undergone a recent merger which is past pericentric passage.

Figure 2.3 shows the combined, background subtracted and exposure corrected *Chandra* image of A1664. The image was adaptively smoothed using the adaptive_density_2d software within the TARA[5] package. The smoothing length was set such that a signal to noise of 10 was achieved for each pixel. Point sources identified with the CIAO tool wavdetect were masked prior to smoothing.

A temperature map (Figure 2.3) was created in a similar fashion to Owers et al. (2013) where a spectra was extracted for each $3.94'' \times 3.94''$ pixel using a circular region with radius set such that the total number of background-subtracted counts in the $0.5 - 7$ keV band is $\sim$1000. Spectra are not extracted where the radius required is $\gtrsim 120''$. Responses are extracted on a more coarsely binned ($\sim$16$''$ $\times$ 16$''$ pixel) grid. Spectra and responses are extracted for both of the observations. The spectra are then fitted within XPSEC (Version 12.7.1; Arnaud, 1996) using an absorbed mekal model (Mewe et al., 1985, 1986; Kaastra, 1992; Liedahl et al., 1995) with the hydrogen column density fixed at the galactic value ($n_{HI} = 8.95 \times 10^{20}$

---

[5]http://www2.astro.psu.edu/xray/docs/TARA/

40

cm^{-2}), metallicity fixed at 0.45 relative to the solar value (value from Kirkpatrick et al., 2009) and temperature allowed to vary to its best fitting value. Because of the top-hat method of extraction for each pixel, the temperatures are highly correlated where the X-ray brightness is low.

2.3   Photometric Analysis

2.3.1   Substructure and sample definition

To search for substructure, we make use of an adaptive smoothing technique on a conservative selection of cluster galaxies identified through the first method in Section 2.2.1 The adaptive smoothing follows the same two-step procedure outlined in (Owers et al., 2013). Briefly, the spatial distribution of galaxies is first smoothed with a fixed-width Gaussian kernel with an optimal width derived from the data. The resulting smoothed distribution is used to define an adaptive smoothing length at each point which depends on the local galaxy surface density. The resulting smoothed surface density map is sensitive to structure between 200 - 1800 kpc.

Figure 2.4 shows the result of the adaptively-smoothed 2d spatial distribution of cluster galaxies centred on the BCG. We identify a local peak in the galaxy number density distribution 800 kpc from the BCG and to the South. The number density in this region is comparable to the cluster core and indicates that there may be substructure present here. Within this, there is an optically bright galaxy (yellow circle in Figure 2.1) which is more luminous than all the other galaxies in the substructure. This galaxy has an absolute R-band magnitude of -21.39 which is 1.39 mags fainter than the BCG and we consider it to be the brightest group galaxy of this substructure.

A caveat of using the galaxy number density for the adaptive smoothing is that it treats all galaxies as being equal, ignoring the mass of each galaxy. To account for the mass of each galaxy, we assume that galaxy light traces the mass distribution for cluster galaxies. Figure 2.5 shows the adaptively-smoothed luminosity density for the cluster galaxies in A1664. The same galaxies used in the smoothed galaxy number density (Figure 2.4) have been weighted according to its luminosity relative to the BCG and smoothed with the same smoothing lengths as the galaxy number density. This method ensures the mass of each galaxy is taken into account and
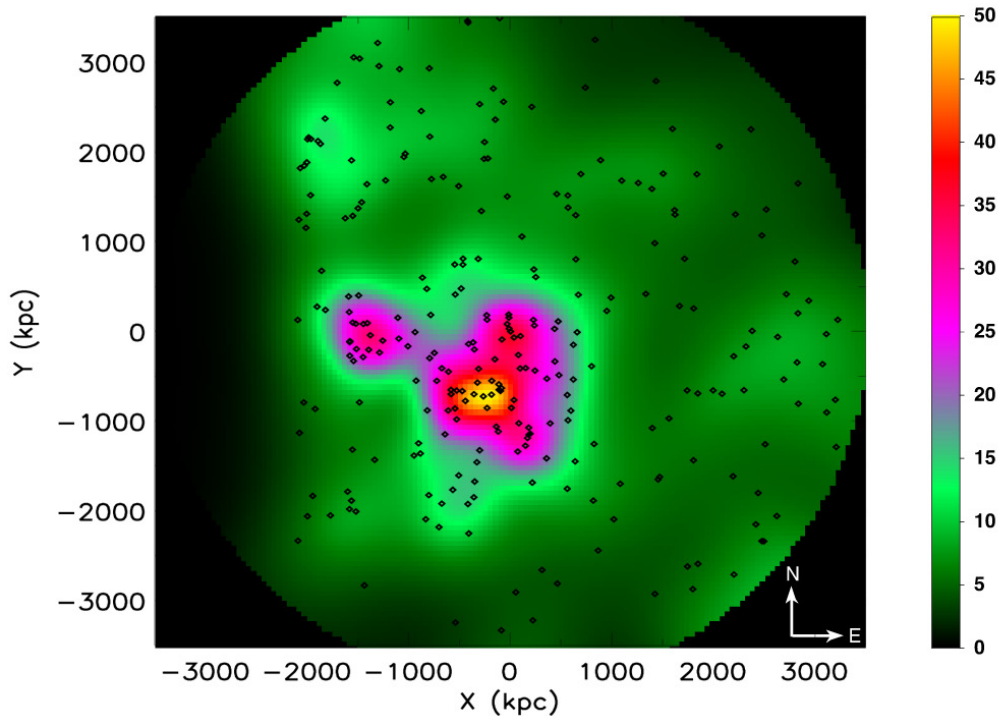
Fig. 2.4: The 2d spatial distribution of adaptively-smoothed cluster galaxies. Galaxies with a B-R colour within 2σ of the red sequence and spectroscopically confirmed blue galaxies down to $M^* + 1.5$ were included for the smoothing. The origin is set to the location of the BCG where the black diamond show the individual galaxies and the colour-bar highlights the number of galaxies per Mpc^2. The dense feature seen South-West of the cluster core which we identify as best candidate for the merging group.

is a more accurate method for searching for substructure. The largest over density seen in Figure 2.5 coincides with the largest over density in Figure 2.4 which is strong evidence this feature is the group merging with the cluster. Investigating the properties (i.e. colour and morphology) of the galaxies contained in this group would be an interesting comparison to the cluster galaxies. However, we lack the numbers of spectroscopically confirmed galaxies to separate galaxies belonging to the group from the cluster. Attempting this analysis with the data used in this study would result in group membership being underestimated or contain significant interlopers. Therefore, we leave this task for future work when more spectroscopic data is available.
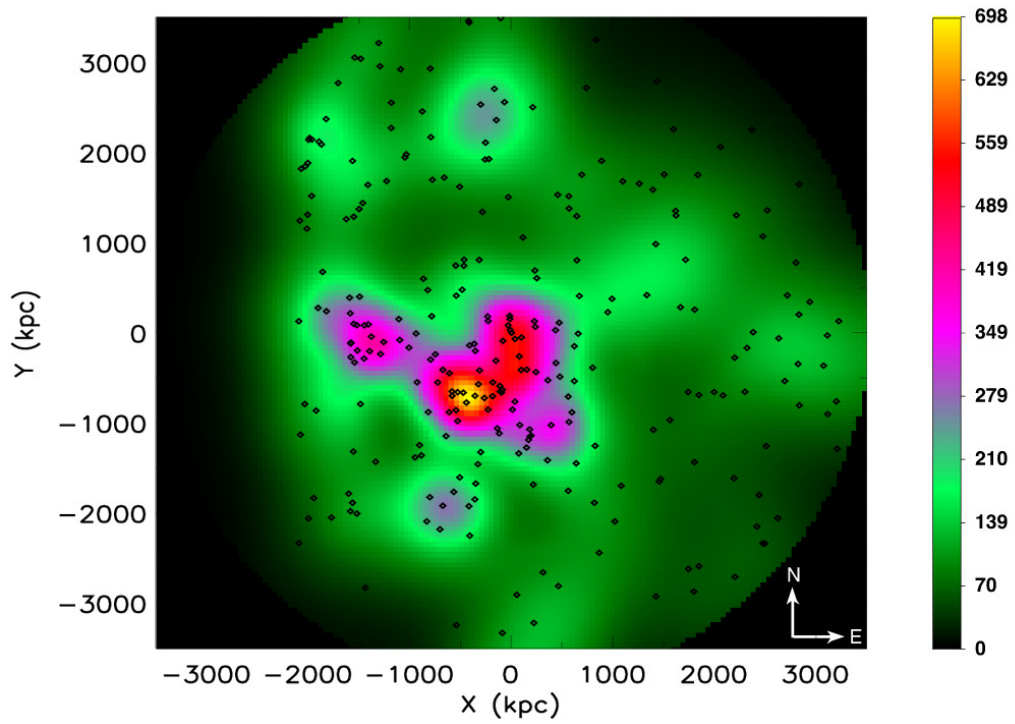
Fig. 2.5: Adaptively-smoothed cluster galaxies where each galaxy has been weighted according to its magnitude relative to the BCG. The same smoothing lengths from Figure 2.4 were used to ensure no artefacts were introduced from the weighting. The symbols are the same as Figure 2.4 where the colour's now show the relative weighted number of galaxies per Mpc^2.

We relate the position of the detected substructure to the X-ray surface brightness and temperature map (Figure 2.3) to define our galaxy samples. The extended X-ray emission to the South seen in the X-ray surface brightness is likely to be additional emission from the group responsible for the minor merger. If the detected substructure is the group merging with the main cluster then it will be responsible for triggering the cold front shown in the temperature map. With these features in mind, we define two samples to represent different environments within A1664.

The two samples are shown as blue dashed lines in Figure 2.1. The inner sample is the dense regions of A1664 as it includes the cluster core and the detected substructure. The outer sample is the under dense region of A1664 as it is dominated by the cluster outskirts which is sufficiently far away from the cluster core and detected substructure. While maintaining the condition that the inner sample is dense compared to the outer sample, we have run the analysis with different limits for the samples and find no significant change in our results.

2.3.2 Galaxy properties

Here, we investigate how the galaxies have responded to the merger in the two different environments. Cluster membership has been assigned using method ii) in Section 2.2.1 where all uncertainties are 1σ errors assigned from the scatter in the Monte Carlo simulation unless stated otherwise.

Morphological properties

One of the most frequently used ways to probe the recent history of galaxies from their photometry alone is to quantitatively determine their morphology. There are a number of options for doing this, but by far the most widely used and tested is the Concentration-Asymmetry-clumpinesS (CAS; Conselice, 2003) approach and its extensions. We search for subtle differences in the I-band CAS (Conselice, 2003), M_{20} and Gini (Lotz et al., 2004) morphological parameters by measuring the median and skewness of the distribution for each morphological parameter over both samples (Table 2.2). Abraham et al. (1996) used a comparable approach (albeit with a slightly different definition of asymmetry and concentration to Conselice, 2003) and note that highly skewed asymmetry values are present because their sample is dominated by irregular, peculiar and merging galaxy systems. We also measure the median and

skewness of the same morphological parameters of the field galaxies used in section 2.2.1 (Table 2.2). This provides us with a control sample to contrast our results to where the uncertainty in the field was measured by jackknifing 6 equal areas of the field sample.

We find that the median of the distribution for all the morphological parameters are within uncertainties between the inner, outer and field samples. The skewness of the distribution for all morphological parameters except asymmetry are also within uncertainties between the samples. This result implies that the population of galaxies is the same in all the galaxy samples down to our spatial resolution limit. The skewness of the asymmetry distribution is significantly higher in the inner sample which indicates there is a greater number of recent, strong galaxy interactions such as galaxy-galaxy mergers occurring. The skewness of the asymmetry distribution in the outer sample resembles the asymmetry distribution of field galaxies which supports the enhancement of asymmetric galaxies found in the inner sample.

The CAS system was used by Holwerda et al. (2011) to quantify how long neutral hydrogen appears disturbed in galaxy-galaxy mergers. We employ three definitions presented in Holwerda et al. (2011) to measure the fraction of galaxies that are visibly interacting in our samples (Table 2.2). Neutral hydrogen is more sensitive to mergers than the stellar population which will result in the neutral hydrogen appearing disturbed for a longer time (Lotz et al., 2010). Therefore, the fraction of interacting galaxies being measured using the stellar population can be treated as a lower limit. Our main finding in Table 2.2 is that the same fraction of galaxies are visibly interacting in both samples. We find the fraction of interacting galaxies varies according to which definition was used to calculate it which will be due to applying the definitions to the optical photometry, coupled with our photometry having a lower spatial resolution than Holwerda et al. (2011).

Galaxy colours

To probe the effect the cluster merger has on the SFR of the galaxies, we present a three colour (*B-I*, *B-R*, *R-I*) radial analysis in Figure 2.6. The galaxies included are contained within the limits of the wedge in Figure 2.1 and are binned out to a radius of 3 Mpc in 275 kpc bins (similar to Chung et al., 2009). If the merger has a significant effect on the cluster galaxies, this should be reflected by a bluer colour due to starbursting galaxies at the interaction site. There is suggestion of a slight

Table 2.1: The median and skewness of the 5 morphological parameters in the I-band in the inner, outer and field sample. The uncertainty in the inner and outer sample were assigned by the 1σ scatter from the Monte Carlo simulation and the uncertainty in the field sample was assigned by jackknifing 6 equal areas contained in the field sample from Section 2.2.1. The skewness of the asymmetry is significantly higher in the inner sample than the outer and field samples which can attributed to a higher number of recent strong galaxy interactions. There is no further evidence in the median or skewness in the distribution of the other morphological parameters to suggest the population of galaxies is significantly different between the samples.

Parameter	Inner Median	Outer Median	Field Median	Inner Skewness	Outer Skewness	Field Skewness
C	2.17 ± 0.03	2.21 ± 0.02	2.16 ± 0.04	-0.07 ± 0.08	0.39 ± 0.27	0.65 ± 0.42
A	0.20 ± 0.01	0.20 ± 0.01	0.20 ± 0.01	4.43 ± 0.61	1.71 ± 0.39	2.26 ± 0.79
S	0.15 ± 0.01	0.14 ± 0.01	0.14 ± 0.01	3.04 ± 0.53	-2.45 ± 1.92	2.82 ± 0.01
M_{20}	-1.71 ± 0.1	-1.67 ± 0.01	-1.69 ± 0.01	0.96 ± 0.27	2.24 ± 0.35	2.10 ± 0.21
Gini	0.52 ± 0.01	0.52 ± 0.01	0.52 ± 0.01	4.19 ± 0.24	5.50 ± 1.55	7.68 ± 3.93

46

Table 2.2: The fractions of galaxies that are visibly interacting according to three definitions presented in Holwerda et al. (2011). The same fraction of galaxies are visibly interacting in both samples.

Fraction	Inner Sample (%)	Outer Sample (%)
A > 0.4	5.3 ± 1.3	8.6 ± 1.2
G > -0.115M_{20} + 0.384	16.9 ± 1.8	17.3 ± 1.6
G > -0.4A + 0.66	17.0 ± 1.8	17.25 ± 1.6

downward trend in the B-I colour in figure 2.6 demonstrating that the galaxies are becoming bluer at large clustercentric radii. This trend is consistent with the morphology-density relation (Dressler, 1980) but shows no strong enhancement in recent star formation in any part of the cluster.

We contrast this result to Chung et al. (2009), who investigated galaxy colour as a function of radial distance in the Bullet cluster. They found that a shock propagating through the ICM was not powerful enough to induce a starburst from the rapid increase in pressure on the galaxies, resulting in no significant colour change. This demonstrates that galaxy colour can be uniform in different environments within the Bullet cluster which is a more hostile environment than A1664.

We have calculated the Butcher-Oemler blue fraction which defines a galaxy as blue if it is 0.2 bluer than the cluster red sequence in the B-V rest frame (Butcher & Oemler, 1978, 1984). We present Figure 2.7 which plots the blue fraction as a function of limiting magnitude and find there is consistently a higher blue fraction in the outer sample down to all limiting magnitudes. This trend is consistent with the radial colour analysis (Figure 2.6) emphasising that bluer galaxies preferentially reside in less dense environments such as the outskirts of clusters.

2.4   Discussion

There are three pieces of evidence in favour of interpreting A1664 as presently undergoing a minor merger. These are: (i) the extended feature to the South in the X-ray surface brightness image (Figure 2.3), (ii) the cold front in the cluster core seen in the temperature map and (iii) the detected substructure displayed in the adaptively-smoothed unweighted and weighted 2d spatial distribution of cluster galaxies (Figure 2.4 and 2.5). In this section, we discuss the limitations of our data in conjunction with the effects a minor merger has on cluster galaxies.
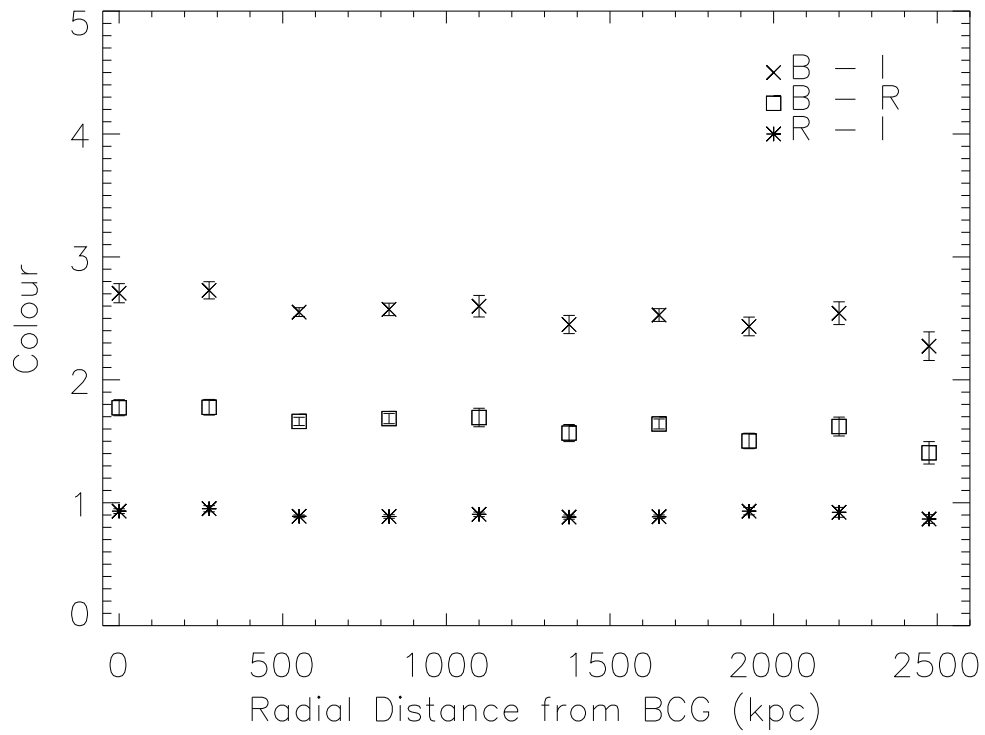
Fig. 2.6: Colour as a function of distance from the BCG where each galaxy was binned into 275 kpc increments. The slight negative trend in the *B-I* colour is consistent with the morphology-density relation and reveals no strong recent star formation at any radii of the cluster.
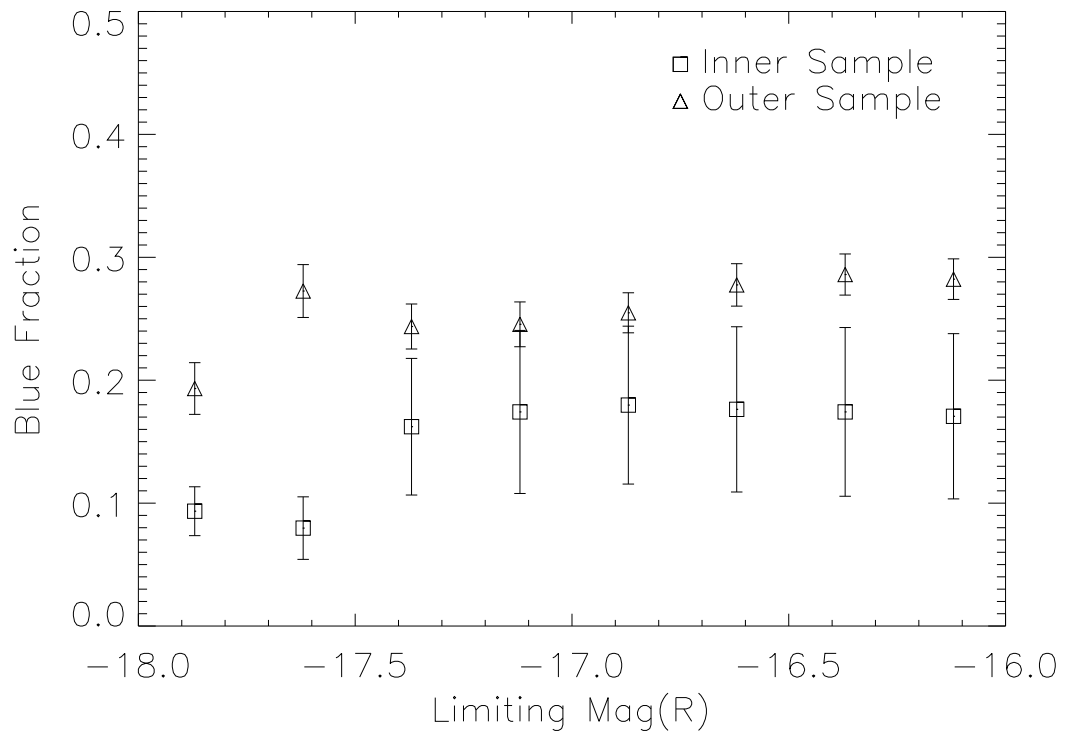
Fig. 2.7: The blue fraction for the two samples as a function of limiting magnitude. The outer sample has significantly higher blue fraction at bright magnitudes and continues to have a higher blue fraction (though not as significant) at faint magnitudes.

If the substructure to the South is the perturber, then it must have passed pericentre as it would be responsible for triggering the cold front in the cluster core. As many cluster galaxies lack redshifts, we are unable to unambiguously confirm that the substructure in Figures 2.4 and 2.5 is the remnant peturber. However this is the most likely scenario for the following reasons: i) The X-ray morphology which appears extended towards the BCG is best explained by emission from the intra group medium of the peturber. ii) The bright galaxy in the yellow circle of Figure 2.1 appears luminous enough to be the brightest group galaxy.

We measure the skewness of the CAS (Conselice, 2003), M_{20} and Gini (Lotz et al., 2004) parameters. This method will be most sensitive to the differences in the galaxy population between the samples as well as galaxies with measured morphological values in the extremities of the distribution. We interpret the higher percentage of asymmetric galaxies found in the inner sample as a result of increased galaxy-galaxy interactions while the group passes through pericentre. As the merging group has travelled passed pericentre, this interpretation is consistent with the work of Vijayaraghavan & Ricker (2013) who showed that galaxy interactions increased during pericentric passage. Due to a higher percentage of late type galaxies residing in the field than clusters, we would expect the field to have a higher skewness of the asymmetric parameter than a relaxed cluster. However, A1664 is not a relaxed cluster and we find a higher skewness of asymmetry in the inner sample which supports the previous result that a cluster mechanism (galaxy-galaxy mergers) is responsible for this increase in asymmetric galaxies.

The major limitation of this morphological analysis is the spatial resolution of our I-band photometry. The biggest consequence is that only the galaxies currently undergoing strong interactions (i.e. recent mergers) will be differentiated from the cluster population. This limitation is the most likely explanation for detecting a difference between the galaxy populations in the asymmetry parameter but not the in the other morphological parameters (Table 2.1) and the disagreement between the definitions of interacting galaxies in Table 2.2.

If galaxies in the cluster were undergoing a starburst, we would expect an enhancement in the blue section of Figure 2.6. We observe a slight negative trend in the most sensitive colour (B-I) but see no significant enhancements of recent star formation in any part of the cluster. We expect to find a similar radial colour trend in relaxed clusters which implies other galaxy transformation mechanisms (such as pre-processing) are able to quench star formation well before interacting with the merging group.

We consistently measure a higher blue fraction in the outer sample of A1664 (Figure 2.7) where the clearest difference is seen in the bright magnitudes. The morphology-density relation (Dressler, 1980) predicts the trend we see in the measured blue fraction. As we measure the blue fraction down to fainter magnitudes, we include less luminous (and therefore less massive) galaxies in our sample which are more sensitive to interactions. Due to this sensitivity, starbursts could be more easily triggered in less massive galaxies. However, the fainter we measure our blue fraction to, the less complete our sample is which increases the uncertainty in our measurements. The colour analysis has shown that A1664 has the same colour properties as a cluster that is not undergoing a minor merger.

2.5 Conclusions

We have presented a detailed analysis using multi-band photometry of the disturbed galaxy cluster A1664. Our main findings from this study are:

- We detect substructure in the smoothed unweighted and weighted 2d galaxy distributions. The substructure coincides with the extended X-ray emission in the South and a local over-density in the optical image. These results are best explained by the substructure being the remnant core of the merging group where the bright optical galaxy is most likely the surviving BCG.

- We find there is a higher percentage of morphologically asymmetric galaxies in the inner region of A1664 when compared to the outer and field samples. The difference between the inner and outer sample is significant to 3.7σ. Due to the limited resolution of our imagery, our morphological analysis will only be able to detect galaxies that are highly asymmetric. It is likely that these galaxies have undergone strong encounters resulting from a higher interaction rate as the merging group passes through pericentre.

- We only detect a variation in the asymmetry parameter between our samples. We believe our spatial resolution was the main reason for not being able to detect variation in the other morphological parameters.

- There is disagreement between the percentage of galaxies interacting according to which definition is implemented. This is also most likely due to the spatial resolution of our photometry.

- The radial colour profile of A1664 has a slight negative trend in the *B-I* colour and a flat trend in the *B-R* and the *R-I* colours. This colour profile shows no enhancement at a specific radial distance from the BCG which indicates no significant recent star formation occurring in the cluster.

- The blue fraction was found to be higher in the outer sample which is consistent with blue galaxies preferentially residing in the outskirts of clusters.

Our work shows that a minor merger has subtle effects on the population of cluster galaxies in A1664 – in the sense that only one interaction signature of many (Holwerda et al., 2011) demonstrated any significant consequence for the galaxies involved. Our morphological analysis is found to be consistent with the work of Vijayaraghavan & Ricker (2013) who show that galaxy-galaxy interactions increase while a group passes through pericentre. The colour of the galaxies in A1664 resembles what we would expect to find in a relaxed (i.e. not merging) cluster. As the population of cluster galaxies is found to be quite uniform, we have not observed any significant galaxy transformations in this environment. It is likely that galaxies are being pre-processed well before they are able to interact with the merging group but it is possible that cluster mechanisms such as rapid strangulation or ram pressure stripping are contributing to the uniformity of cluster galaxies. The techniques used in this analysis can be applied to other clusters undergoing a minor merger that may be identifiable by a cold front. The application to other clusters could help disentangle the effect minor mergers have on clusters which are difficult to observationally detect.

Acknowledgments

Chapter 3

6dFGS Group Finding and Mock Catalogues

3.1 Overview

In this chapter we create two mock catalogues intended for calibrating a friends-of-friends (FoF) algorithm (Huchra & Geller, 1982), that will be used to define galaxy groups in the 6 degree Field Galaxy Survey (6dFGS; Jones et al., 2009). Currently there is no group catalogue for 6dFGS and creating one provides an essential platform for delineating filaments (e.g. Murphy et al., 2011; Alpaslan et al., 2014), a key goal of this thesis. Additionally, it would provide a benchmark in both the creation of mocks and group finding application for the upcoming Taipan survey (da Cuhuna et al. in prep).

The mocks need to reproduce a spatial distribution that quantitatively matches 6dFGS. If they meet this threshold, more can be produced and used to calibrate the FoF algorithm. Although we were unable to create a mock that matched 6dFGS to our satisfaction, important discrepancies between observation and simulation were highlighted in this process. We will pursue the origin of these in future work. A different technique for delineating filaments in 6dFGS was ultimately implemented in Chapter 4, which we describe in detail there.

3.2 Introduction

Quantifying the physical processes in individual galaxy clusters (Chapter 2) is an efficient means of testing galaxy evolution. The high density of galaxies make clusters attractive sites for probing multiple mechanisms responsible for galaxy transformations in a small area. However, galaxy clusters are the densest viralised structures

in the Universe, making them rare where the physical processes can be extreme and unique to the densest environment (e.g. Aragón-Calvo et al., 2010c).

A key goal of this thesis is to quantify the filamentary structure of the local Universe to determine if filament galaxies evolve differently to galaxies far from filaments. There are many attempts in the literature to reliably quantify filaments in galaxy redshift surveys (e.g. Pimbblet, 2005; Stoica et al., 2005; Novikov et al., 2006; Platen et al., 2007; Forero-Romero et al., 2009; Aragón-Calvo et al., 2010a; Sousbie, 2011; Murphy et al., 2011; Smith et al., 2012; Alpaslan et al., 2014; Tempel et al., 2014b; Dehghan & Johnston-Hollitt, 2014; Leclercq et al., 2015). Some of these techniques require a group catalogue to define filaments (e.g. Murphy et al., 2011; Alpaslan et al., 2014; Chen et al., 2015a) where others operate directly on the positions and redshifts of the galaxies (e.g. Platen et al., 2007; Sousbie, 2011; Tempel et al., 2014b; Dehghan & Johnston-Hollitt, 2014; Chen et al., 2015a).

Creating a group catalogue using a redshift survey determines whether a galaxy is part of a group or isolated. The FoF algorithm (Huchra & Geller, 1982) is well tested and a popular method to create a group catalogue. It defines galaxies in a common dark matter halo (i.e. group) by linking galaxies together in accordance with their angular separation, line-of-sight separation and survey selection function. Group catalogues from modern galaxy redshift surveys enable large statistical tests of galaxy evolution. Most modern surveys, such as the 2 degree Field Galaxy Redshift Survey (2dFGRS; Colless et al., 2001), the Sloan Digital Sky Survey (SDSS; Abazajian et al., 2009) and the Galaxy And Mass Assembly survey (GAMA; Driver et al., 2011) have corresponding group catalogues produced from the FoF algorithm (Eke et al., 2004; Berlind et al., 2006; Robotham et al., 2011). Currently, there is no 6dFGS group or filament catalogue and it is an ideal survey for testing galaxy evolution in the nearby Universe. The process of making a 6dFGS group catalogue could ideally be directly applied to Taipan a future redshift survey in the same 6dFGS volume and will be the most comprehensive spectroscopic survey of the southern hemisphere (Hopkins et al., 2014).

6dFGS is a wide angle galaxy redshift survey and offers a homogeneously-selected galaxy sample in the nearby Universe. The survey measured redshifts and peculiar velocities in the southern hemisphere beyond $|b| > 10°$ (Jones et al., 2004, 2009). There are 125 071 galaxies with observed redshifts and the median redshift of the survey is $z_{\frac{1}{2}} = 0.053$. The survey is near-complete at $(K, H, J, r_{\mathrm{F}}, b_{\mathrm{J}}) \leq (12.65, 12.95, 13.75, 15.60, 16.75)$ where the JHK photometry is taken from the 2MASS

extended source catalogue (Jarrett et al., 2000) and the b_J and r_F photometry are from the SuperCOSMOS catalogue (Hambly et al., 2001b,a).

Through hierarchical growth, the majority of galaxies reside in groups. Producing a group catalogue from 6dFGS enables us to test fundamental ideas of galaxy evolution in group environments from a survey that is not subject to cosmic variance. For example, galaxy transformations have been shown to occur in group environments (Konstantopoulos et al., 2013) and pre-processing in groups is needed to explain the quenching of galaxies prior to entering high density environments (e.g. Mahajan, 2013; Vijayaraghavan & Ricker, 2013; Haines et al., 2015; Odekon et al., 2016). It is unclear at what scale environmental mechanisms dominate the evolution of galaxies (Mendel et al., 2011). To test this, we can use a statistically large sample of galaxy groups in 6dFGS. However, to achieve this, we need to create a reliable group catalogue using 6dFGS, which takes proper account of redshift space distortions and can define filaments of galaxies in the manner of Murphy et al. (2011).

3.3 Friends of Friends Algorithm

The FoF algorithm (Huchra & Geller, 1982) is a popular method for creating group catalogues and has been used on 2dFGRS, SDSS and GAMA (Eke et al., 2004; Berlind et al., 2006; Robotham et al., 2011). It determines which galaxies are part of bound structures using only their positions and redshifts. First, the algorithm finds friends of a galaxy by searching for other galaxies within a linking volume. If no friends are found, the galaxy is considered isolated and the algorithm moves onto the next galaxy. For a galaxy with friends, the algorithm searches for friends-of-friends by adding galaxies within the linking volume centred on each friend. This continues until no further friends are found and the set of galaxies is considered a group. Clearly, the choice of linking volume is crucial for the FoF algorithm to return groups of galaxies that trace true gravitationally bound structures.

The FoF algorithm is intuitive in n-body simulations where distances between galaxies are measured in Cartesian co-ordinates and can be directly related to the radii of the (spherical) dark matter halos. This is not the case for galaxy redshift data, where redshift space distortions cause bound structures to be smeared out in the redshift direction, an effect known as 'fingers-of-god'. To account for this finger-of-god effect, a cylindrical linking volume is used that is constructed for each galaxy

using a perpendicular ($\ell_\perp$) and parallel ($\ell_\parallel$) linking length. The linking lengths chosen for each galaxy should scale with the varying average number galaxies as a function of redshift for a magnitude-limited redshift survey. As these depend on the survey selection function, the linking lengths need to be calibrated in mocks that reproduce the features of the survey. This reveals the optimal linking lengths needed to trace true gravitational structures and quantifies the systematics associated with those values.

We use the K-band input target catalogue of 6dFGS to calculate linking lengths in preparation for defining groups of galaxies. This is the largest single photometric band catalogue containing $88\,610$ galaxies and completeness measurements for each galaxy that is essential for measuring the number density. For 6dFGS, we follow the prescription of Eke et al. (2004) who created the 2dFGRS Percolation-Inferred Galaxy Group (2PIGG) catalogue.

The number density of a complete sample of galaxies can be measured by integrating the luminosity function (LF). However, flux limited surveys (like 6dFGS) are not complete and the number density varies as a function of redshift (i.e. more galaxies are being missed at further distances) and sky position (i.e. whether a particular part of the sky was observed enough to measure all the galaxies within the flux limits). The number density is measured for each galaxy using

$$n(z, \theta) = \int_{k_{bright}}^{k_{lim}(\theta)} \Phi[M(k, z)] c_z(k, \theta) \, \mathrm{d}k, \tag{3.1}$$

which is an integration of the LF $\Phi[M(k, z)]$, for the apparent magnitude k at redshift z. The LF is weighted by the completeness of the galaxy $c_z(k, \theta)$, with apparent magnitude k at sky position θ. The weighted LF is then integrated from the bright flux limit (k_{bright}) down to the limiting flux of the survey seen at that sky position ($k_{lim}(\theta)$).

To determine the linking volume for each galaxy, we first compute the perpendicular linking length in the same manner as Eke et al. (2004), using

$$\ell_\perp = \min \left[\frac{b}{n^{1/3}}, L_{\perp,\mathrm{max}}(1+z) \right]. \tag{3.2}$$

The perpendicular linking length is chosen as the minimum value between the galaxy bias b scaled by the number density n (from equation 3.1) and the physical upper

limit perpendicular linking length $L_{\perp,\max}(1+z)$. The galaxy bias sets the physical size for galaxies to share a common dark matter halo. In n-body simulations, dark matter haloes are identified using a FoF algorithm with a well tested linking length of $b = 0.2$ times the mean interparticle separation. However, the extent to which galaxies in redshift surveys trace dark matter halos is entirely dependant on the survey selection function. Therefore, the choice of b is unique to the survey and should account for the unobserved galaxies in order to link galaxies that share a common dark matter halo. As the perpendicular linking length scales with $n^{-1/3}$, small number densities can produce unrealistically large linking lengths. To ensure $\ell_\perp$ is realistic, a maximum linking length ($L_{\perp,\max}$) is implemented in the choice of linking length. We use $L_{\perp,\max} = 2\ h^{-1}$ Mpc (which is then scaled with redshift in equation 3.2) as Eke et al. (2004) found this value produced the most realistic groups with the least contamination.

To construct the cylindrical linking volume, we now calculate the parallel linking length with

$$\ell_\parallel = R\ell_\perp, \tag{3.3}$$

where R is the elongation factor that stretches out the linking volume in the line-of-sight direction. The choice of R is inherent to the survey and directly influences which group properties are recovered best. Fig. 3.1 is from Berlind et al. (2006) and shows the group properties in the parameter space of the perpendicular and parallel linking lengths. There is no combination of b and R that can simultaneously recover true membership, projected size and velocity dispersion. This is because it is very difficult to trace the underlying dark matter distribution in redshift space. The choice of b and R should reflect the survey selection function and the aim of the group catalogue (e.g. to recover accurate group membership, realistic velocity dispersions or a compromise of both). Eke et al. (2004) chose b = 0.13 and R = 11, favouring group size and velocity dispersion while Berlind et al. (2006) chose b = 0.14 and R = 5.4 which returned groups with accurate group membership and projected sizes.

With suitable values for b and R, two galaxies i and j are considered friends and are linked together if

$$\theta_{ij} \leq \frac{1}{2}\left(\frac{\ell_{\perp,i}}{d_{c,i}} + \frac{\ell_{\perp,j}}{d_{c,j}}\right), \tag{3.4}$$

and
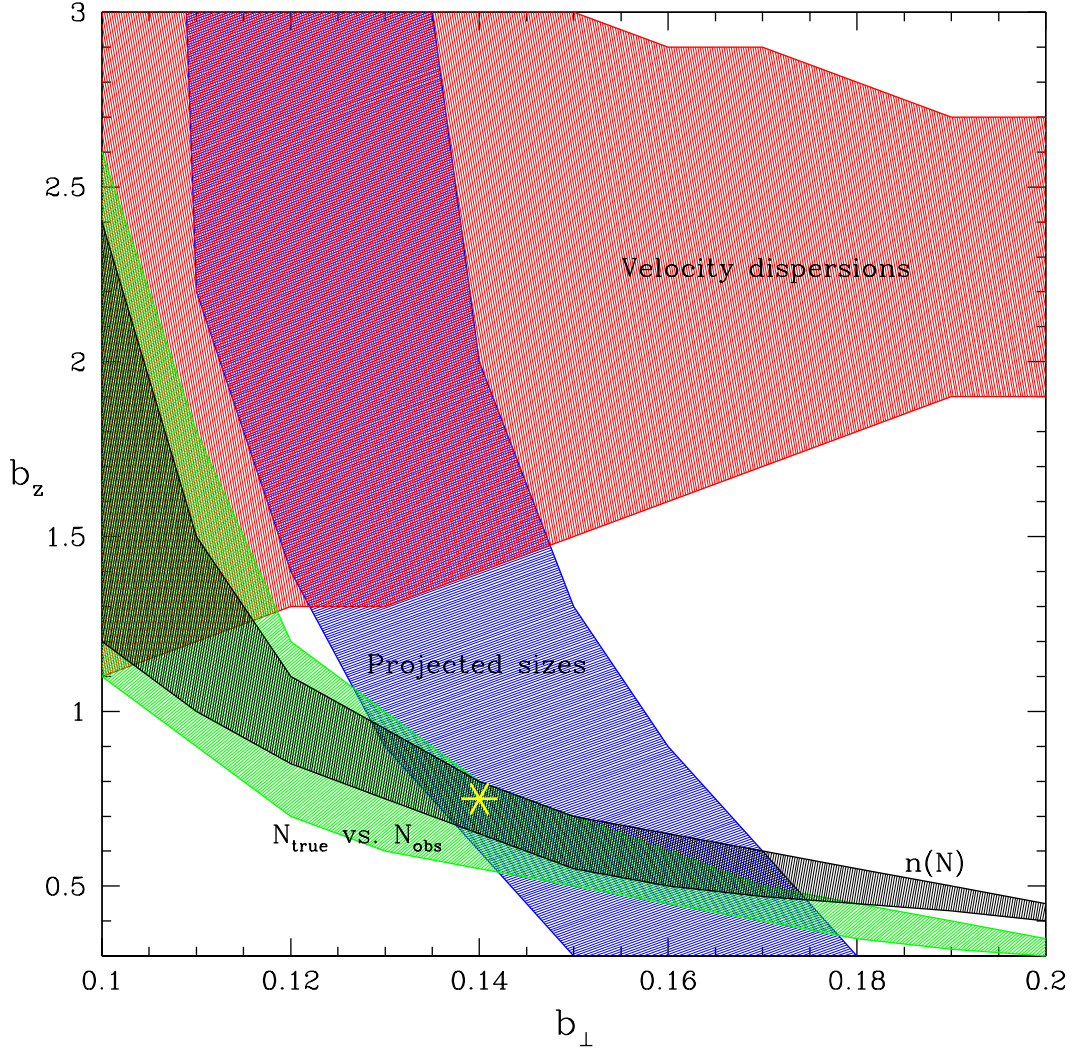
Fig. 3.1: The linking length parameter space from Berlind et al. (2006) where $b_\perp$ and b_z are the same as $\ell_\perp$ and $\ell_\parallel$. Each coloured-shaded region is a different measurable property of a group of galaxies where the multiplicity function is in black, the one-to-one matched halo and group richness is green, projected size in blue and velocity dispersion in red. There are no combination of linking lengths that return all desired group properties and the choice of linking lengths (yellow star are the values used in Berlind et al., 2006) should reflect the aim of the group catalogue.

$$|d_{c,i} - d_{c,j}| \leq \frac{\ell_{\parallel,i} + \ell_{\parallel,j}}{2}, \tag{3.5}$$

where θ_{ij} is the angular separation, $d_{c,i}$ and $d_{c,j}$ are the comoving distances of the galaxies.

Using a FoF algorithm to identify galaxy groups in this way, the two unknown quantities are the galaxy bias (b) in equation 3.2 and the elongation factor (R) in equation 3.3. These are unique to each galaxy redshift survey as they reflect the survey selection function and are calibrated to return a group catalogue with specific properties (e.g. accurate group membership). To choose applicable values for b and R in 6dFGS, a mock needs to be created that reproduces the features of 6dFGS.

3.4 Creating 6dFGS mocks

The purpose of creating a 6dFGS mock is to calibrate the unknown parameters of the FoF algorithm. As the mock is produced from a simulation created in real space, it is known which galaxies belong in groups. To make the mock, we need to determine which galaxies would be observed with the 6dFGS survey parameters. To achieve this, we do the following:

1. Produce a light-cone that matches the 6dFGS geometry and maximum redshift of the survey.

2. Ensure the magnitudes of the galaxies produced by the simulation are realistic. If they are not, populate the dark matter halos with galaxies from the 6dFGS LF.

3. Replicate the 6dFGS selection function by only retaining galaxies that would be observed within the survey flux limits while accounting for observational completeness.

3.4.1 The Theoretical Astrophysical Observatory

The Theoretical Astrophysical Observatory[1] (TAO) is an online virtual laboratory that hosts mock observations of galaxy surveys (Bernyk et al., 2016). It is designed

---

[1]https://tao.asvo.org.au/tao/

to produce mocks tailored to the needs of an individual without the user requiring expert knowledge in galaxy modelling, simulation techniques, software development or access to high performance computing.

TAO gives the user access to multiple n-body dark matter simulations, semi-analytic galaxy formation models, a multitude of dark matter and galaxy properties from the simulations. To create a mock using TAO, the user is able to select:

- A box or light-cone geometry.

- The size and redshift of the box or the RA, Dec and z limits for the light-cone.

- The dark matter prescription: Millennium, Mini-Millennium (Springel et al., 2005b) or Bolshoi (Klypin et al., 2011).

- A semi-analytic galaxy formation model. Currently, the only model available is the Semi-Analytic Galaxy Evolution model (SAGE; Croton et al., 2016) but more models will be available in future TAO versions.

- Measurements of galaxy masses (e.g. total stellar mass, cold gas mass), galaxy properties (e.g. total star formation rate, time of last merger), halo properties (e.g. virial mass, maximum circular velocity), positions and velocities (RA, Dec, z) and simulation information (e.g. central galaxy ID).

- The application of a spectral energy distribution (SED). There is a choice of three single stellar population models (Bruzual & Charlot, 2003; Maraston, 2005; Conroy et al., 2009) using the Chabrier, Kroupa or Salpeter initial mass function (IMF).

- Apparent and absolute magnitudes in a wide range of filters (e.g. SDSS, 2MASS, GALEX, HST) including a Slab (Devriendt et al., 1999) or Calzetti (Tonini et al., 2012) dust model.

To make a 6dFGS mock from TAO, we select a light cone with $0 < \alpha \leq 360$, -90 $< \delta \leq 0$ and $0 < z \leq 0.2$ using the Millennium dark matter prescription (Springel et al., 2005b). SAGE (Croton et al., 2016) was selected with the Conroy et al. (2009) stellar population model, Kroupa IMF and Calzetti dust model (Tonini et al., 2012). Apparent and absolute magnitudes were selected in the 2MASS Ks filter and we selected the halo maximum circular velocity (V_{max}) and subhalo maximum circular velocity at infall (V_{max}^{sub}). The galactic plane ($|b| < 10°$) was removed from the mock which now matches the geometry of 6dFGS.

3.4.2   A Mock using Sub Halo Abundance Matching

Even though TAO provides 2MASS K-band magnitudes from SAGE and SED fitting, we found there was a significant offset between TAO and 6dFGS magnitudes (resulting in offset LFs). We assumed the 2MASS K-band magnitudes produced by TAO were calibrated in the same system as the 2MASS K-band magnitudes in 6dFGS. However, only recently (August 2016) we discovered the K-band magnitudes produced by SAGE and SED fitting are calibrated to the AB system, where 6dFGS is calibrated to Vega. In Chapter 3.4.3 we create a mock using the SAGE galaxies with corrected magnitudes but originally we searched for an alternate method to make a mock using the underlying dark matter distribution from TAO without using the TAO magnitudes.

For this mock, we use Sub Halo Abundance Matching (SHAM) to populate each dark matter halo with galaxies from the observed 6dFGS LF (SHAM; Conroy et al., 2006). SHAM is a non-parametric model that monotonically relates the luminosity of a galaxy to V_{max}. By design, it reproduces the LF and has excellent agreement with the two-point correlation function at a variety of redshifts (Conroy et al., 2006; Conroy & Wechsler, 2009). The two-point correlation function is a statistical quantification of the spatial distribution, the most important feature the mock must reproduce.

For N halos in TAO, we produce N luminosities from the 6dFGS K-band LF (Jones et al., 2006). The Schechter function fitted to the LF of 6dFGS takes the form

$$\phi(M)\mathrm{d}M = 0.4 \ln 10 \; \phi_* \frac{(10^{0.4(M_*-M)})^{\alpha+1}}{\exp\,[10^{0.4(M_*-M)}]} \; \mathrm{d}M, \tag{3.6}$$

where $M_* - 5 \log h = -23.83$ mag, $\alpha = -1.16$ and $\log[\phi_*] = -2.126 \; h^3 Mpc^{-3}$ in the K-band. We use $h = 0.73$ to match the cosmology of the Millennium simulation that created the dark matter halos in this mock.

The distribution of luminosities selected from equation 3.6 need to match the distribution of luminosities observed in the Universe. To achieve this, we treat the Schechter function as a probability density function and select N galaxies using the following prescription:

1. Choose a random luminosity (M_{rand}) between the bright and faint limits of the LF.

2. Determine the corresponding $\phi(\mathrm{M}_{rand})$ using equation 3.6 where $M = M_{rand}$.

3. Generate a random number density (ϕ_{rand}) between the minimum and maximum number densities in the LF, set by the brightest and faintest magnitude bins.

4. If $\phi(\mathrm{M}_{rand}) > \phi_{rand}$, M_{rand} is retained. Otherwise, return to step 1.

This process ensures there is a higher probability of retaining a faint galaxy than a bright galaxy. Before placing the galaxies in the halos, we select V_{max} according to

$$V_{max} = \begin{cases} V_{max}, & \text{for halos} \\ V_{max}^{sub}, & \text{for sub halos,} \end{cases} \tag{3.7}$$

where V_{max}^{sub} is the maximum circular velocity of the sub halo at the time of infall onto a halo. V_{max} is closely related to halo mass and this choice of V_{max} ensures that under-luminous galaxies are not placed into sub halos.

To determine which galaxies are assigned to each halo, the monotonic relation between the luminosity of a galaxy and V_{max} from equation 3.7 is assumed. This is the only assumption and is the foundation of SHAM. The relation is expressed as

$$n_g(> L_i) = n_h(> V_{max,i}), \tag{3.8}$$

where n_g and n_h are the number density of galaxies and halos. Provided the number densities of the galaxies and halos are the same, the luminosities (populated from the LF) are ranked from brightest to faintest and the halos are ranked from largest V_{max} to smallest. Therefore, there is one galaxy per (sub) halo and the brightest galaxy is assigned to the halo with the highest V_{max}, the second brightest galaxy to the second largest V_{max} etc.

As we are producing luminosities in the same volume as the halos, creating the same number of luminosities as halos automatically matches the number densities. A key feature of SHAM is the galaxies populating the halos will reproduce the LF by design, as we show in Fig. 3.2.
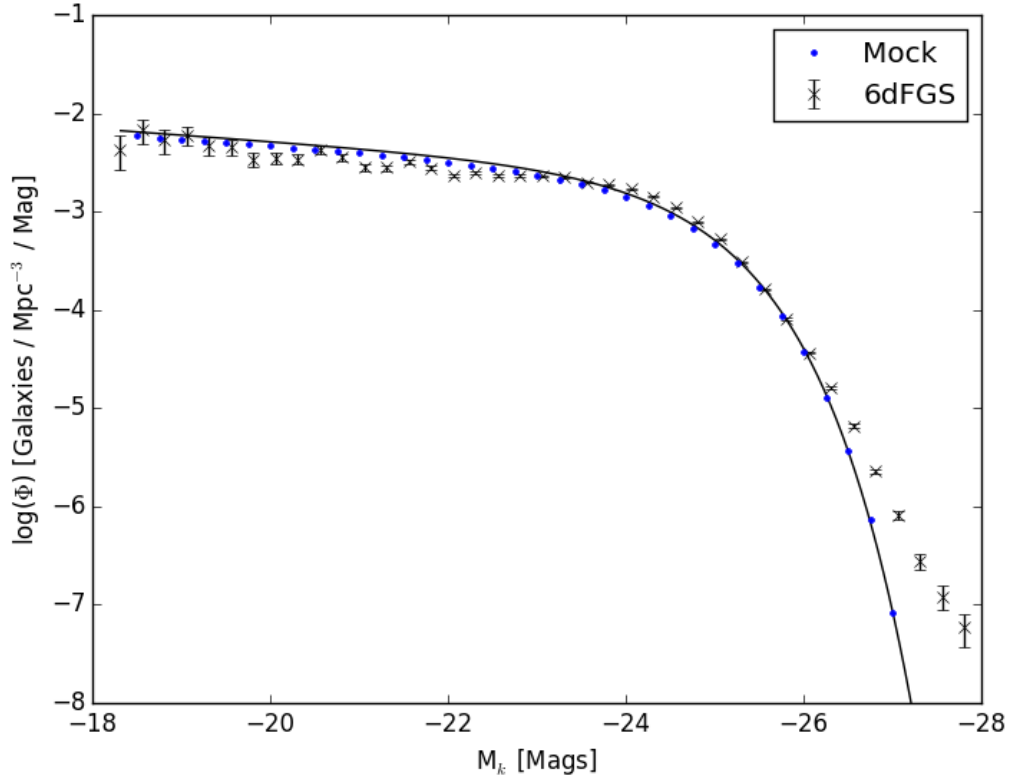
Fig. 3.2: The 6dFGS K-band luminosity function (black crosses) and Schechter function (black line) from Jones et al. (2006) in a cosmology of $h = 0.73$. The Schechter function was used to produce the luminosities that populated the dark matter halos with SHAM. The blue points show the LF of the mock (with uncertainties too small to show), produced by SHAM. There is almost an exact match between the mock LF and the 6dFGS Schechter function, as expected.

3.4.3 A Mock using SAGE galaxies

The K-band magnitudes produced by SAGE and SED fitting are calibrated to the AB system. We convert the TAO magnitudes using

$$K(\text{Vega}) = K(\text{AB}) - 1.843, \tag{3.9}$$

from Blanton & Roweis (2007), which calibrates the magnitudes to Vega. This mock now has apparent and absolute K-band magnitudes which can be directly compared to the 2MASS K-band magnitudes in 6dFGS.

3.4.4 Accounting for the 6dFGS selection function

The selection function of a galaxy survey describes which galaxies have be observed in the survey. It is unique to each survey and depends on the input catalogue(s), flux limits and completeness maps. The 6dFGS selection function needs to be applied to the mocks in order for them to be a realistic representation of 6dFGS. After applying the 6dFGS selection function to the mocks, they should reproduce the key features of the survey.

Currently, the mock created using SHAM does not have apparent magnitudes for the galaxies, it only contains absolute magnitudes. To determine apparent magnitudes we first calculate a k-correction for each galaxy using Poggianti et al. (1999) and apparent magnitudes are obtained through

$$k = K + 5\log(D_L) - 5 + k_{corr}, \tag{3.10}$$

where K is the absolute K-band magnitude, D_L is the luminosity distance to the galaxy in pc and k_{corr} is the k-correction. Now that both the SHAM and SAGE mocks have apparent magnitudes, we impose the 6dFGS flux limits by only retaining galaxies with $8.75 < k < 12.75$.

In their current form, the mocks are 100% complete within flux limits of 6dFGS. However, 6dFGS is not 100% complete within the flux limits as the galaxies observed in the survey depends on the galaxy density and number of observations achieved at each sky position.

Table 3.1: The field and its respective completeness fraction range. Each galaxy in the 6dFGS K-band catalogue has a field assigned to it according to its magnitude, galaxy density and how many galaxies were observed from the input catalogue, for each pointing. These fields were assigned to the mock galaxies to reproduce the selection function of 6dFGS.

Field	Completeness fraction range
1	$0.9 - 1.0$
2	$0.8 - 0.9$
3	$0.7 - 0.8$
4	$0.6 - 0.7$

Each galaxy in the 6dFGS K-band catalogue has been assigned a completeness field based on the number of observed galaxies compared to the number of galaxies in the input catalogue, for a given magnitude in each 6dFGS pointing (Jones et al., 2009). As the completeness is a function of the input catalogue, it takes into account the varying galaxy density across the sky as well as galaxies unable to be observed due to fibre collisions. The completeness fields and the range of their respective fractions are shown in table 3.1.

To apply the same completeness to the mocks, each mock galaxy is assigned the field (from table 3.1) of the nearest 6dFGS galaxy within 5 square degrees with the closest apparent magnitude. If there is no 6dFGS galaxy within 5 square degrees or the magnitude difference between the mock and 6dFGS galaxy is greater than 0.1 mag, the mock galaxy is removed. For mock galaxies with completeness fields, a Monte Carlo simulation is run in the following manner:

1. Generate a random field probability (P_{Field}) between the limits of the respective field.

2. Generate a random probability (P_{Rand}) between 0 and 1.

3. If $P_{Field} > P_{Rand}$, the mock galaxy is retained. Otherwise, the galaxy is removed from the mock.

This ensures mock galaxies with a high completeness field are more likely to be retained than galaxies with a lower completeness field. Removing galaxies based on their completeness field is the final step of applying the 6dFGS selection function to the mocks and they should now reproduce the unique features of 6dFGS.

3.5 Comparison of the mocks to 6dFGS

Before using the constructed mocks to calibrate the FoF linking lengths, we need to ensure the mocks are a good representation of 6dFGS. By comparing the observable properties of 6dFGS to the mocks, we can directly test how well mocks reproduce the unique properties of the survey.

3.5.1 Magnitude distributions

We qualitatively compare the absolute K-band magnitude as a function of redshift for 6dFGS (Fig. 3.3) to the SHAM mock (Fig. 3.4) and the SAGE mock (Fig. 3.5).

For a galaxy to be observed in 6dFGS, its apparent brightness must reside within the flux limits. Therefore, galaxies within a characteristic absolute magnitude range will be observed at each redshift where the range incorporates brighter luminosities at further distances. The mocks should display the same distribution as 6dFGS (Fig. 3.3), otherwise galaxies outside the 6dFGS flux limits (which shouldn't be observed) are being included.

In order to compare the absolute magnitudes of SHAM galaxies to 6dFGS, we construct Fig. 3.4 that shows the absolute magnitude of SHAM mock galaxies a function of redshift. It displays the same distribution as 6dFGS although there is less scatter in the bright SHAM mock galaxies.

Similarly, to compare the absolute magnitudes of the SAGE mock galaxies in the same manner, we construct Fig. 3.5, that shows the absolute magnitude of SAGE mock galaxies as a function of redshift. It displays the same distribution as 6dFGS although there is more overall scatter amongst the distribution.

We qualitatively compare the apparent K-band magnitude as a function of redshift for 6dFGS (Fig. 3.6) to the SHAM mock (Fig. 3.7) and the SAGE mock (Fig. 3.8). In the same style as the previous comparisons, the purpose is to ensure the mocks observe the same simulated galaxies that 6dFGS observe in the Universe.

Fig. 3.6 shows the apparent magnitude of 6dFGS galaxies as a function of redshift. Only faint galaxies are observed at high redshifts and the distribution has a characteristic shape that should be replicated in the mocks.

To compare the apparent magnitudes of SHAM mock galaxies to 6dFGS, we construct Fig. 3.7 that shows the apparent magnitude of SHAM mock galaxies as a function of
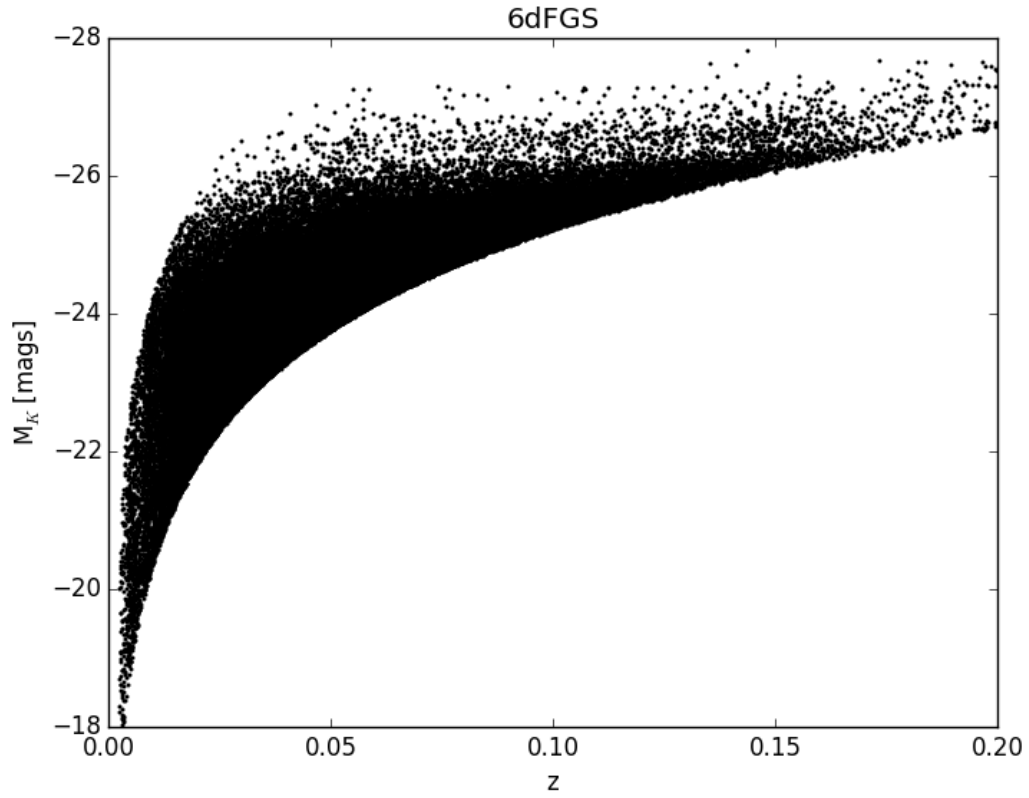
Fig. 3.3: The absolute magnitude of 6dFGS K-band galaxies as a function of redshift. The lower and upper magnitude limits at each redshift are an effect of the 6dFGS flux limits. These limits shift to brighter luminosities for increasing redshifts.
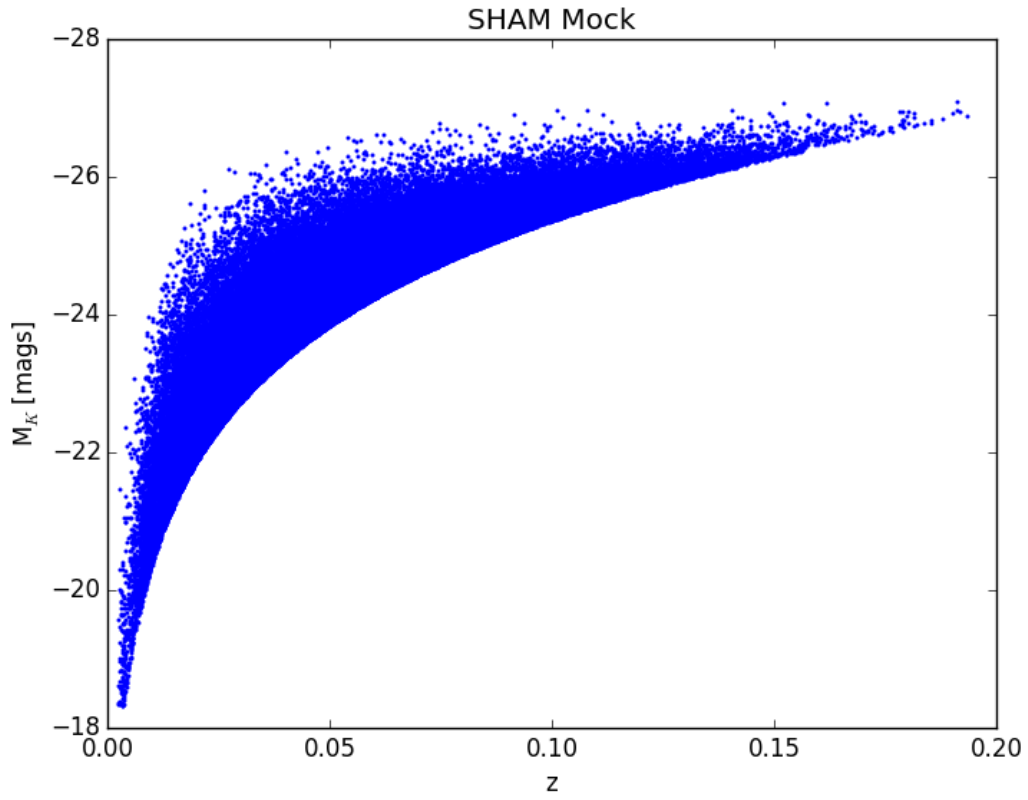
Fig. 3.4: The absolute magnitude of SHAM mock galaxies as a function of redshift. The distribution is remarkably similar to 6dFGS albeit the higher magnitudes display less scatter than 6dFGS.
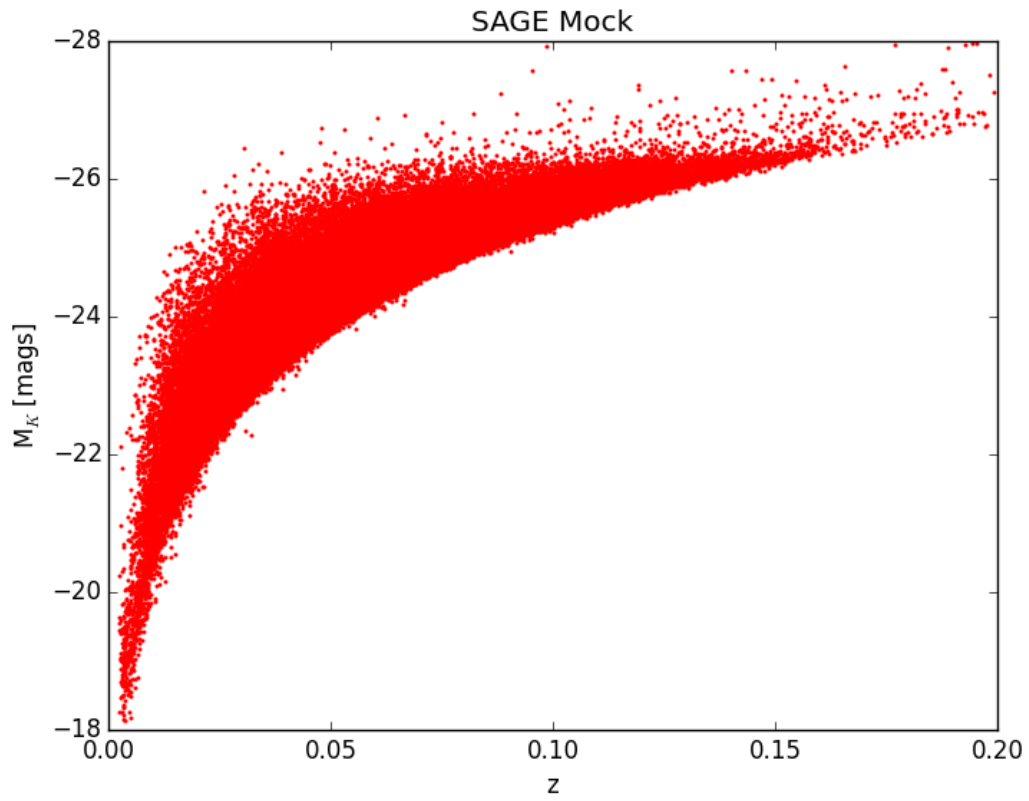
Fig. 3.5: The absolute magnitude of SAGE mock galaxies as a function of redshift. The distribution is remarkably similar to 6dFGS, however there is greater scatter throughout the distribution.
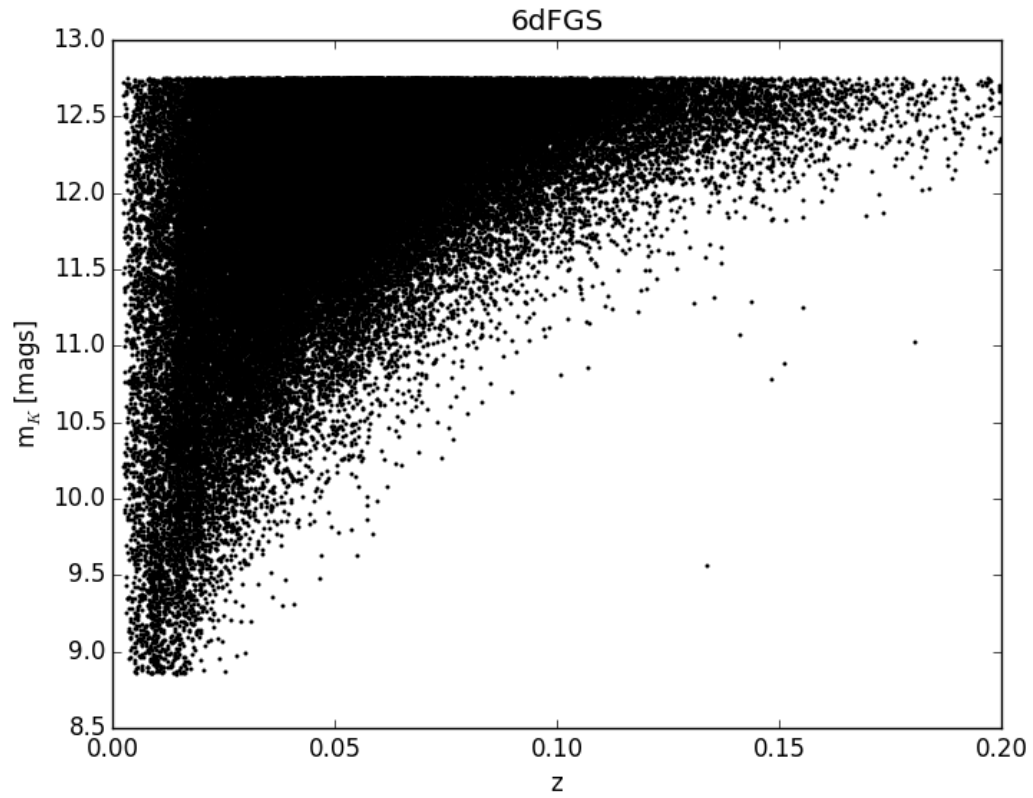
Fig. 3.6: The apparent magnitude of 6dFGS K-band galaxies as a function of redshift. With increasing redshift, only fainter galaxies are able to be observed.
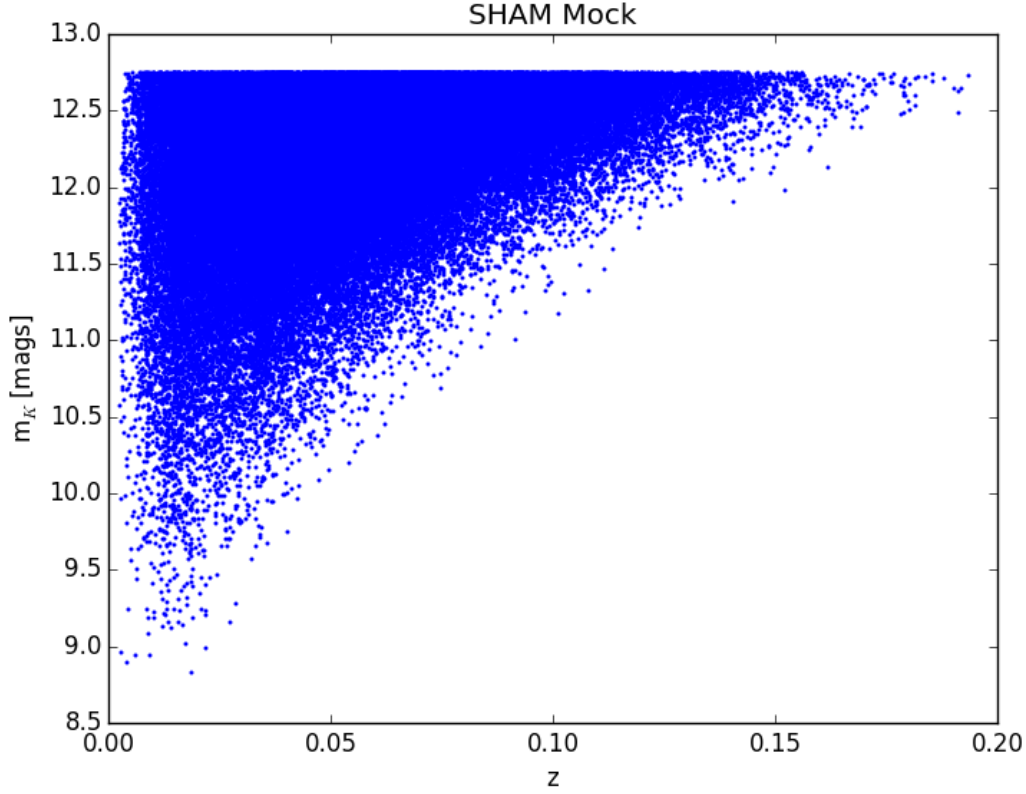
Fig. 3.7: The apparent magnitude of SHAM mock galaxies as a function of redshift. The distribution has the same trend as 6dFGS, although there is less scatter and fewer bright galaxies at low redshift in comparison.

redshift. It displays the same trend of only faint galaxies being observed at higher redshifts. However, there is less scatter in this distribution and there are fewer bright galaxies at low redshift when compared to 6dFGS.

Similarly, to compare the apparent magnitudes of the SAGE mock galaxies in the same manner, we construct Fig. 3.8 that shows the apparent magnitude of SAGE mock galaxies as a function of redshift. It has a similar scatter as 6dFGS and displays the same trend of only faint galaxies being observed at higher redshifts. Like the SHAM mock, there are fewer bright galaxies at low redshift when compared to 6dFGS.

The qualitative comparisons of the absolute and apparent magnitude distributions between the mocks and 6dFGS show the mocks observe the same galaxies in the simulations as 6dFGS observes in the Universe. The SHAM mock has the least scatter compared to the SAGE mock and 6dFGS. This is due to the simplicity of SHAM which populates dark matter halos with galaxies directly sampled from the luminosity

72
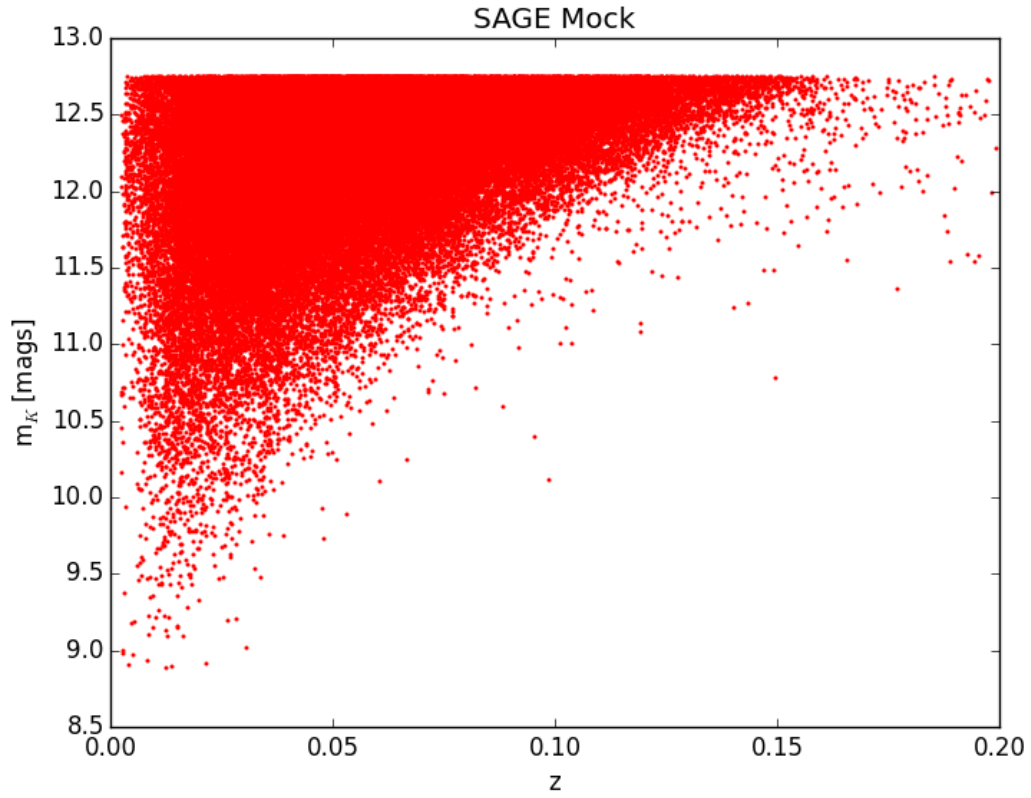
Fig. 3.8: The apparent magnitude of SAGE mock galaxies as a function of redshift. The distribution has the same trend and scatter as 6dFGS. However, there are fewer bright galaxies at low redshift in comparison.

function. The SAGE mock has a similar scatter to 6dFGS which is inherent to the complexities of the semi-analytics models in SAGE. Overall, the SHAM and SAGE mocks mimic the 6dFGS magnitude distributions where the discrepancies can be attributed to the different initial conditions of the simulation compared to the observable Universe. Specifically, there are more bright galaxies in the 6dFGS low redshift Universe compared to the number of bright galaxies produced in the low redshift Universe of these simulations.

3.5.2   Redshift distribution

The number of galaxies observed as a function of redshift is the result of the 6dFGS flux limits. A mock that is a good representation of 6dFGS is expected to have the same redshift distribution.

There are $88\,527$ galaxies in the K-band 6dFGS catalogue, $96\,815$ galaxies in the SHAM mock and $78\,391$ galaxies in the SAGE mock. In Fig. 3.9 we compare the normalised redshift distribution of 6dFGS to the mocks. The median redshifts of 6dFGS, the SHAM and SAGE mock are $z_{\frac{1}{2}} = 0.051$, 0.052 and 0.052 respectively. The three distributions show excellent agreement with the same median and extremely similar overall shape. The only potential systematic is a slightly higher percentage of (SHAM and SAGE) mock galaxies between $0.08 < z \leq 0.12$. It is not expected that the redshift distributions of 6dFGS and the mocks have the same heterogeneous features as each other. 6dFGS contains different cosmological structures to the ones created in the simulations which is reflected in the heterogeneous features of the redshift distributions.

3.5.3   Spatial distribution

For the mocks to be a good representation of 6dFGS, they should only contain galaxies in the regions where 6dFGS galaxies were observed and incomplete regions (due to fewer repeat observations) should be replicated. These features can be viewed in Fig. 3.10, 3.11 and 3.12 where we compare the spatial distribution of galaxies with $0.0025 < z \leq 0.05$ in 6dFGS to the SHAM and SAGE mock.

These figures show galaxies in the Southern sky with $|b| > 10°$. An example area of low completeness in 6dFGS is the position $\alpha = 85°$, $\delta = $ -8° in Fig. 3.10. The

74
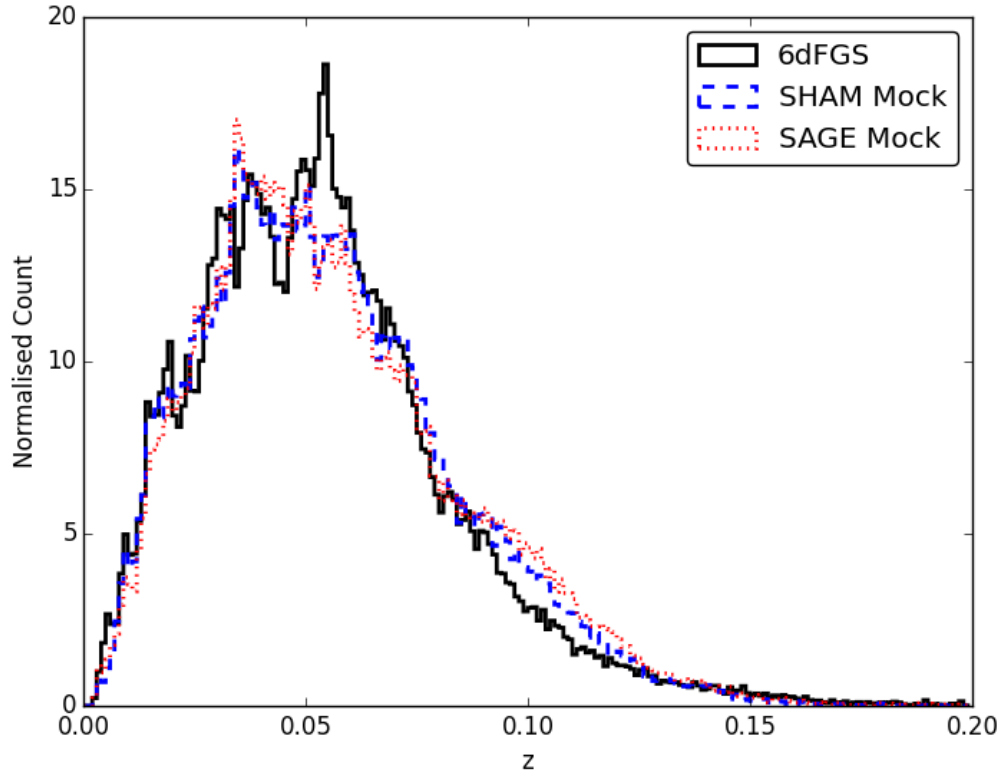
Fig. 3.9: The normalised redshift distributions of 6dFGS (black solid), the SHAM (blue dashed) and SAGE mock (red dotted). The shape of the distributions are very similar where the medians are almost identical with $z_{\frac{1}{2}} = 0.051$, 0.052 and 0.052 for 6dFGS, the SHAM and SAGE mock.
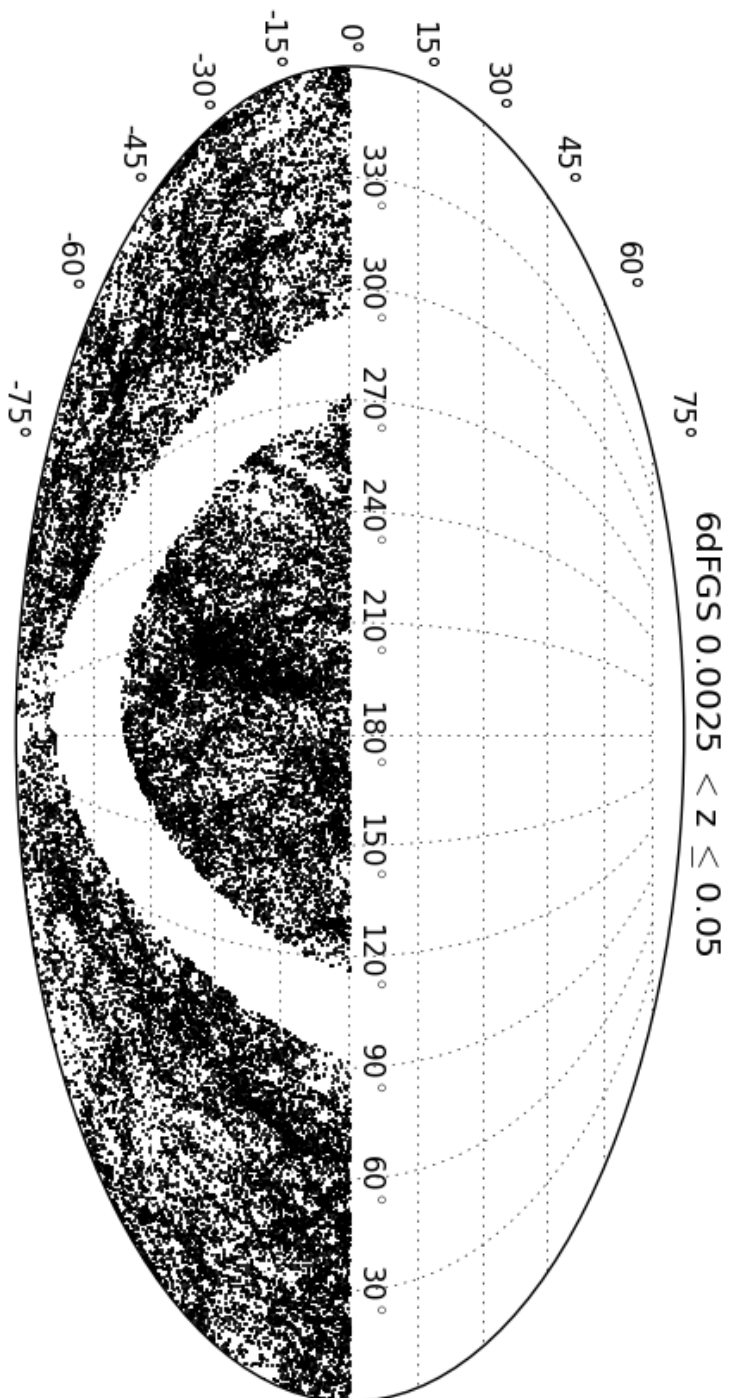
Fig. 3.10: A mollweide projection of the 6dFGS K-band catalogue. Only the galaxies with $0.0025 < z \leq 0.05$ are being displayed to highlight the over and under densities of 6dFGS.

76
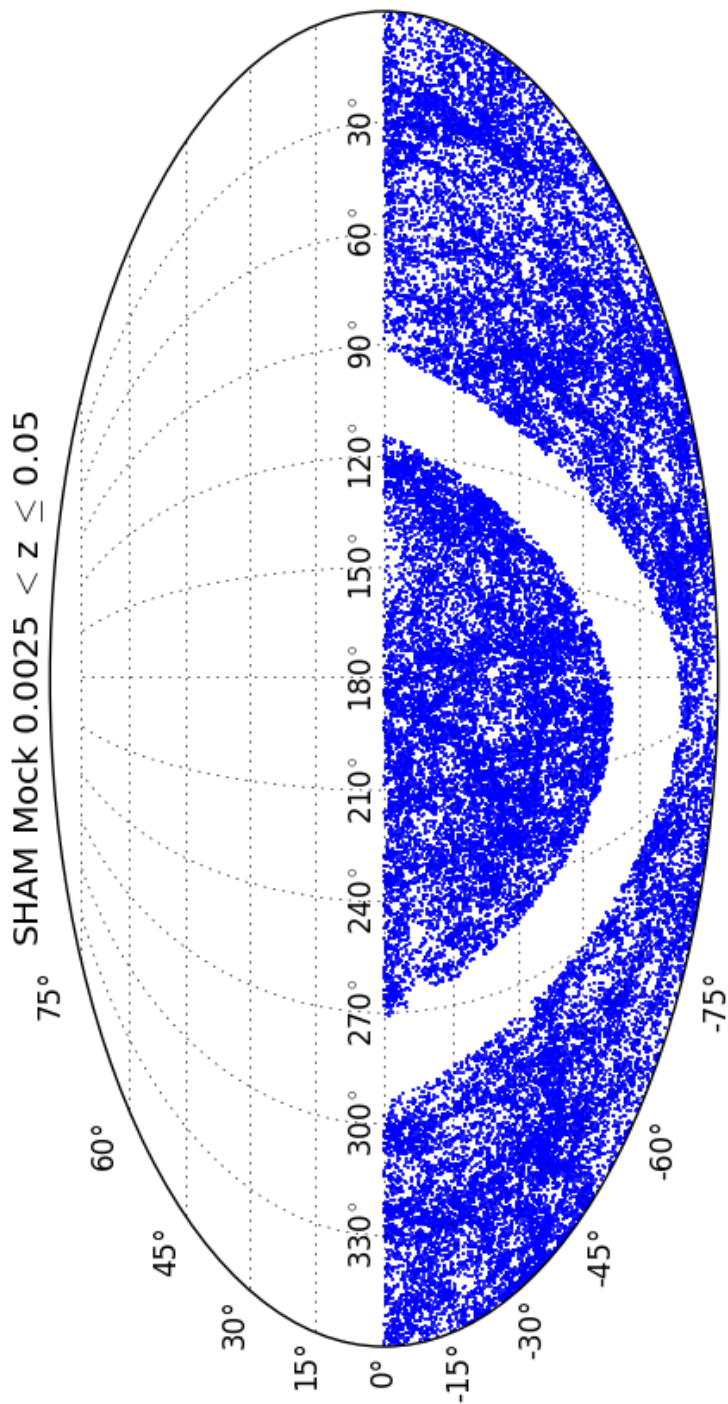
Fig. 3.11: A mollweide projection of the galaxies in the SHAM mock. The same redshift range ($0.0025 < z \leq 0.05$) is displayed to highlight the over and under densities of the mock.
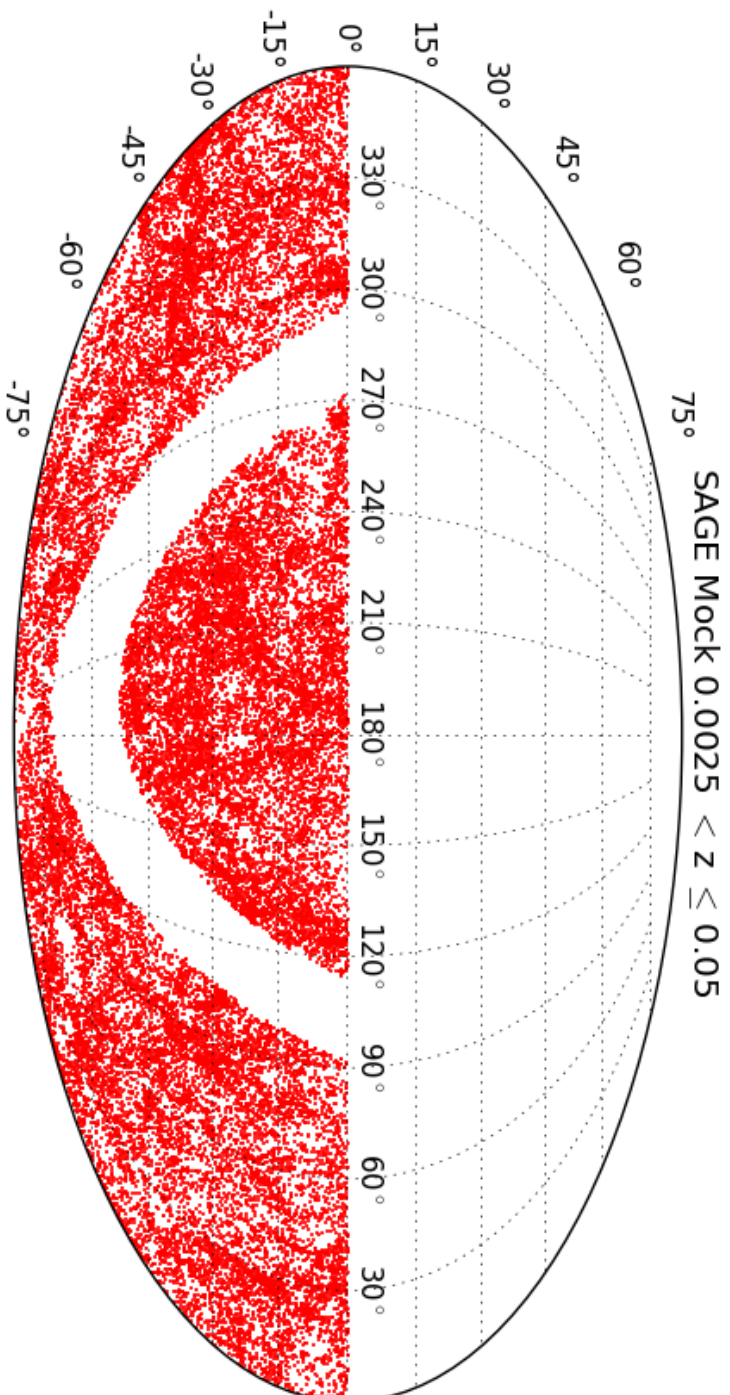
Fig. 3.12: A mollweide projection of the galaxies in the SAGE mock. The same redshift range (0.0025 < z ≤ 0.05) is displayed to highlight the over and under densities of the mock

78

same positions in Fig. 3.11 and 3.12 show the same incompleteness irrespective of the mocks having different structures and number densities to 6dFGS.

While the spatial distribution of the mocks appear visually reasonable, the purpose of these mocks is to determine the optimal parameters for the FoF algorithm which is computed in the spatial domain. Therefore, we require a quantitative measure of the spatial distribution to ensure the mocks are reproducing the same spatial features as 6dFGS.

3.5.4 Projected clustering; the two-point correlation function

Measuring the correlation function is a well known method of statistically quantifying the spatial scales that separate galaxies (e.g. Palamara et al., 2013; Dolley et al., 2014). We utilise this and measure the correlation function of 6dFGS and the mocks as a quantitative comparison of the spatial distribution of galaxies. The probability (dP) of finding a pair of galaxies at separation r in volume element dV can be expressed as

$$dP = n[1 + \xi(r)] \, dV, \tag{3.11}$$

where n is the mean number density and $\xi(r)$ is the two-point correlation function (Peebles, 1980). Therefore, $\xi(r)$ is a measure of the excess probability of finding a galaxy pair at separation r within dV above a random (Poisson) distribution. To measure the correlation function for a set of galaxies, a corresponding random galaxy distribution is required. They are random in the spatial domain but are still required to adhere to the flux limits and incompleteness effects of the parent set of galaxies. Fig. 3.13 shows the spatial distribution of the random galaxies used to measure the 6dFGS clustering where there are no cosmological structures and the relevant areas of incompleteness have been reproduced. The random galaxy distribution for the SHAM and SAGE mock appear nearly identical to Fig. 3.13, though the number of galaxies in each random distribution are adjusted to contain the same number of galaxies in each respective mock. The lack of structure in the random galaxies leads to its redshift distribution taking a smooth form of the parent galaxy redshift distribution. The redshift distribution of 6dFGS, the SHAM and SAGE mock along

with their corresponding random galaxy redshift distribution can be seen in Fig. 3.14, 3.15 and 3.16.

While there are different correlation functions (e.g. real space, angular, projected), the most applicable correlation function for this work is one that utilises the positions and distances of the galaxies. 6dFGS galaxies have sky positions and redshifts where only a small subset have measured peculiar velocities. Measuring real space clustering with redshift determined distances would lead to an inaccurate correlation function (e.g. Coil et al., 2008) and the best choice for measuring galaxy clustering with redshift data is the projected correlation function.

Adopting the method of Fisher et al. (1994), each galaxy has position vector $\vec{v}$ with Cartesian co-ordinates $\vec{v} = (x, y, z)$. For two galaxies, the redshift separation vector is $\vec{s} = \vec{v_1} - \vec{v_2}$ and the mean distance is $\vec{l} = \frac{1}{2}(\vec{v_1} + \vec{v_2})$. The separation between a pair of galaxies in the parallel (π) and perpendicular (r_p) directions are measured as

$$\pi = \frac{\vec{s} \cdot \vec{l}}{|\vec{l}|}, \tag{3.12}$$

$$r_p = \sqrt{\vec{s} \cdot \vec{s} - \pi^2}. \tag{3.13}$$

The separations are binned up on a two-dimensional grid of r_p and π and the real space correlation function $\xi(r_p, \pi)$ is measured using the Landy & Szalay (1993) estimator

$$\xi(r_p, \pi) = \frac{DD - 2DR + RR}{RR}, \tag{3.14}$$

where DD, DR and RR are the binned counts for galaxy-galaxy, galaxy-random and random-random pairs. The projected correlation function $w_p(r_p)$ is measured as

$$w_p(r_p) = 2 \int_0^\infty \xi(r_p, \pi) \, d\pi, \tag{3.15}$$

which is an integration of the correlation function $\xi(r_p, \pi)$ along the parallel axis. As redshift-space distortions only affect the perpendicular component of the correlation function, $w_p(r_p)$ is independent of systematics from redshift measured distances.
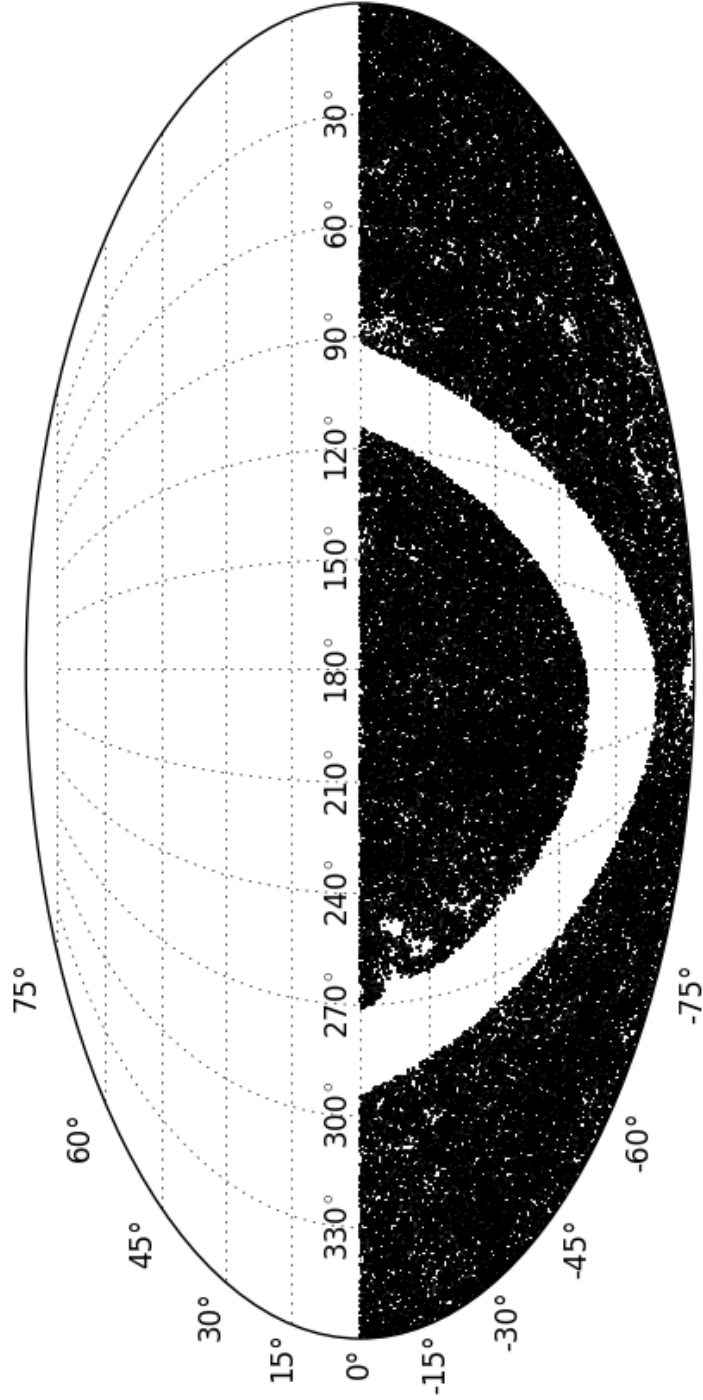
Fig. 3.13: A mollweide projection of the random distribution of galaxies produced to measure the 6dFGS clustering. The spatial distribution is random, which ensures that there are no cosmological structures present and the patchiness is a reproduction of the 6dFGS incompleteness. The random distribution of galaxies for the mocks looks analogous to this with each having the same number of randoms as the number of galaxies in their respective mock.
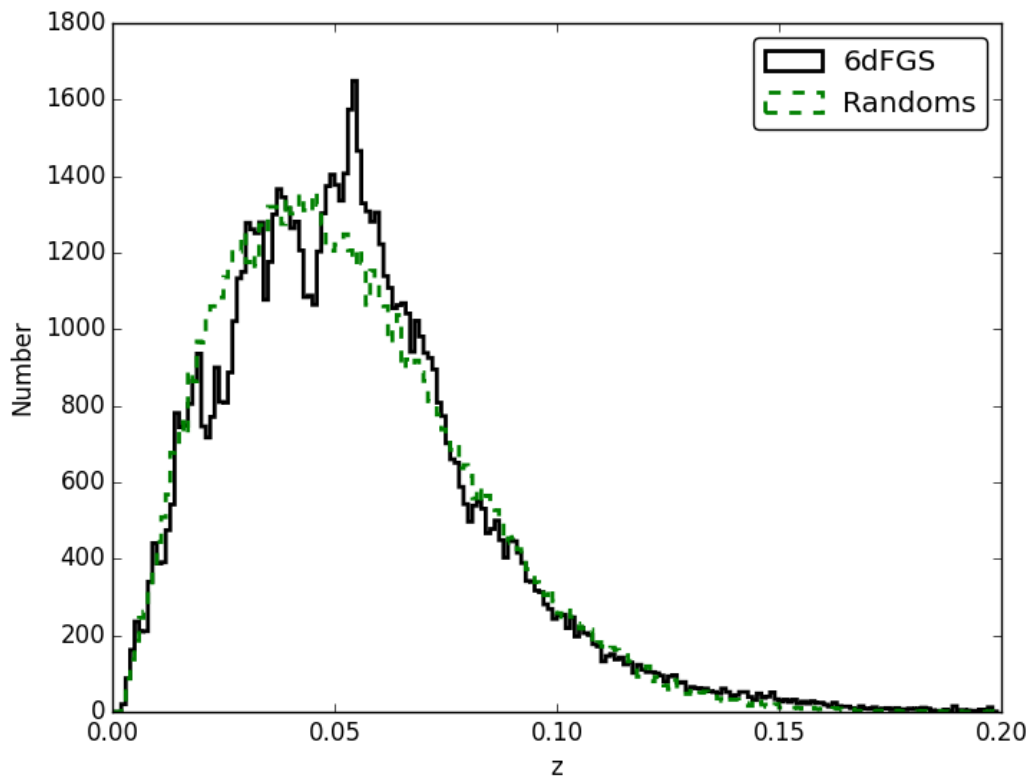
Fig. 3.14: The redshift distribution of 6dFGS (black solid) and the corresponding random galaxies (green dashed). The randoms produce a smoothed version of the 6dFGS redshift distribution.
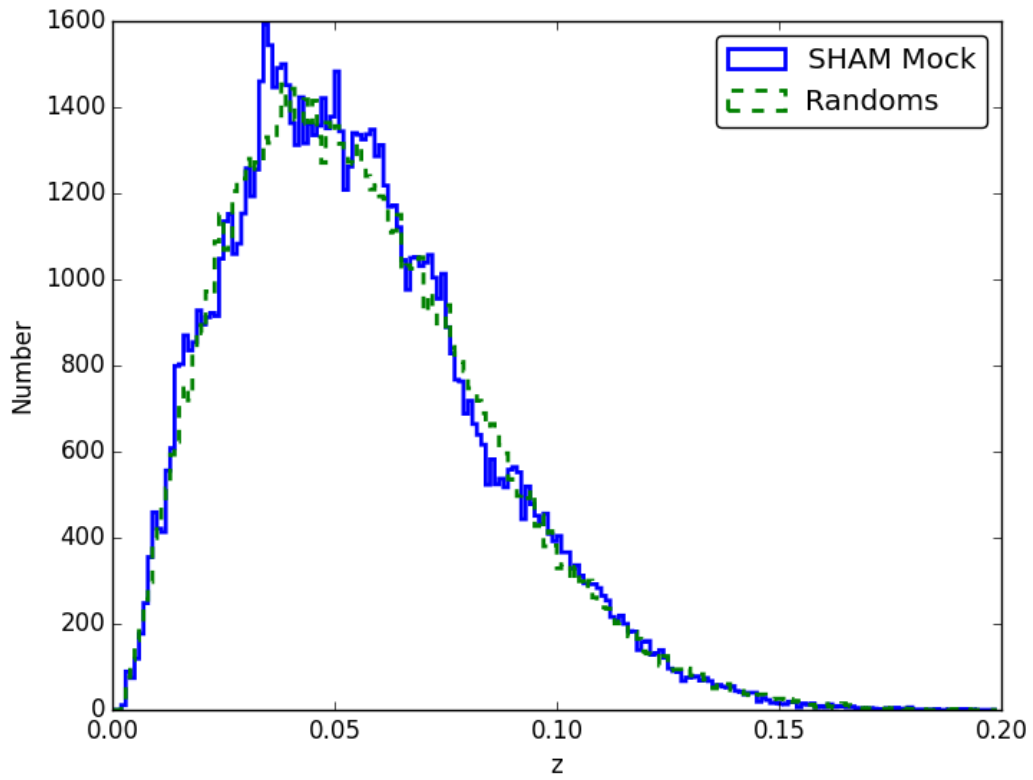
Fig. 3.15: The redshift distribution of the SHAM mock (blue solid) and the corresponding random galaxies (green dashed). The randoms produce a smoothed version of the SHAM mock redshift distribution.
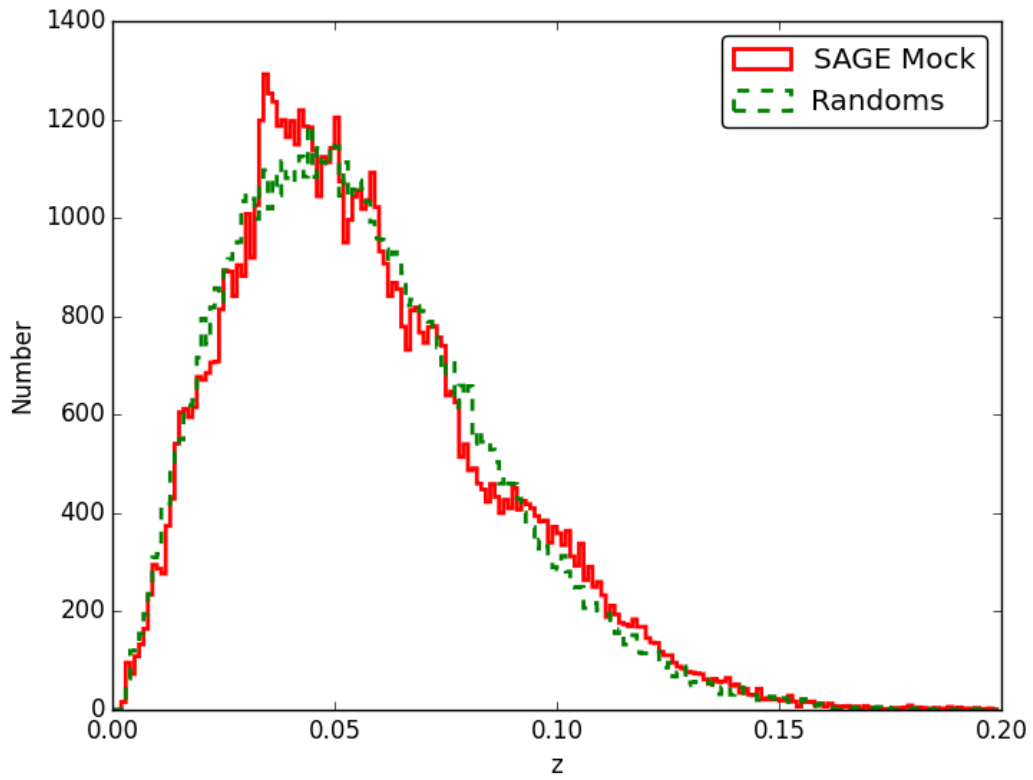
Fig. 3.16: The redshift distribution of the SAGE mock (red solid) and the corresponding random galaxies (green dashed). The randoms produce a smoothed version of the SAGE mock redshift distribution.

84

Fig. 3.17 shows the projected correlation function for 6dFGS, the SHAM and SAGE mock. The projected correlation function of the SHAM mock underestimate the clustering at all scales compared to 6dFGS and turns over at $r_p < 0.3$ Mpc h^{-1}. Clearly the spatial distribution of the SHAM mock is in poor agreement with the spatial distribution of 6dFGS and should not be used to calibrate the linking lengths of the FoF algorithm. The projected correlation function of the SAGE mock is in excellent agreement with 6dFGS down to $r_p = 0.3$ Mpc h^{-1}, where the projected correlation function turns over and the clustering is subsequently underestimated at small scales. The SAGE mock may be suitable to calibrate the linking lengths of the FoF algorithm and we discuss the details in Chapter 3.6.

3.6 Interpretation and future outlook

It is not clear why the projected correlation function of the SHAM mock has such poor agreement with 6dFGS. Weak clustering is a result of too many low mass galaxies (or halos) in the sample. It is possible that SHAM is placing faint galaxies in massive halos which would result in an underestimated correlation function. The cause of the underestimated projected correlation function should be investigated in the future as other SHAM correlation functions have been able to reproduce the same correlation function as observed galaxies (e.g. Conroy et al., 2006).

The projected correlation function of the SAGE mock is the same as 6dFGS for scales $r_p \geq 0.3$ Mpc h^{-1}. For projected distances less than 0.3 Mpc h^{-1}, the projected correlation function turns over and underestimates the clustering. In its current form, the SAGE mock may be suitable to calibrate the FoF linking lengths. However, the cause of the turn over at small scales needs to be understood to determine if this mock is suitable for linking length calibrations. We measured the clustering of the SAGE mock prior to any completeness corrections (chapter 3.4.4) and find the projected correlation function is within the 1σ uncertainty of the SAGE projected correlation function in Fig. 3.17. The turn over is still present at small scales and we conclude the completeness corrections are not the cause of underestimating the clustering. As the turn over is present in both the SHAM and SAGE mock, it may be inherent to the dark matter simulation used to create these mocks. A distance of 0.3 Mpc h^{-1} may be the limiting spatial resolution of the Millennium simulation. Therefore, the underestimated clustering may be a result of how the simulation handles galaxies below its resolution or how the simulation treats galaxy mergers.
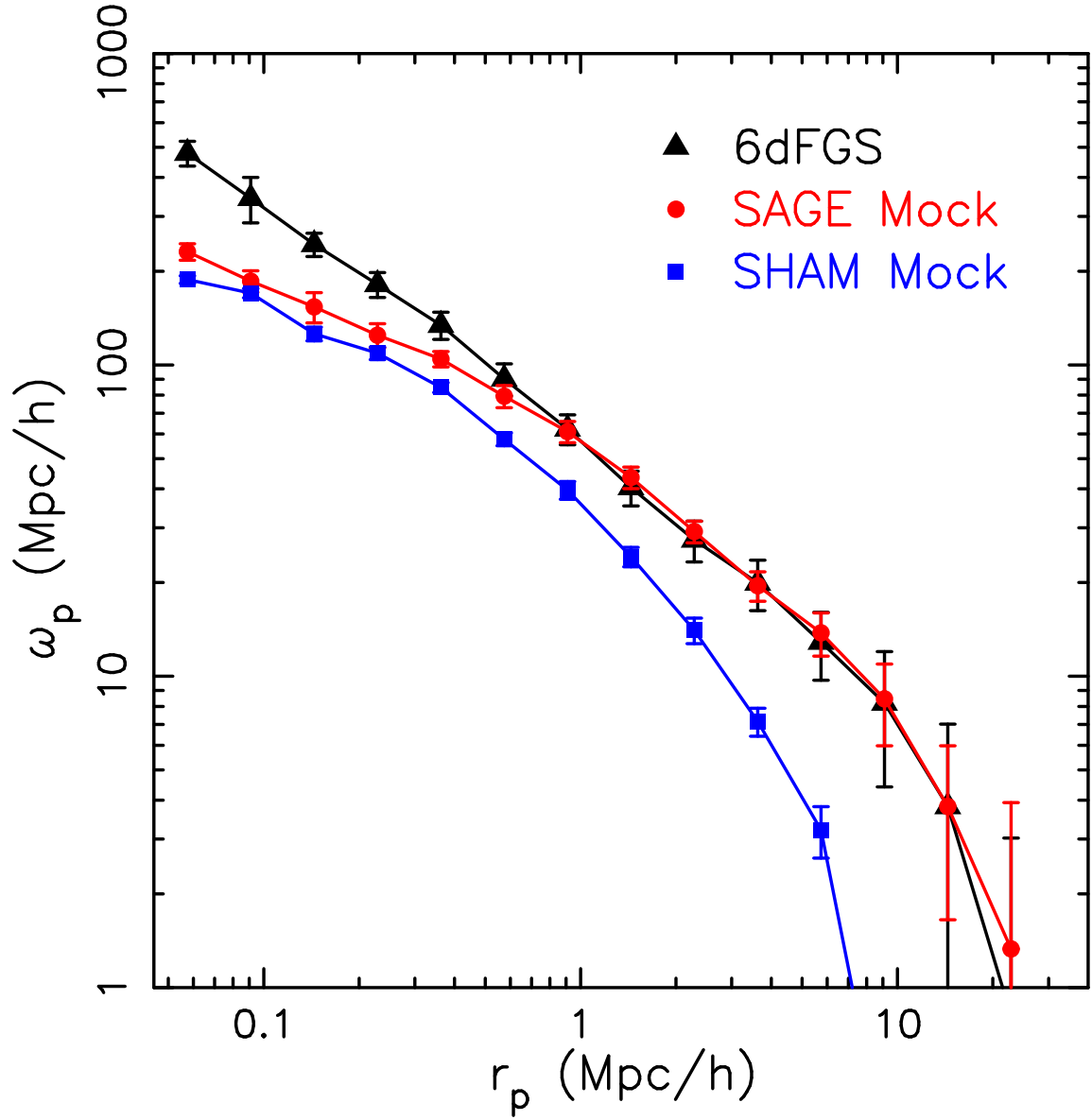
Fig. 3.17: The projected correlation functions for 6dFGS (black triangles), the SHAM (blue squares) and SAGE (red circles) mock where the uncertainties are measured using 10 equal area jackknife samples. The SHAM mock is in poor agreement with 6dFGS as its projected correlation function underestimates the clustering at all scales. The SAGE mock is in excellent agreement with 6dFGS. However, the projected correlation function of both mocks turn over and underestimate the clustering at $r_p < 0.3$ Mpc h^{-1}.

In the future, we will determine what distance is the limiting spatial resolution for the Millennium simulation. If spatial resolution is the issue, we will create a SAGE mock using the Bolshoi dark matter simulation which has better resolution than the Millennium dark matter simulation. If spatial resolution is not the issue, we need to determine the minimum (projected) distance we require the clustering to agree with 6dFGS. The initial aim of this project is to create a group catalogue of 6dFGS which would then lead to quantifying filaments using a second pass of the FoF algorithm (Murphy et al., 2011). With this aim in mind, the most important spatial aspect of the mock is to reproduce close galaxy groups analogous to those observed in 6dFGS. If the clustering agrees down the scale of close galaxy groups, the mock is suitable for calibrating the FoF linking lengths.

We will pursue all relevant avenues to understand what is causing the discrepancy of the projected correlation function at small scales. As we did not find a reliable mock to produce a group and filament catalogue, we have quantified the cosmic web in 6dFGS using a different method, which is explained in Chapter 4.

Monash University
Declaration for Thesis Chapter 4

Declaration by candidate:

I declare that my contribution to the work in Chapter 4 that is published in the Monthly Notices of the Royal Astronomical Society as Kleiner et al. (2017), involved the following:

The writing of the publication, the sample selection, analysis, and all other work contained therein (that is not referenced otherwise), excepting collection of the survey data and development of the data products that were used, such as: photometry, redshifts, spectroscopy etc.
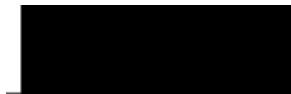
Extent of contribution by candidate: 85%

Co-author names: Kevin A. Pimbblet, D. Heath Jones, Bärbel S. Koribalski and Paolo Serra

Nature of co-author's contribution: The collection of the survey data, production of stellar mass estimates along with comments and feedback during writing of the paper. I have renumbered sections, equations and figures of the published paper in order to generate a consistent presentation within the thesis.

The undersigned hereby certify that the above declaration correctly reflects the nature and extent of the student's and co-authors' contributions to this work.

Candidate's signature:

Date: May 23, 2017

Main Supervisor's signature:

Date: May 23, 2017

CHAPTER 4

Evidence for HI replenishment in massive galaxies through gas accretion from the cosmic web

Dane Kleiner, Kevin A. Pimbblet, D. Heath Jones, Bärbel S. Koribalski, and Paolo Serra

Abstract

We examine the HI-to-stellar mass ratio (HI fraction) for galaxies near filament backbones within the nearby Universe (d < 181 Mpc). This work uses the 6 degree Field Galaxy Survey (6dFGS) and the Discrete Persistent Structures Extractor (DisPerSE) to define the filamentary structure of the local cosmic web. HI spectral stacking of HI Parkes All Sky Survey (HIPASS) observations yield the HI fraction for filament galaxies and a field control sample. The HI fraction is measured for different stellar masses and 5th nearest neighbour projected densities (Σ_5) to disentangle what influences cold gas in galaxies. For galaxies with stellar masses $\log(M_\star / M_\odot) \leq 11$ in projected densities $0 \leq \Sigma_5 < 3$ galaxies Mpc^{-2}, all HI fractions of galaxies near filaments are statistically indistinguishable from the control sample. Galaxies with stellar masses $\log(M_\star / M_\odot) > 11$ have a systematically higher HI fraction near filaments than the control sample. The greatest difference is 0.75 dex, which is 5.5σ difference at mean projected densities of 1.45 galaxies Mpc^{-2}. We suggest that this is evidence for massive galaxies accreting cold gas from the intra-filament medium which can replenish some HI gas. This supports cold mode accretion where filament galaxies with a large gravitational potential can draw gas from the large scale structure.

4.1 Introduction

The distribution of galaxies in the Universe forms a cosmic web (Bond et al., 1996) consisting of clusters, filaments and voids. Tightly packed groups and clusters are situated at web nodes and interconnected by a tenuous network of galaxy filaments delineating the underdense voids. These features were observed in early galaxy redshift surveys (e.g. CfA – Huchra et al., 1983; de Lapparent et al., 1986) and are clear in more recent galaxy redshift surveys such as the 2 degree Field Galaxy Redshift Survey (2dFGRS), the Sloan Digital Sky Survey (SDSS), the 6 degree Field Galaxy Survey (6dFGS), the Galaxy And Mass Assembly survey (GAMA) and the 2MASS Redshift Survey (2MRS) (Colless et al., 2001; Abazajian et al., 2009; Jones et al., 2009; Driver et al., 2011; Huchra et al., 2012). Dark matter N-body simulations and baryonic hydrodynamical simulations also reproduce these structures (e.g. Springel et al., 2006; Popping et al., 2009; Angulo et al., 2012; Habib et al., 2012; Poole et al., 2015).

Although filaments, clusters and voids have been studied separately for a long time, a unified approach to all these structures have only been possible in the past $\sim$ decade due to the availability of wide field redshift surveys. The cosmic web spans many orders of magnitude where the boundaries between the features of the web are not clearly defined. Finding a reliable method that quantifies galaxy membership of different regions is a difficult task and many attempts have been presented (e.g. Pimbblet, 2005; Stoica et al., 2005; Novikov et al., 2006; Hahn et al., 2007; Platen et al., 2007; Neyrinck, 2008; Forero-Romero et al., 2009; Stoica et al., 2010; Aragón-Calvo et al., 2010b,a; Sousbie, 2011; Sousbie et al., 2011; Smith et al., 2012; Leclercq et al., 2015). Currently, no single method has been universally adopted for such classification.

Furthermore, galaxy redshift survey data are often sparse and incomplete. Despite this, attempts to disentangle the cosmic web from these surveys are wide ranging (2dFGRS, SDSS, GAMA – Pimbblet et al., 2004; Murphy et al., 2011; Tempel et al., 2014b; Chen et al., 2015a; Alpaslan et al., 2014).

Forty per cent of the mass in the Universe resides within filaments (Aragón-Calvo et al., 2010c), which makes them an important aspect of galaxy evolution. While mass (e.g. Baldry et al., 2006; von der Linden et al., 2010; Evoli et al., 2011; Pimbblet & Jensen, 2012; Lemonias et al., 2013; Lin et al., 2016) and local galaxy density (e.g. Balogh et al., 2004; Kauffmann et al., 2004; Baldry et al., 2006; Poggianti et al.,

2006; Park et al., 2007; Bamford et al., 2009) are primary drivers of galaxy evolution, the total baryonic mass residing in filaments is too large to ignore. More broadly, filaments can be classified as intermediate density environments which (predominantly) host small groups of galaxies. Chen et al. (2015b) show that the properties of filament galaxies adhere to the morphology-density relation of Dressler (1980). The moderately dense filament environment makes them suitable sites for galaxy pre-processing, where galaxies may be significantly transformed before entering a cluster's virial radius. Pre-processing can strip the gas from a galaxy and quench its star formation (e.g. Lewis et al., 2002; Gómez et al., 2003; Porter et al., 2008; Haines et al., 2011; Mahajan, 2013) and filaments are ideal environments to search for signatures of galaxy pre-processing.

Previous attempts to determine if galaxies evolve differently in filaments are illuminating. A study by Porter et al. (2008) found a weak enhancement of star formation in the faint dwarf galaxies contained in filaments feeding a supercluster. Mahajan et al. (2012) show a similar result for the star formation rate of galaxies feeding clusters. However, Alpaslan et al. (2015) found that galaxy colour, morphology and stellar mass are driven by the stellar mass and local environment of galaxies and there was no observable influence that were driven by filaments. Later work by Alpaslan et al. (2016) found that the star formation of galaxies closer to the filament axis is slightly lower than those further away. This is consistent with Chen et al. (2015a) who showed red high-mass galaxies are typically closer to filaments than blue low-mass galaxies. Martínez et al. (2016) find galaxies in filaments have a lower specific star formation rate than galaxies in the field. Taken together, these studies suggest that galaxies in filaments evolve differently to galaxies in other large scale environments. However the evidence is tentative and more work is needed to confidently measure the potential second order influence of the large scale structure.

Numerical and hydrodynamic simulations show these filaments host a diffuse gaseous medium with a neutral hydrogen (Hi) column density of $\sim 10^{16}$ cm^{-2} at low redshift (e.g. Popping et al., 2009). Current radio telescopes observe column densities down to $\sim 10^{18}$ cm^{-2} which is not sensitive enough to detect the proposed Hi in filaments. Lyman-alpha emission from distant quasars can "illuminate" gas in the cosmic web which has constrained the mass and morphology of gas in the cosmic web (e.g. Cantalupo et al., 2014). However, these systems are rare and can not be used to study the cosmic web as a large statistical sample.

The interaction between galaxies and the gas reservoir in filaments is poorly constrained and where galaxies accrete their gas from is not well understood. A favourable scenario for gas accretion onto galaxies is 'cold mode' accretion where the gaseous medium of filaments provide galaxies with a reservoir of gas to draw from Kereš et al. (2005). Recently Aragon-Calvo et al. (2016) proposed the cosmic web detachment (CWD) model which links the properties of galaxies in a natural cosmological framework. In this model, galaxies attached to the cosmic web are able to accrete cold gas from filaments and form stars. Non-linear interactions detach galaxies from the cosmic web, sever its cold gas supply and quench star formation. The CWD model successfully reproduces important features of galaxy evolution (such as the red fraction dependence on mass and environment) in N-body simulations. However, observational evidence supporting this model is currently lacking.

Understanding the Hi content of galaxies is fundamental to understanding galaxy evolution. A sufficiently dense supply of Hi can condense in to massive molecular clouds that collapse and forms stars. Galaxies with an abundance of Hi have the ability to form new stars through this process and there are strong correlations between the Hi content of a galaxy and its star formation (Doyle & Drinkwater, 2006; Fabello et al., 2011a; Cortese et al., 2011; Catinella et al., 2013; Brown et al., 2015). Galaxies devoid of Hi gas do not have the fuel to form new stars and Hi -deficient galaxies are correlated with passive galaxies (e.g. Catinella et al., 2010; Dénes et al., 2014, 2016). Another important aspect is that Hi extends to larger radius than stars in galaxies. Therefore, it is more easily perturbed during tidal interactions, and can exhibit a disturbed morphology for a long period of time after these events (e.g. Koribalski & Dickey, 2004; Holwerda et al., 2011), making the Hi content of galaxies a powerful probe of their interaction with the environment.

The Hi Parkes all sky survey (HIPASS – Staveley-Smith et al., 1996; Barnes et al., 2001) detected Hi in 4315 galaxies in the Southern sky out to a redshift of $z < 0.0423$ (Meyer et al., 2004; Zwaan et al., 2004) down to a column density of 4.0×10^{18} cm^{-2}. HIPASS has played a significant part in understanding the role of Hi in galaxies (e.g. Meyer et al., 2004; Zwaan et al., 2004; Koribalski et al., 2004; Zwaan et al., 2005; Doyle et al., 2005; Wong et al., 2006; Meyer et al., 2008; Wong et al., 2009; Popping & Braun, 2011; Allison et al., 2014) but is limited to only the brightest Hi galaxies. Since the Hi 21-cm emission line is weak, observing Hi in galaxies with low column densities requires long integration times to reach the desired sensitivity which is often impractical. The Square Kilometre Array (SKA) and Australian Square Kilometre

Array Pathfinder (ASKAP) will be able to observe faint Hi galaxies with reasonable integration times. Survey such as the Widefield ASKAP L-band Legacy All-sky Blind surveY (WALLABY – Koribalski, 2012) and the Deep Investigation of Neutral Gas Origins (DINGO) will allow us to directly study the Hi in galaxies with unprecedented detail in larger volumes than any current survey. However WALLABY, DINGO and SKA surveys won't be available for years to come and we must rely on indirect methods of measuring Hi in galaxies.

In the interim, spectral stacking has proven to be a powerful technique for measuring Hi line strength. It measures the average Hi content of galaxies by co-adding spectra together (Lah et al., 2007, 2009; Pen et al., 2009; Fabello et al., 2011a,b, 2012; Geréb et al., 2013, 2015; Delhaize et al., 2013; Meyer et al., 2016). The advantage of spectral stacking is improved signal-to-noise over an individual spectrum, revealing signatures that can not be individually detected. As Hi in galaxies is sensitive to the dynamical history and immediate environment, the Hi mass of a galaxy can span orders of magnitude for a given stellar mass. The Hi -to-stellar mass ratio (Hi fraction) is a useful way of comparing how much Hi is present in galaxies with different stellar masses. There is a strong anti-correlation between Hi fraction and galaxy stellar mass while there is a weaker anti-correlation between Hi fraction and local galaxy density (e.g. Baldry et al., 2008; Catinella et al., 2010; Cortese et al., 2011; Brown et al., 2015). By contrasting the Hi fraction of galaxies in filaments with that of galaxies far from filaments (at fixed stellar mass and local galaxy density), we can directly compare the availability of Hi gas as a function large scale environment and test the CWD model.

In this paper, we select galaxies from the filament backbones of 6dFGS (Jones et al., 2009) and measure the average Hi fraction from HIPASS (Barnes et al., 2001) for different stellar masses and local galaxy densities. The 6dFGS is the most comprehensive galaxy redshift survey of the local Universe in the Southern hemisphere to date. There cosmic web is well-defined within $z < 0.1$ making it ideal for studying the large scale structure of the Universe and the galaxies that reside in it. This work can be used as a pilot study to define the cosmic web in the upcoming Taipan (da Cunha et al. in prep) survey and predict the amount of Hi present in galaxies within the cosmic web for ASKAP and the SKA.

Section 4.2 presents the optical data and Hi data. In section 4.3, we present our delineation of filaments in 6dFGS and the samples used in this study. Section 4.4 is where we show the stacking technique used to measure the average Hi fraction of our

samples. Section 4.5 presents the results for the average H I fraction our samples in different stellar mass and local density regimes. Section 4.6 discusses our measured H I fractions and its implication of galaxies evolving in the cosmic web. Finally, we summarise our conclusions in section 4.7. Throughout this paper, we assume the standard Λ cold dark matter cosmological model with $\Omega_M = 0.3$, $\Lambda = 0.7$ and $H_0 = 70.4$ km s^{-1} Mpc^{-1} (Komatsu et al., 2011).

4.2 Data

In this work, we utilise two primary datasets. The first is the 6 degree Field Galaxy Survey (6dFGS – Jones et al., 2004, 2009). We use the positions and redshifts of 6dFGS galaxies to determine the filamentary structure. From the 6dFGS catalogue, we use the SuperCOSMOS B–band photometry to test for unreliable H I spectra (section 4.4.1) and we use the 2MASS J–band photometry to estimate stellar masses in 6dFGS. The second dataset we use is the H I Parkes all sky survey (HIPASS – Staveley-Smith et al., 1996; Barnes et al., 2001). We extract the H I spectra from HIPASS data cubes using the optical positions and redshifts which are then stacked for different samples. In the following sections, we describe each dataset and how they relate to this work.

4.2.1 6dFGS optical catalogue

The 6dFGS is a galaxy redshift and peculiar velocity survey conducted in the southern hemisphere for $|b| > 10°$ (Jones et al., 2004, 2009). It contains 125 071 galaxy redshifts obtained with the 6 degree field fibre-fed multi-object spectrograph at the United Kingdom Schmidt Telescope at Siding Spring. The survey is near-complete at $(K, H, J, r_F, b_J) \leq (12.65, 12.95, 13.75, 15.60, 16.75)$. The primary targets for 6dFGS are K-band selected and secondary targets are selected from J, H b_J and r_F bands. The J, H and K band photometry is taken from the 2MASS extended source catalogue (Jarrett et al., 2000) and the b_J and r_F photometry comes from the SuperCOSMOS catalogue (Hambly et al., 2001b,a). The 6dFGS volume is comparable to 2dFGRS (Colless et al., 2001), but a consequence of the huge sky coverage of 6dFGS is that it has a bright flux limit and therefore a relatively shallow survey depth compared to the other surveys.

Each 6dFGS redshift is assigned a quality (Q) reflecting its reliability. The redshifts blunder rate for individual and pairs of 6dFGS galaxies is 1.2% and 2.3% respectively. Redshift blunders are defined as a mismatch of more than 330 km s^{-1} (5σ) between a pair of redshift measurements of the same target. We refer the reader to (Jones et al., 2004, 2009) for further technical details.

For this analysis, we limit the 6dFGS input sample to redshift-space positions within the HIPASS volume ($z < 0.0423$). Only galaxies with Q = 3 (reliable) or 4 (high quality) have been used to define our cosmic structures and extract HI spectra for subsequent stacking. As the HIPASS volume is less than the median redshift of 6dFGS ($z_{\frac{1}{2}} = 0.053$), all galaxies within the 6dFGS catalogues are used irrespective of the subsample to which they belong.

Stellar mass estimates are those used in Beutler et al. (2013) which have been applied to our cosmology (H$_0$ = 70.4 km s^{-1} Mpc^{-1}). The 6dFGS J–band magnitudes we use offer the lowest background noise making it the most reliable for stellar mess estimates and have been used in the calculations. Stellar population synthesis results from Bruzual & Charlot (1993) were used in conjunction with the modified Salpeter initial mass function (Bell & de Jong, 2001) to estimate the stellar masses. The typical uncertainty for the stellar mass estimates within this volume are log(M$_\star$ / M$_\odot$) $\pm$ 0.04.

4.2.2 HIPASS radio data

HIPASS is a blind HI survey that covers the whole southern sky (Barnes et al., 2001) and northern sky to $\delta \leq +25°$ (Wong et al., 2006). The observations were carried out with the Australian Telescope National Facility's Parkes 64 m telescope using the 21 cm multibeam receiver (Staveley-Smith et al., 1996). The observed frequency range is 1362.5 – 1426.5 MHz corresponding to a velocities -1 280 < cz < 12 700 km s^{-1}. The data are organised into $8° \times 8°$ cubes with a gridded beam of ~15.5 arcmin and 18 km s^{-1} velocity resolution. Like other surveys that observe a large area of sky, it has a shallow survey depth ($z < 0.0423$) with a rms of 13.3 mJy per 13 km s^{-1} channel. These limitations result in only the brightest HI galaxies being detected in HIPASS. As we are utilising a spectral stacking technique in our analysis, it is not of concern if an individual galaxy has been detected above the noise.

For this study, we use HIPASS data cubes to extract HI spectra to conduct our stacking analysis. The positions and redshifts of 6dFGS galaxies are used to define

the central co-ordinates in the HIPASS data cubes which we extract individual H I spectra for galaxies of different samples. The spectra are stacked and we measure the H I fraction for each sample.

4.3 Delineating filaments from redshift data

To define filaments of galaxies in redshift data, one must devise a method of connecting a series of points that have a higher density than a random distribution and determine if the result is a good representation of the large scale structure in the Universe. This is inherently difficult as the length of filaments span many orders of magnitude with complex geometry and poorly defined boundaries. Redshift data presents additional challenges as the data can be sparse, incomplete and redshift space distortions elongate clusters in the z-direction, causing them to appear filamentary when they should not be classified as filaments.

4.3.1 Choice of algorithm

Numerous techniques have been developed in an attempt to over come the difficulties of reliability delineating filaments in galaxy surveys. These techniques are separated by a set of assumptions based on the physical, probabilistic and geometric treatment of filaments.

Two physically motivated filament finders are the two-pass friends of friends algorithm and minimal spanning tree used by Murphy et al. (2011) and Alpaslan et al. (2014). Both approaches operate on a group catalogue where redshift space distortions are suppressed. This is advantageous by ensuring clusters stretched in the z-direction do not get classified as filaments. A limitation of this approach is that mock catalogues that match the survey characteristics (i.e. selection function and completeness) are required to calibrate the parameters that link galaxies in groups and groups to filaments. The linking parameters for extracting filaments in this technique is arbitrary in the sense that it is visually determined by what looks the best.

The probabilistic approach for delineating filaments uses galaxy positions to determine the likelihood of being a part of a long, thin structure (i.e. a filament) in random

data. Tempel et al. (2014b) use the Bisous model, an object point process with interactions that assume galaxies are grouped inside small cylinders and connected aligned cylinders form filaments. Leclercq et al. (2015) use decision theory, a method that classifies cosmic web components by deciding which component maximises its quantitative profit for each galaxy position. Filaments have a unique structural type component in decision theory and galaxy positions optimised by this component are chosen to be part of the filament. These techniques are a natural integration of probability theory which allow the classification of filaments directly from the galaxy positions without a group catalogue or density field. However, redshift space distortions are not suppressed and the success of these techniques rely on how well the priors match the underlying cosmic web. Essentially, the agreement between what constitutes a filament (i.e. galaxies in cylinders or a unique structural component) and what a filament is. Currently, the optimal choice for modelling filaments is an open mathematical and data analysis problem.

A popular technique for extracting filaments use a geometric approach. Broadly speaking, a density field or equivalent (such as a tessellation) is created from galaxy positions and a mathematical formalisation is computed over the field to compute the geometry and extract filaments. For example, the watershed technique transforms the density field in to a series of valleys and ridges and filaments are viewed as ridges surrounded by multiple valleys (Platen et al., 2007; Aragón-Calvo et al., 2010a), the Hessian matrix computed from a density field identifies filaments as a specific set of eigenvalues (Hahn et al., 2007; Cautun et al., 2013), the subspace constrained mean shift algorithm identifies filaments as ridges above a critical density (Chen et al., 2015a) and connected saddle points in Morse theory is used to delineate filaments from the Delaunay tessellation (Sousbie, 2011). While filaments are viewed and extracted differently in each formalism, every technique using the geometric approach requires a measure of density and filaments are identified as thin ridges. The advantage of the geometric approach is that it does not make any assumptions about the underlying dark matter distribution of the Universe. The success of each technique rely on how well the mathematical formalism identify and separate the components of the cosmic web in data with varying densities. Even though there is no physical basis for the cosmic web to be described by the formalisms, all these techniques have shown excellent agreement with identifying filaments (and other cosmic web components).

The geometric approaches (such as Aragón-Calvo et al., 2010a; Cautun et al., 2013; Sousbie, 2011) have produced excellent filament delineation in N-body simulations.

When searching for filaments in redshift data, incorrect distances measured from redshifts make it considerably harder to trace the coherent three-dimensional structure of filaments. This is a serious concern in the local Universe where peculiar velocities dominate redshift measurements of galaxies. Chen et al. (2015b) splits the galaxy positions in to thin redshift slices, removing the redshift dependance of filaments. While the three-dimensional coherence of filaments is lost, the galaxy number density in each slice is sufficient to easily observe the large scale structure of filaments at that distance. Hence, the contamination from peculiar velocity dominated redshifts is minimised.

Given the above considerations, we have decided to identify filaments in 6dFGS using the Discrete Persistent Structures Extractor[1] (DisPerSE – Sousbie, 2011; Sousbie et al., 2011). DisPerSE is freely available, easy to use and utilises a geometric approach to identify coherent multi-scale astrophysical structures such as voids, walls, filaments and clusters. While there are multiple geometric approaches that can be used to identify filaments, DisPerSE has the distinct advantage of operating directly on a tessellation opposed to a smoothed density field where structural information can be lost (e.g. Watershed, Hessian matrix, subspace constrained mean shift algorithm). Additionally, DisPerSE is scale and parameter-free unlike other geometric approaches that require smoothing lengths. DisPerSE can be applied to both N-body simulations and galaxy redshift surveys without the use of complex mocks and Sousbie et al. (2011) show excellent recovery of the cosmic web in both simulation and redshift surveys, even when the data is sparse and incomplete.

4.3.2 Filament backbones in 6dFGS

We summarise the main steps below and refer the reader to Sousbie (2011) for the theory and implementation of DisPerSE, Sousbie et al. (2011) for the application of DisPerSE on astronomical data and Appendix B of Sousbie et al. (2011) for a succinct summary of the algorithm.

We adopt a similar method to Chen et al. (2015b) and split 6dFGS in to thin redshift slices ($\delta z = 0.005$) to run DisPerSE on two-dimensional data. While DisPerSE can be applied to three-dimensional data, we found poor agreement between the cosmic web and the filamentary skeleton returned by DisPerSE. See appendix 4.9 for a comparison and discussion on the application of DisPerSE in two and three dimensions.

---

[1]http://www2.iap.fr/users/sousbie/web/html/indexd41d.html

Table 4.1: The best persistence ratio (σ_{pr}) for the galaxy distributions above ($b > 10°$) and below ($b < $ -10°) the Galactic Plane in each 6dFGS redshift slice. The persistence ratios were chosen to return the most *topologically robust* filament backbones.

Redshift Range	σ_{pr} for $b > 10°$	σ_{pr} for $b < $ -10°
$0.0025 \leq$ z < 0.0075	3.8	4.0
$0.0075 \leq$ z < 0.0125	3.2	3.8
$0.0125 \leq$ z < 0.0175	4.0	4.4
$0.0175 \leq$ z < 0.0225	3.6	4.2
$0.0225 \leq$ z < 0.0275	4.0	3.8
$0.0275 \leq$ z < 0.0325	3.6	4.6
$0.0325 \leq$ z < 0.0375	4.0	4.4
$0.0375 \leq$ z < 0.0425	4.0	4.8

DisPerSE operates directly on the galaxy positions and we separate each slice into distinct samples above and below the Galactic Plane ($|b| > 10°$) to ensure no spurious connections are made over this boundary. A density field is produced from the galaxy positions using the Delaunay tessellation. Discrete Morse theory (Forman, 1998, 2002) is then applied on the tessellation which computes the geometry and topology of the density field, enabling the filament backbones to be recovered. Fig. 4.1 shows this procedure on two slices used in this analysis and the full sample can be viewed in Appendix 4.8.

While DisPerSE is scale and parameter-free, the user is required to select a threshold (persistence ratio – σ_{pr}) to extract the significant and robust topological features above the sampling noise. The persistence ratio is a signal-to-noise measurement of how sensitive a topological feature (such as a filament) is to change. Features with high persistence ratios have greater topological significance above the sampling noise. Choosing a persistence ratio that eliminates spurious detections while retaining only the most prominent features of the cosmic web is the aim. The persistence ratio will differ according to the distribution and density of the data. To find the optimal persistence ratio for each slice, we inspected the filament backbones returned by DisPerSE using initial persistence ratios between $2\sigma_{pr}$ and $5\sigma_{pr}$. Table 4.1 shows the redshift ranges for each 6dFGS slice and the persistence ratio chosen for each side of the Galactic Plane. Our requirement to separate local and large scale environmental effects lead us to choose conservative persistence ratios. This will return the most *topologically robust* filament backbones, by which we mean as those unambiguously above the noise.
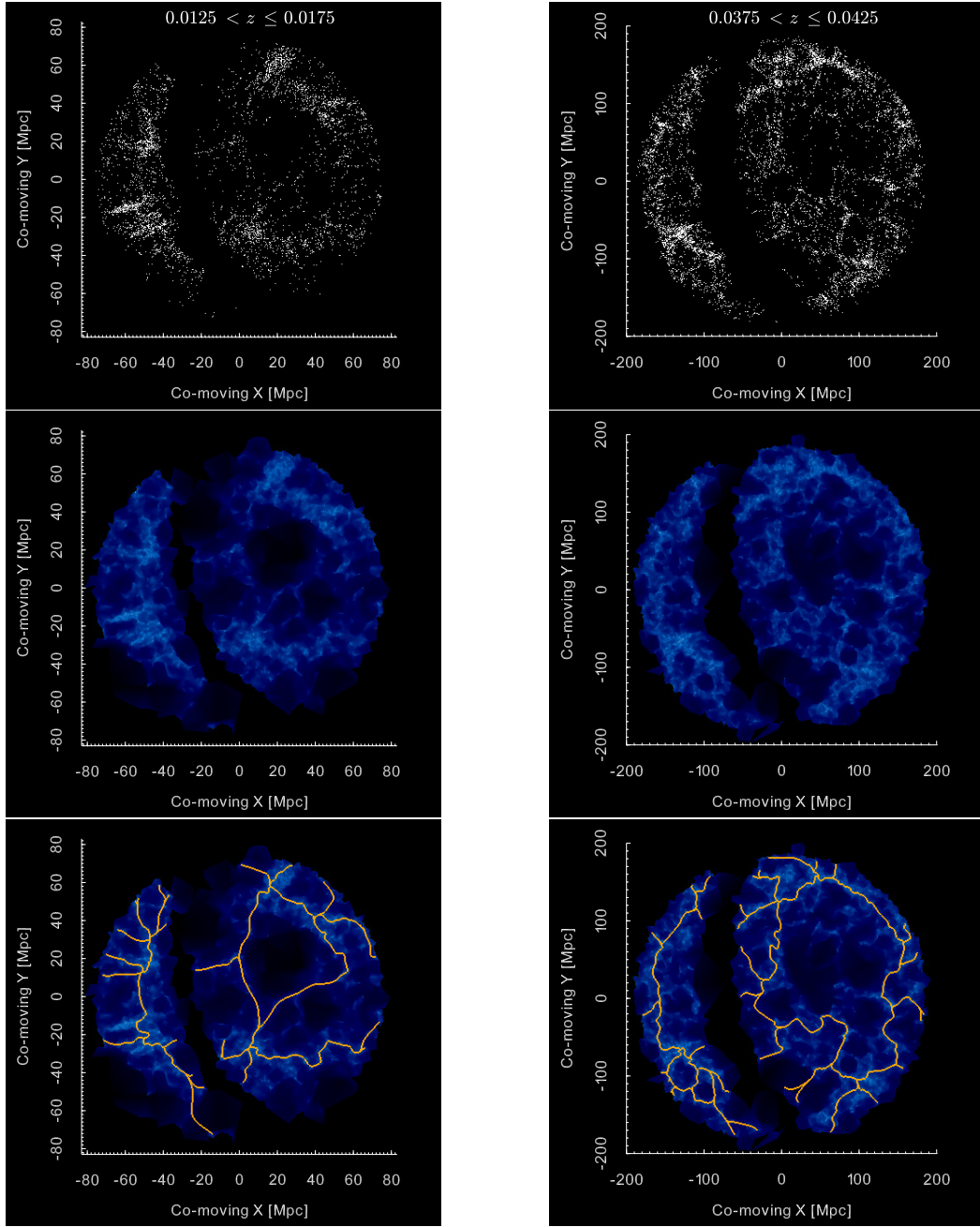
Fig. 4.1: The main steps of DisPerSE delineating filament backbones from a galaxy distribution. The left column is the redshift slice $0.0125 \leq z < 0.0175$ and the right column is the redshift slice $0.0375 \leq z < 0.0425$. The top panel shows all 6dFGS galaxies for the respective redshift ranges and the middle panel shows the corresponding Delaunay tessellations. The tessellation is coloured according to the local density field where underdense regions are darker colours and overdensities are lighter colours. The bottom panel has the filament backbones (orange lines) found by DisPerSE overlaid on the tessellation. There is excellent agreement between the density of the tessellation and the galaxy distribution and excellent agreement between the thin overdensities in the tessellation and the filament backbones found by DisPerSE. This process for all the redshift slices can be viewed in Appendix 4.8.

The main caveat of DisPerSE is that Morse theory requires filaments to circumscribe voids. This can sometimes lead to a filament being defined in a region that is underdense and most likely incomplete. By choosing a persistence ratio that returns the most topologically significant filament backbones, we minimise the occurrence of filament backbones being defined in unrealistic underdense regions. When we assign galaxies to the relevant sample of interest (section 4.3.3), on the order of ~10 galaxies from incomplete regions are assigned to a sample that contains ~5 000 galaxies and does not affect our results.

4.3.3 Sample Selection

We create two samples:

1. The *near filament* sample containing 5 358 galaxies with available stellar mass estimates, limited to 0.7 Mpc from filament backbones with a projected density of $\Sigma_5 < 3$ galaxies Mpc^{-2}.

2. A *control sample* containing 8 149 galaxies with available stellar mass estimates, a minimum distance of 5 Mpc from the nearest filament backbone and projected density of $\Sigma_5 < 3$ galaxies Mpc^{-2}.

The purpose of these two samples is to differentiate galaxies on the basis of surrounding large scale structure and an example is shown in Fig. 4.2. A maximum distance of 0.7 Mpc was chosen for the near filament sample as this is considered a thin radius for filaments of galaxies (Tempel et al., 2014b). The minimum distance of 5 Mpc from the nearest filament backbone in the control sample implements a clear buffer between the two samples which eliminates potential in-falling galaxies in the control sample. There are 36 805 6dFGS galaxies in the HIPASS volume where 8 436 and 12 119 are in the near filament and control sample prior to any density or stellar mass restriction.

In each redshift slice we obtain a measure of local galaxy density using the 5$^{\text{th}}$ nearest neighbour projected density (e.g. Balogh et al., 2004; Brough et al., 2013), defined as

$$\Sigma_5 = \frac{5}{\pi r_5^2},\tag{4.1}$$
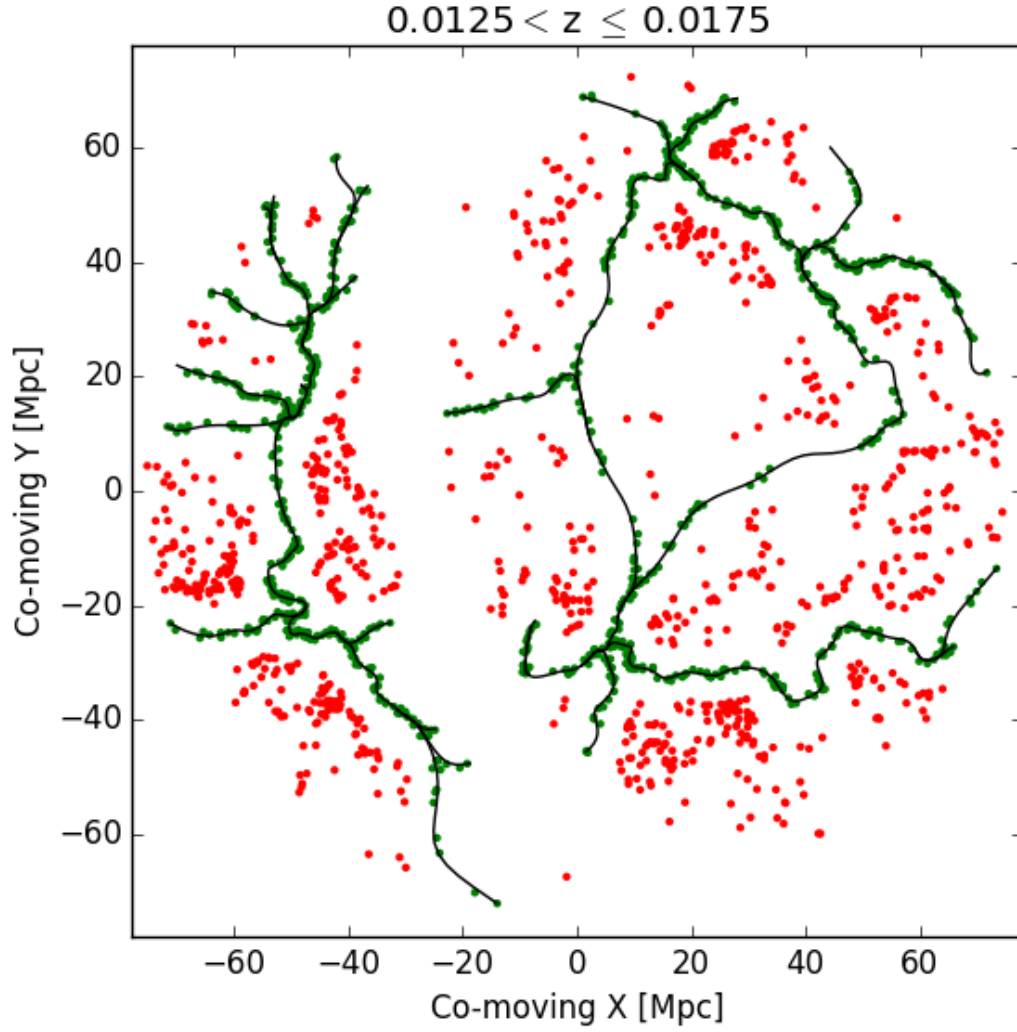
Fig. 4.2: Redshift slice $0.0125 \leq z < 0.0175$ showing filament backbones (solid black lines), galaxies near filaments (green points) and the control sample (red points).

Table 4.2: Projected density (Σ_5), in units of galaxies Mpc^{-2} for all galaxies in the HIPASS volume, the near filament and control sample. All samples have been restricted to $\Sigma_5 < 3$ galaxies Mpc^{-2} and the projected density distribution of the near filament sample is distinctly different from the control sample.

Sample	Ngal	Mean	Median	Standard Deviation
All Galaxies	36 805	0.57	0.36	0.59
Near Filament	7 510	0.90	0.58	0.71
Control	11 982	0.30	0.16	0.39

where r_5 is the projected distance in Mpc to the 5th nearest galaxy from the target galaxy. We restrict both samples to have a maximum projected density of 3 galaxies Mpc^{-2}. This density threshold reduces the near filament and control sample to 7 510 and 11 982 galaxies and removes galaxies residing in overdense environments which are subjected to cluster mechanisms.

Fig. 4.3 shows the distribution of Σ_5 for all galaxies within the HIPASS volume, the near filament sample and the control sample. It is clear that near filament sample has a different Σ_5 distribution compared to the control sample. The distribution of Σ_5 for the near filament systematically consists of denser local environments which reflects that filaments can be viewed as intermediately dense environments that mainly host groups of galaxies. The distribution of Σ_5 for the control sample is dominated by the lowest density local environments which shows that we have obtained a good representation of field galaxies far from filament backbones. Table 4.2 highlights the differences between the distributions of Σ_5 for the two samples used in this work.

Stellar masses are estimated using J–band photometry (Beutler et al., 2013) and the photometry of a galaxy is dependant on its input catalogue. As 6dFGS utilised multiple input catalogues, not all galaxies have J–band photometry and these galaxies have no stellar mass estimate. This reduces the number of galaxies in the near filament and control sample and our final samples contain 5 358 and 8 149 galaxies. Fig. 4.4 shows the distribution of the stellar masses for all 6dFGS galaxies within the HIPASS volume, the near filament and control sample. The stellar mass distributions of the near filament and control sample show remarkable similarities. Table 4.3 quantifies the properties of the distributions.

The indistinguishable stellar mass distributions and maximum projected density threshold of the near filament and control sample ensure that we are comparing galaxies of the same stellar mass in similar local environments.
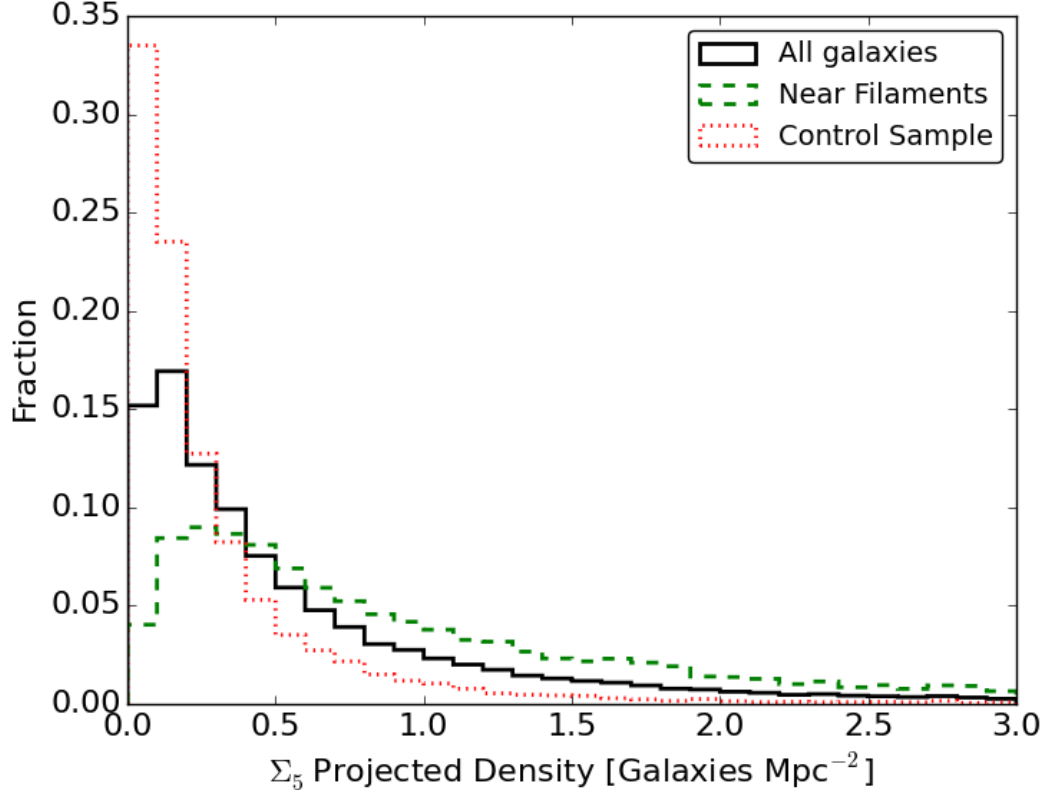
Fig. 4.3: Normalised distribution of projected density for all 6dFGS galaxies in the HIPASS volume (solid black), galaxies near filament (dashed green) and the control sample (dotted red). The near filament sample systematically contains higher density local environments than the control sample, which is dominated by the lowest density local environments.

Table 4.3: Stellar mass distributions in units of $\log(M_\odot)$ for all 6dFGS galaxies in the HIPASS volume, the final near filament and control sample. The near filament and control sample distributions have very similar properties to each other.

Sample	Ngal	Mean	Median	Standard Deviation
All Galaxies	26 855	10.52	10.56	0.45
Near Filament	5 358	10.53	10.58	0.46
Control	8 149	10.57	10.58	0.39
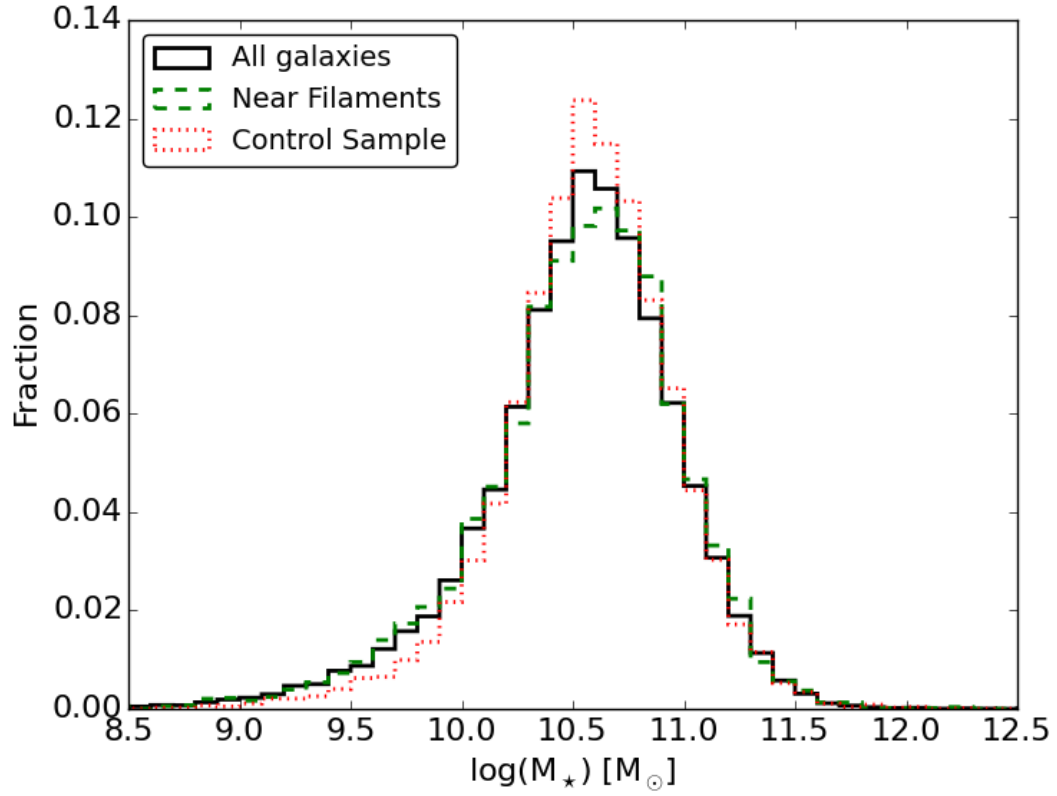
Fig. 4.4: Normalised stellar mass distributions for all 6dFGS galaxies in the HIPASS volume (solid black), galaxies near filament (dashed green) and the control sample (dotted red). The near filament sample and control sample have similar stellar mass distributions.

4.4 HɪI Spectral stacking

We perform spectral stacking in the same manner as Delhaize et al. (2013) with two differences; (i) we stack in velocity space (described below), and (ii) we exclude certain galaxies that meet our criteria for unreliable spectra (section 4.4.1).

We use 6dFGS positions and velocities to extract the flux spectra from the HIPASS cubes for each galaxy to be stacked. In each HɪI flux spectrum, a 4th-order polynomial (excluding the emission region) is subtracted from the baselines to account for noise due to standing waves internally reflected off telescope structures, or data reduction artefacts. All flux spectra are converted to a HɪI mass per unit velocity through

$$\frac{M_{\mathrm{HI}}}{\Delta v} = \frac{2.356 \times 10^5}{(1+z)} \frac{S}{\Delta v} D_L^2, \tag{4.2}$$

where $\frac{S}{\Delta v}$ is the flux per unit velocity (in Jansky km s^{-1}) and D$_L$ is the luminosity distance (in Mpc). We need to convert spectra into the HɪI domain prior to co-adding to use the HɪI luminosity rather than flux. Each HɪI spectrum is shifted to its respective rest frame which aligns all spectra to the same point of reference. The co-added weighted HɪI mass per unit velocity of the sample is found as

$$\left\langle \frac{M_{\mathrm{HI}}}{\Delta v} \right\rangle = \frac{\sum_{i=1}^{N}\left(w_i \frac{M_{\mathrm{HI},i}}{\Delta v}\right)}{\sum_{i=1}^{N} w_i}, \tag{4.3}$$

where $\frac{M_{\mathrm{HI},i}}{\Delta v}$ is the HɪI mass per unit velocity of the ith galaxy and w_i is the associated weight. We calculate the weight of the ith galaxy as

$$w_i = (\sigma_i D_{L,i}^2)^{-2}, \tag{4.4}$$

where σ_i is the rms of the flux spectrum excluding the emission region of the galaxy and D$_{L,i}$ is the luminosity distance. This choice in weight ensures spectra with a high rms and non-detections of distant galaxies do not overpower any HɪI emission in the stack. The average HɪI mass of a sample of galaxies (equation 4.5) is measured by integrating over the velocity interval where emission is present $[v_1, v_2]$ in the co-added weighted HɪI mass per unit velocity $\left\langle \frac{M_{\mathrm{HI}}}{\Delta v} \right\rangle$,

$$M_{\mathrm{HI}} = \int_{v_1}^{v_2} \left\langle \frac{M_{\mathrm{HI}}}{\Delta v} \right\rangle \, dv. \tag{4.5}$$

106

The corresponding H I fraction (f_{HI}) is

$$f_{\mathrm{HI}} = \log_{10}\left(\frac{M_{\mathrm{HI}}}{M_\star}\right), \qquad (4.6)$$

where M_{HI} is the H I mass (in solar masses) measured from the stacking process and $M_\star$ is average stellar mass (in solar masses) of the sample. By measuring the H I fraction, we are able to compare the H I content of galaxies for different stellar masses.

The dominant uncertainty in the H I fraction is the uncertainty in the average H I mass. To measure the uncertainty in the average H I mass for a sample of N galaxies, we stack N 'random' flux spectra. Each random flux spectrum is extracted using a random sky position and velocity ($2\,000 \leq \mathrm{v}_{random} \leq 11\,500$ km s^{-1}), chosen to avoid Galactic emission and the edges of each HIPASS cube. Random flux spectra are stacked in the same way as actual co-added weighted H I data.

The velocity range (v_1 and v_2) used in equation 4.5 is set by the boundaries of the stacked profile that cross the rms of the random stack for the first time. The rms of the randoms is integrated between v_1 and v_2 to measure the 1σ uncertainty in the stack.

If the average H I mass 3 standard deviations above the uncertainty, it is considered a clear detection. Otherwise, there is no clear detection and the 1σ upper limit is measured by integrating the rms of the randoms $\pm$ 150 km s^{-1}, a typical rotation velocity for galaxies in a H I stacked sample (Delhaize et al., 2013).

4.4.1 Accounting for spectra with H I flux of indeterminable origin

The full width half maximum of the gridded HIPASS beam is $\sim$15.5 arcmin which can have multiple galaxies contributing H I flux to a single spectrum (e.g. see Doyle et al., 2005; Rohde et al., 2006). The spectra with H I flux of indeterminable origin above the HIPASS noise are considered *unreliable* which we exclude by constructing a simple mock H I profile and determining if it would be observed in HIPASS.

Taking the HIPASS beam to be Gaussian, a rectangular mock H I profile is constructed for any 6dFGS galaxy (except the central galaxy) within 3 standard deviations (19.8 arcmin) from the beam centre, a recessional velocity within $\pm$ 300 km s^{-1} of the central galaxy and has a (b_{j} - r_{F}) colour < 1.3. We have chosen the velocity overlap

to be 300 km s^{-1} because 600 km s^{-1} is the maximum profile width of the HICAT galaxies Doyle et al. (2005) and in the simulations of Obreschkow et al. (2013). (b_j - r_F) = 1.3 is the reddest colour of 6dFGS galaxies with HIPASS detections and we choose the same value as our upper limit to include HI rich galaxies likely to contribute flux in HIPASS spectra.

The width of the mock profile is predicted using the Tully-Fisher relation measured from HIPASS galaxies with known optical counterparts (c.f. Delhaize et al., 2013). The B–band scaling relation of Dénes et al. (2014) used to predict the HI mass of a galaxy has the least scatter in the literature, which we use to estimate the integrated HI mass for the mock HI profile. The width of the HI profile and the integrated HI mass of the galaxy (area of the profile) enables us to determine the peak flux (amplitude of the profile) for the mock HI profile. We convolve each mock HI profile with a Gaussian weight in accordance with its angular distance from the assumed Gaussian beam centre.

A spectrum is considered unreliable and excluded from the stack if the peak flux of the mock HI profile is greater than 3 standard deviations of the rms and less than the peak flux of its HIPASS spectrum. Fig. 4.5 shows an example of a unreliable spectrum that has been excluded from the stack, in this way.

Fig. 4.6 shows the stacked spectrum with the greatest difference between including all spectra and excluding unreliable spectra. 8 out of a total of 619 spectra were removed from the stack and resulted in a ∼20% decrease of HI flux. A decrease of HI flux is expected as neighbouring HI rich galaxies contribute additional flux to the stack. While unreliable spectra can make a significant difference (Fig. 4.6), it does not dominate the HI flux of the stack. The majority of 6dFGS galaxies are not detected above the HIPASS noise as unreliable spectra typically make up a few percent of any sample and the flux from neighbouring galaxies offset from the beam centre quickly decrease due to the Gaussian beam response.

4.5 Results: HI fraction for varying stellar mass and projected densities

We present the HI fraction (HI-to-stellar mass ratio) of galaxies for varying stellar masses and projected densities in the near filaments and control sample. Both stellar
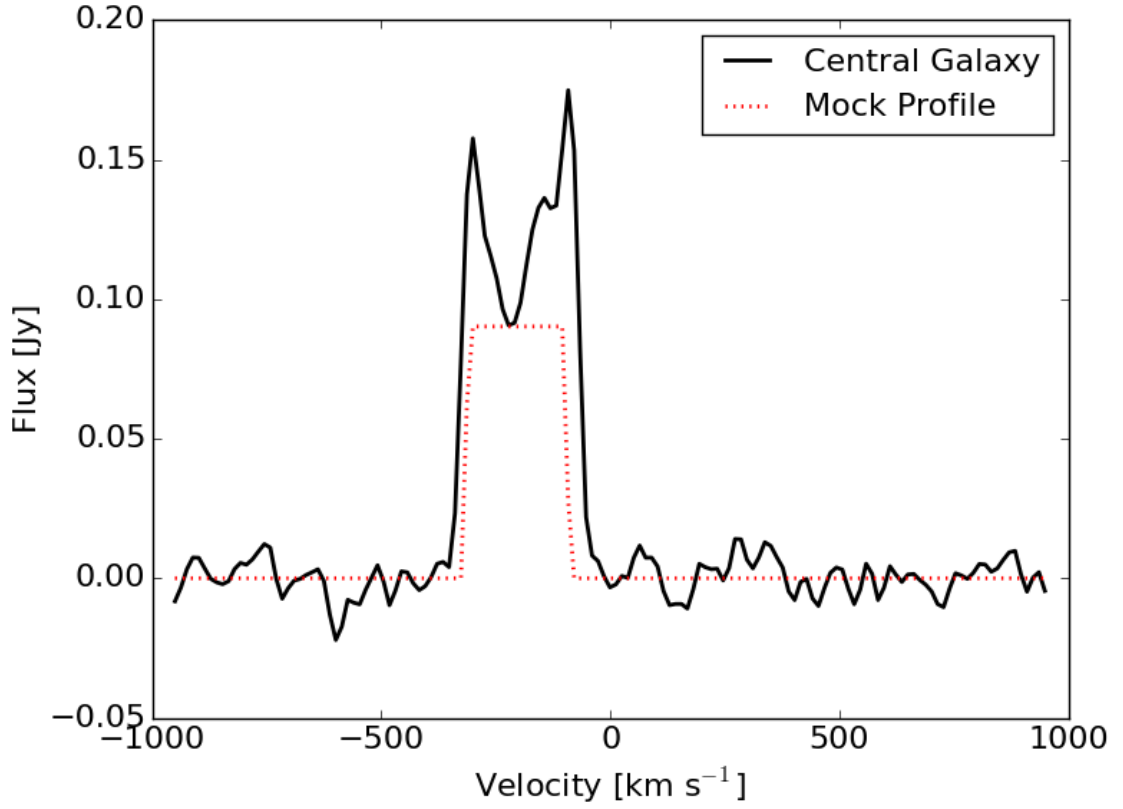
Fig. 4.5: An example of a unreliable spectrum (black solid line) excluded from the stack. There is no emission from the central galaxy centred at 0 km s^{-1}. However, there is clear HI emission from a nearby galaxy offset from the rest velocity of the central galaxy. The mock HI profile (red dotted line) constructed to estimate the flux contribution of nearby galaxies is clearly above the noise and less than than the peak flux of the spectrum. This spectrum is deemed unreliable and is subsequently removed from the sample.
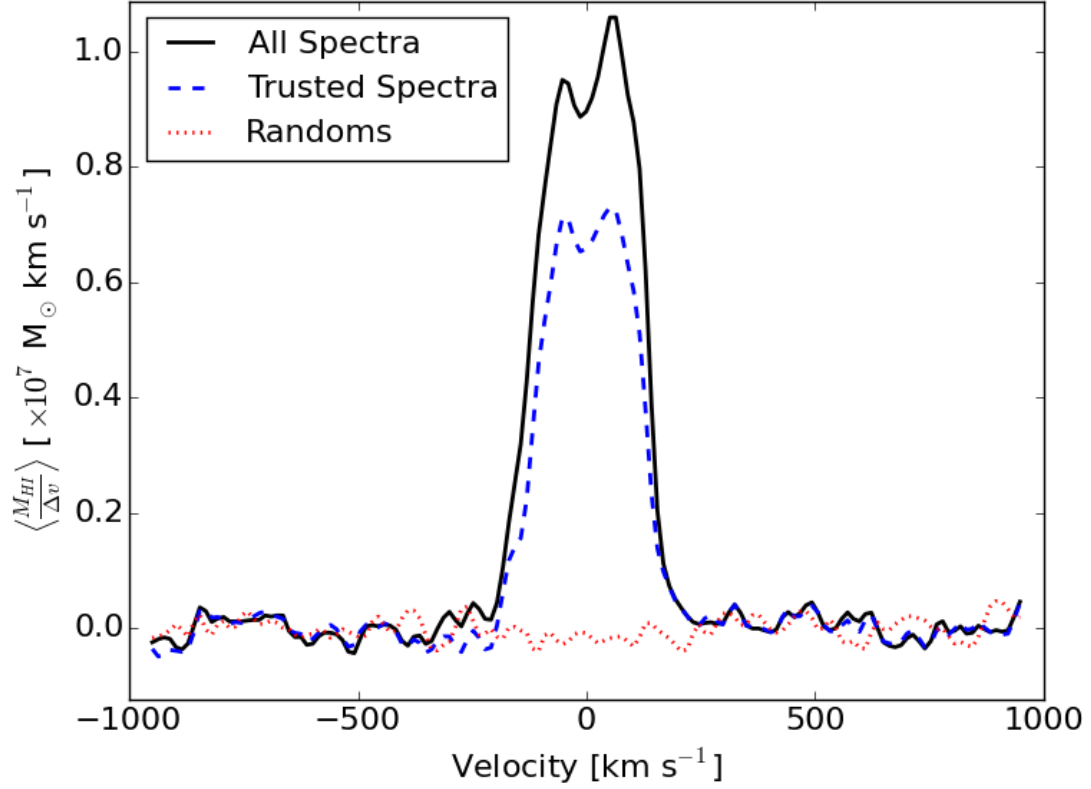
Fig. 4.6: The greatest difference between stacking all 619 spectra (solid black line) and removing 8 unreliable spectra (dashed blue line). The dotted solid red line is the random stack used to measure the uncertainty of the average HI mass. The flux of the reliable stacked profile (dashed blue) has significantly decreased by ∼20% compared to the stacked profile of all spectra (solid black). This decrease of flux is consistent with the expected contribution of neighbouring HI rich galaxies.

mass and local environment are known to affect the H$\textsc{i}$ fraction of a galaxy (e.g. Baldry et al., 2008; Catinella et al., 2010; Cortese et al., 2011; Brown et al., 2015) and we separate these quantities in subsamples to determine if the large scale filamentary environment affects the H$\textsc{i}$ fraction of galaxies with the same stellar mass and projected density.

Fig. 4.7 shows the H$\textsc{i}$ fraction in the near filaments and control sample for varying projected densities in four different stellar mass ranges. The H$\textsc{i}$ fractions decrease with increasing stellar mass range. For galaxies with stellar masses $\log(M_\star / M_\odot)$ < 11, the H$\textsc{i}$ fractions of the near filament samples is within 0.1 dex of the control samples. In this mass range, the H$\textsc{i}$ fractions are flat at the 3σ level. For galaxies with stellar masses $\log(M_\star / M_\odot) \geq 11$, the H$\textsc{i}$ fraction of the near filaments sample is systematically greater than the control sample. It statistically significant at the 4.9 and 5.5σ level where the difference is 0.6 and 0.75 dex at mean projected densities of 0.2 and 1.45 galaxies Mpc^{-2}. Assuming the H$\textsc{i}$ followed this trend, the difference between the near filament and control sample would be even more significant ($\sim$1 dex) at a mean projected density of 1.8 galaxies Mpc^{-2}.

4.6   Discussion

Two ideas currently being tested in galaxy evolution are: i) Whether galaxies near filaments evolve differently to galaxies far from filaments. ii) If any difference in evolution be explained purely by stellar mass and local galaxy density.

In the CWD model, stellar mass and local galaxy density are primary drivers of detaching galaxies from the cosmic web, ending cold gas accretion and quenches star formation. Our results suggest that galaxies with $\log(M_\star / M_\odot) > 11$ near filaments have not (or only recently) detached from the cosmic web and are still accreting cold gas from the cosmic web. Galaxies of the same mass in the same projected densities have already detached from the cosmic web and no longer have access to the cold gas of the cosmic web. This supports the natural motivation of the CWD model (Aragon-Calvo et al., 2016) and could be evidence for cold mode accretions (Kereš et al., 2005) with massive galaxies replenishing their gas content through cold gas accretion from the cosmic web.

This accretion does not enhance their gas content to the extent of making them gas rich, the low mass galaxies are clearly the most gas rich (highest H$\textsc{i}$ fraction). Instead,
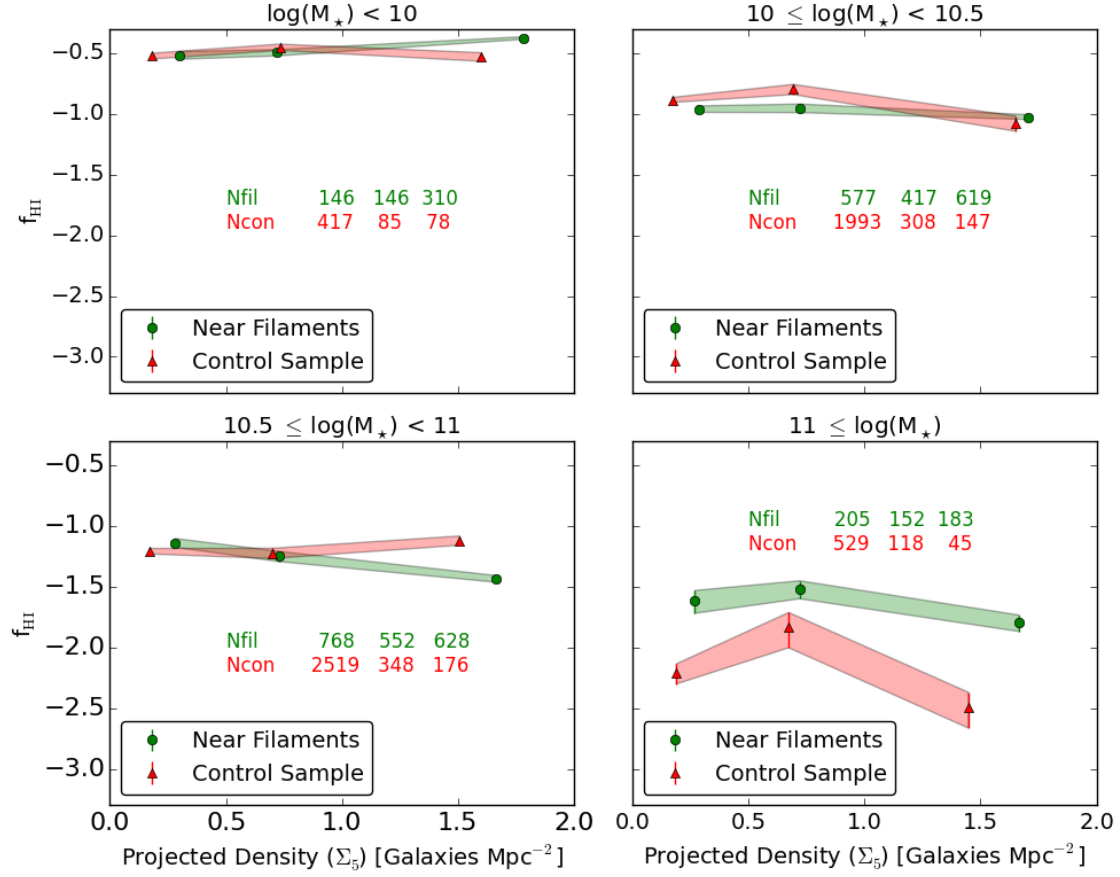
Fig. 4.7: The H I fraction in the near filaments (green circles) and control sample (red triangles) for varying mean projected densities in four different stellar mass ranges. The number of galaxies in each stack are shown in text with the same colours and the shaded regions signify the 1σ uncertainties derived from the rms and width of the stacked profile. The H I fraction as a function of projected density decreases for increasing stellar mass ranges in both the near filaments and control sample. For stellar masses $\log(M_\star / M_\odot) < 11$, the H I fractions are flat and indistinguishable from each other at the 3σ level. For stellar masses $\log(M_\star / M_\odot) \geq 11$, the near filaments H I fraction is significantly higher than the control sample by up to 0.75 dex with a 5.5σ significance. This difference occurs at a mean projected density of $\Sigma_5 = 1.45$ galaxies Mpc^{-2}.

the accretion gives them a slightly enhanced gas content compared to field galaxies of the same mass that are unable to accrete gas from filaments. If galaxies near filaments stay attached to the cosmic web for longer periods than galaxies far from filaments (as our results suggest), gas accretion from the cosmic web may be responsible for a burst of star formation observed on the outskirts of clusters (Porter et al., 2008; Mahajan, 2013). Star formation generally traces H I and is primarily correlated with stellar mass (e.g. Doyle & Drinkwater, 2006). As cosmic web gas is diffuse in the local Universe, any accretion would be second order compared to the H I and star formation driven by stellar mass and local galaxy density. Extra gas accreted from the cosmic web may require dense environments to trigger an appreciable difference in star formation.

We only observe a significant difference in H I fractions in the most massive galaxies in our sample. These galaxies near filaments are located at the deepest minima of the large-scale gravitational potential which would funnel the intra-filament gas onto the galaxies. The less massive galaxies have smaller gravitational potentials and no evidence of cold gas accretion from the large scale structure is observed.

Wang et al. (2015) show H I rich galaxies are surrounded by a H I rich environment where the gas is situated in clumps, hosted by small satellite galaxies or density peaks in the diffuse H I intergalactic medium. These observations also support the CWD model and are best explained by cold mode accretion. The H I rich galaxies in Wang et al. (2015) are rare and their contribution to the H I fractions in this study are averaged out. We are unable to directly compare our results to Wang et al. (2015) as their galaxies did not exceed $\log(M_\star / M_\odot) = 11$, where we see evidence for gas accretion from filaments. However, both this work and Wang et al. (2015) support the CWD model (Aragon-Calvo et al., 2016) and cold mode accretion (Kereš et al., 2005).

The H I content of galaxies can be influenced by local environment where the galaxy H I mass decreases with increasing local density (e.g. Cortese et al., 2011; Serra et al., 2012; Catinella et al., 2013). We do not observe a decreasing H I fraction for increasing projected densities as we impose maximum projected density of 3 galaxies Mpc^{-2} for galaxies in both our samples. This eliminates galaxies in high density environments (such as dense groups and clusters) where the aforementioned environmental trend is clearest. Therefore, we are probing low-to-intermediate projected densities and do not measure H I fractions where strong environmental mechanism remove H I gas from

galaxies. The H<small>I</small> fraction as a function of projected density is flat and indistinguishable between the near filaments and control sample for stellar masses $\log(M_\star / M_\odot)$ < 11 (Fig. 4.7 top and bottom left panels). The only H<small>I</small> fraction as a function of projected density that is different between the near filaments and control sample is for galaxies with stellar masses $\log(M_\star / M_\odot) \geq 11$ (Fig. 4.7 bottom right panel). As we have accounted for stellar mass and local environment, we attribute the difference in H<small>I</small> fractions to a galaxies proximity to filaments.

Previous studies have shown galaxies close to filaments possesses the same properties (Alpaslan et al., 2015) or very similar properties (Chen et al., 2015a; Guo et al., 2015; Alpaslan et al., 2016; Martínez et al., 2016) to galaxies of the same stellar mass but not filament members. The main conclusion from these studies is that any differences due to their filamentary environment are second order effects. While these studies were conducted in the optical and UV regime, we draw the same conclusion with the measured H<small>I</small> fractions for the majority of our sample with only high mass galaxies having a statistically different H<small>I</small> fraction but is still second order in comparison to the correlation of stellar mass with H<small>I</small> fraction.

The work of Chen et al. (2015b) show that the morphology-density relation can extend to the scale of filaments. As the galaxy density is higher in filaments than the field, it is reasonable to expect more (typically gas poor) early types in the near filament sample than the control sample. However, filaments host individual and small galaxy groups where the morphology and gas content depend on the dynamical history. If a filament galaxy has spent sufficient time in a dense group, it may have a bulge dominated morphology with no supply of cold gas. In this scenario, the galaxy has detached from the cosmic web as a result of strong group interactions. In principle, this may occur more in filaments than the field. However, filaments are environments of intermediate density and groups of this density are rare. Hence, interactions of this magnitude would not dominate the galaxy population in filaments. Even though the projected density of the samples used in this work are significantly different (Fig. 4.3), neither sample is inherently gas rich (or poor) as a result of its local environment.

Other studies (e.g. Alpaslan et al., 2015; Martínez et al., 2016) find the star formation rate and specific star formation rate is slightly lower in filament galaxies compared to the field. These trends are weaker when contrasting the star formation of cluster and field galaxies. Both filament and field galaxies span the full spectrum of gas poor to gas rich and passive to star forming. Similar to the gas content, star formation depends on the complex interplay of stellar mass, local galaxy density and cosmic

web attachment. All these factors should be considered when discerning the reason behind a galaxies gas content and star formation.

The HI fractions measured in this work rely on HIPASS observations that detected only the brightest HI galaxies in the nearby ($z < 0.043$) Universe. It is predicted that WALLABY (Koribalski, 2012) will observe HI in 6×10^5 galaxies out to a redshift of $z < 0.26$ and DINGO will detect up to 10^5 galaxies out to a redshift of $z < 0.43$ Duffy et al. (2012). WALLABY, DINGO and future SKA observations will be able to follow up HI measurements of $\log(M_\star / M_\odot) = 11$ galaxies near filaments which will provide better measurements of their HI fraction to determine if this accretion scenario is plausible.

4.7   Conclusions

Using 6dFGS and HIPASS we compare the HI fraction of galaxies near filament backbones to galaxies in a control sample far from filaments. The two samples are created using perpendicular filament distance and a maximum projected density that excludes galaxies in high density environments. The two samples have similar stellar mass distributions but significantly different projected density distributions. The HI fraction is measured using spectral stacking and we vary the stellar mass and projected density for both samples to disentangle what influences the HI gas in these galaxies. We find that:

- HI fraction is strongly correlated with a galaxy's stellar mass, where low mass galaxies have high HI fractions compared to massive galaxies. While the rate that galaxies build stellar mass depends on environment, the stellar mass can be used to estimate the HI fraction to first order. Local and large scale environments can also influence the HI fraction but these are second order effects compared to the stellar mass.

- We observe no significant difference in the HI fraction for varying projected densities between the near filaments and control sample for galaxies with stellar masses $\log(M_\star / M_\odot) \leq 11$. In this mass range, the HI fractions for the near filaments and control sample are indistinguishable from each other in all stellar mass subsamples. This implies that filaments have no influence of the HI content of galaxies compared to the correlation between HI content, stellar mass and local galaxy density.

- Galaxies near filaments with a stellar mass $\log(M_\star / M_\odot) \geq 11$ have a systematically higher Hı fraction for varying projected densities than the same mass galaxies in the control sample. This difference is most pronounced at projected densities of $\Sigma_5 = 0.2$ and 1.45 galaxies Mpc^{-2} where the statistical significance is 4.9 and 5.5σ. As stellar mass and local environment have been accounted for, we suggest this is tentative evidence of massive galaxies accreting cold gas from the intra-filament medium. Galaxies in the control sample do not have access to this gas reservoir and would be unable to replenish their cold gas supply. Only the most massive galaxies in filaments have a large enough gravitational potential to draw gas from the intra-filament medium.

- We observe no trend (at the 3σ level) in the Hı fractions for varying projected densities where the near filaments and control sample and indistinguishable from each other. Only galaxies with a projected density of 3 galaxies Mpc^{-2} were included in the near filaments and control sample, which confines this study to low and intermediate local environments. This threshold is implemented specifically to exclude high density (i.e. cluster) environmental mechanisms where galaxies are typically Hı deficient. The maximum density threshold is the reason we do not see a decreasing Hı fraction with increasing projected density.

Overall, the near filaments and control sample have the same Hı fraction as each other when varying the stellar mass and projected density. The exception arises for galaxies with stellar masses $\log(M_\star / M_\odot) \geq 11$. Our results are best explained by the cosmic web detachment model (Aragon-Calvo et al., 2016) that allows galaxies in this mass range to utilise cold mode accretion (Kereš et al., 2005). Through this mechanism, galaxies are able to accrete gas from the intra-filament medium and replenish their cold gas supply. This evidence is tentative and follow up observations with more sensitive radio telescopes (such as ASKAP and SKA) will be required to statistically support the proposed scenario.

This work is a pilot study for future redshift surveys and radio telescopes. Specifically, Taipan (da Cunha et al. in prep) will reveal the cosmic web and low mass galaxies in the Southern sky in much greater detail than 6dFGS. ASKAP and SKA will change our understanding of the Hı gas in galaxies where our analysis can be directly applied to WALLABY (Koribalski, 2012) and DINGO. We plan to use these surveys to follow

up our work and improve our understanding of the Hɪ content of galaxies within the cosmic web.

4.8   Appendix A: Filament Backbones found with DisPerSE

Here we show the filament backbones in eight 6dFGS redshift slices obtained with DisPerSE as described in section 4.3.2. The galaxies in each redshift slice are separated in two distinct sample – above ($b > 10°$) and below ($b < $ -10°) the Galactic Plane, which ensures DisPerSE does not spuriously connect filament backbones across the Galactic Plane. A density field is produced through computing the Delaunay tessellation on each galaxy distribution. Discrete Morse theory is directly applied to the Delaunay tessellation, identifying topologically important features. Filament backbones are recovered as long, thin topologically important features and a persistence ratio (i.e. signal-to-noise threshold, table 4.1) is chosen to retain filament backbones above the desired threshold. The persistence ratio chosen should reflect the filament backbones that can be visually verified in the galaxy distributions.
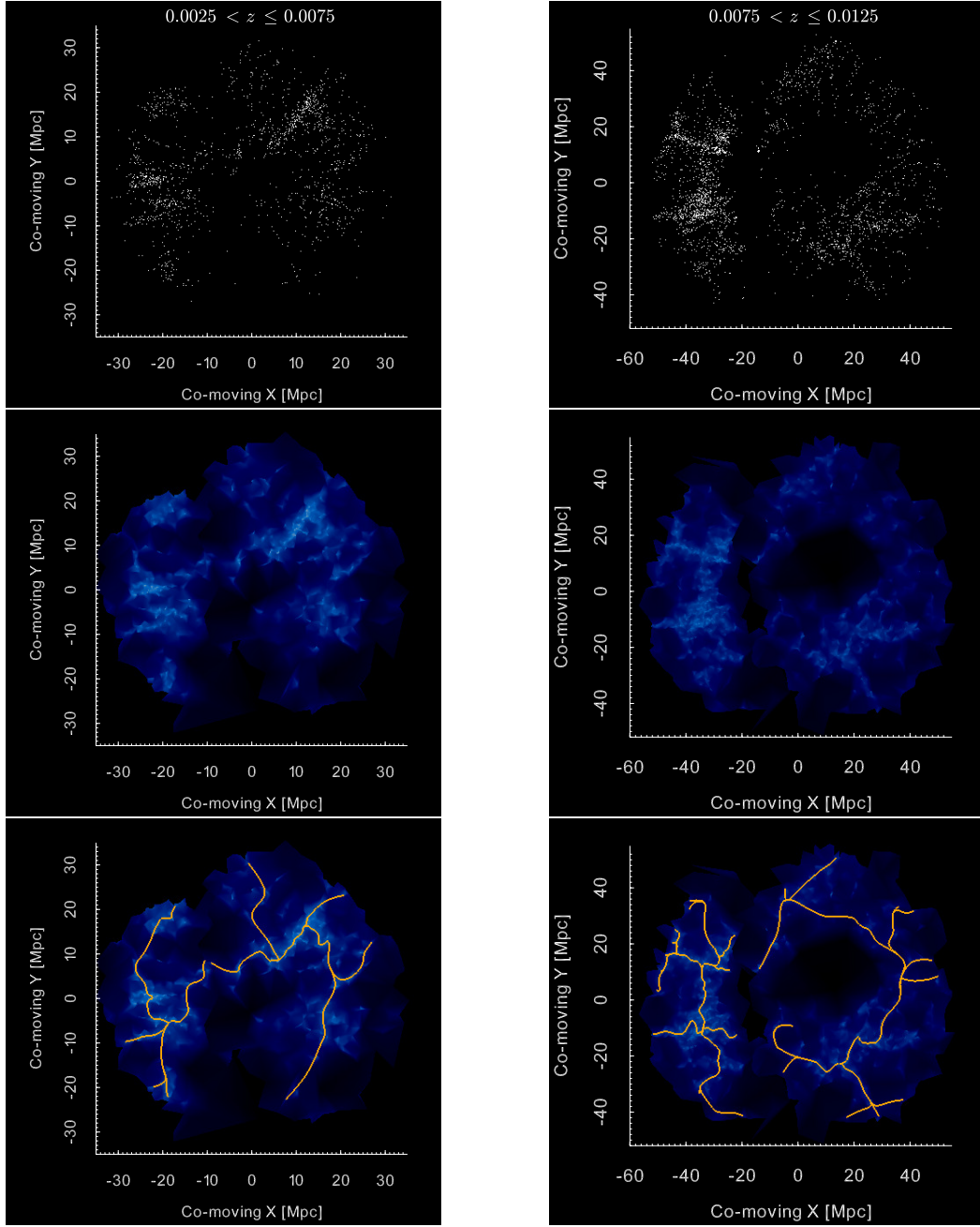
Fig. 4.8: Same as Fig. 4.1 showing the main steps of DisPerSE delineating filament backbones in redshift slices $0.0025 \leq z < 0.0075$ (left column) and $0.0075 \leq z < 0.00125$ (right column). The top panel shows all 6dFGS galaxies for the respective redshift ranges and the middle panel shows the corresponding Delaunay tessellations. The tessellation is coloured according to the local density field where underdense regions are darker colours and overdensities are lighter colours. The bottom panel has the filament backbones (orange lines) found by DisPerSE overlaid on the tessellation.

118
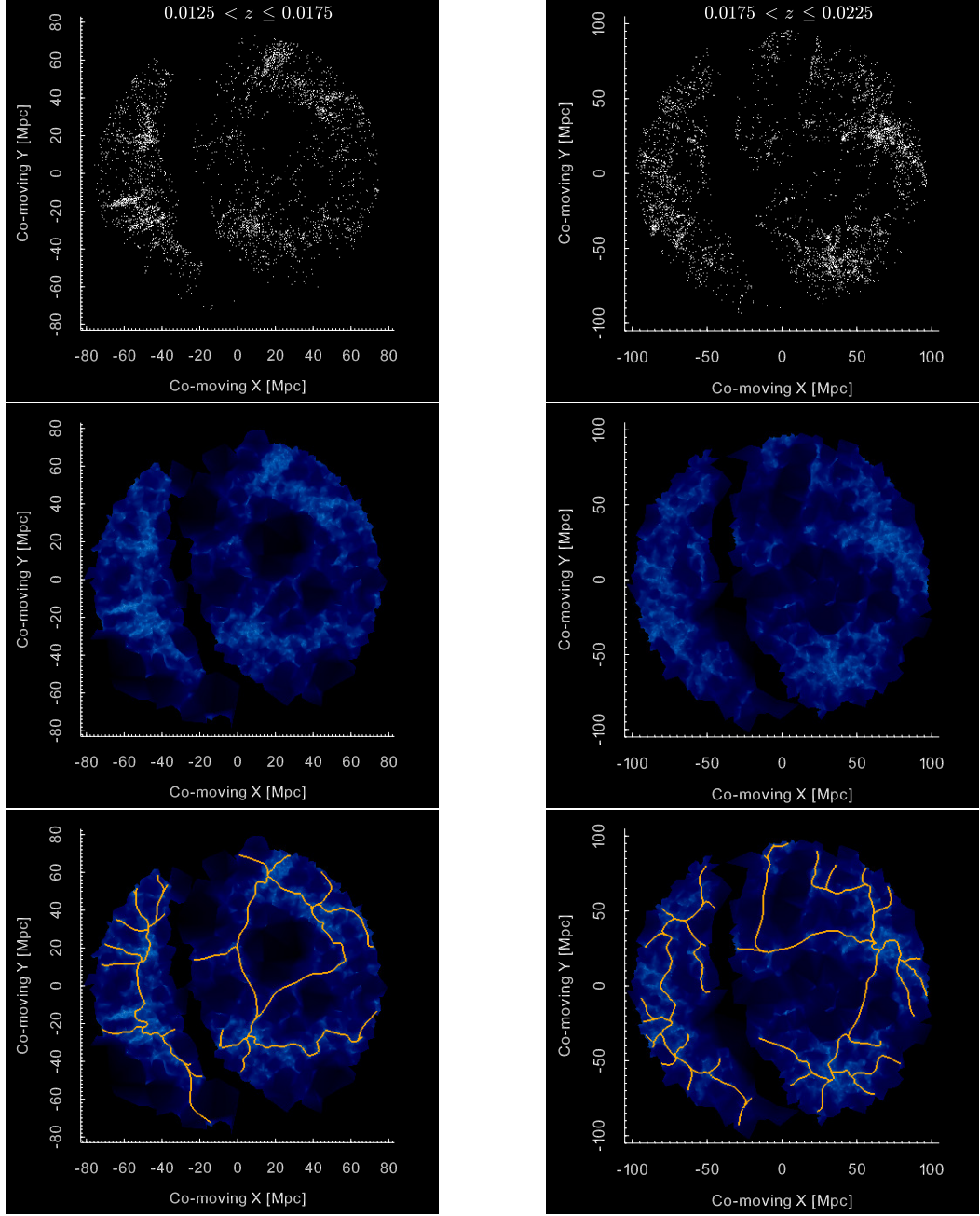
Fig. 4.9: Same as Fig. 4.8 for the redshift slices $0.0125 \leq z < 0.0175$ (left column) and $0.0175 \leq z < 0.00225$ (right column).
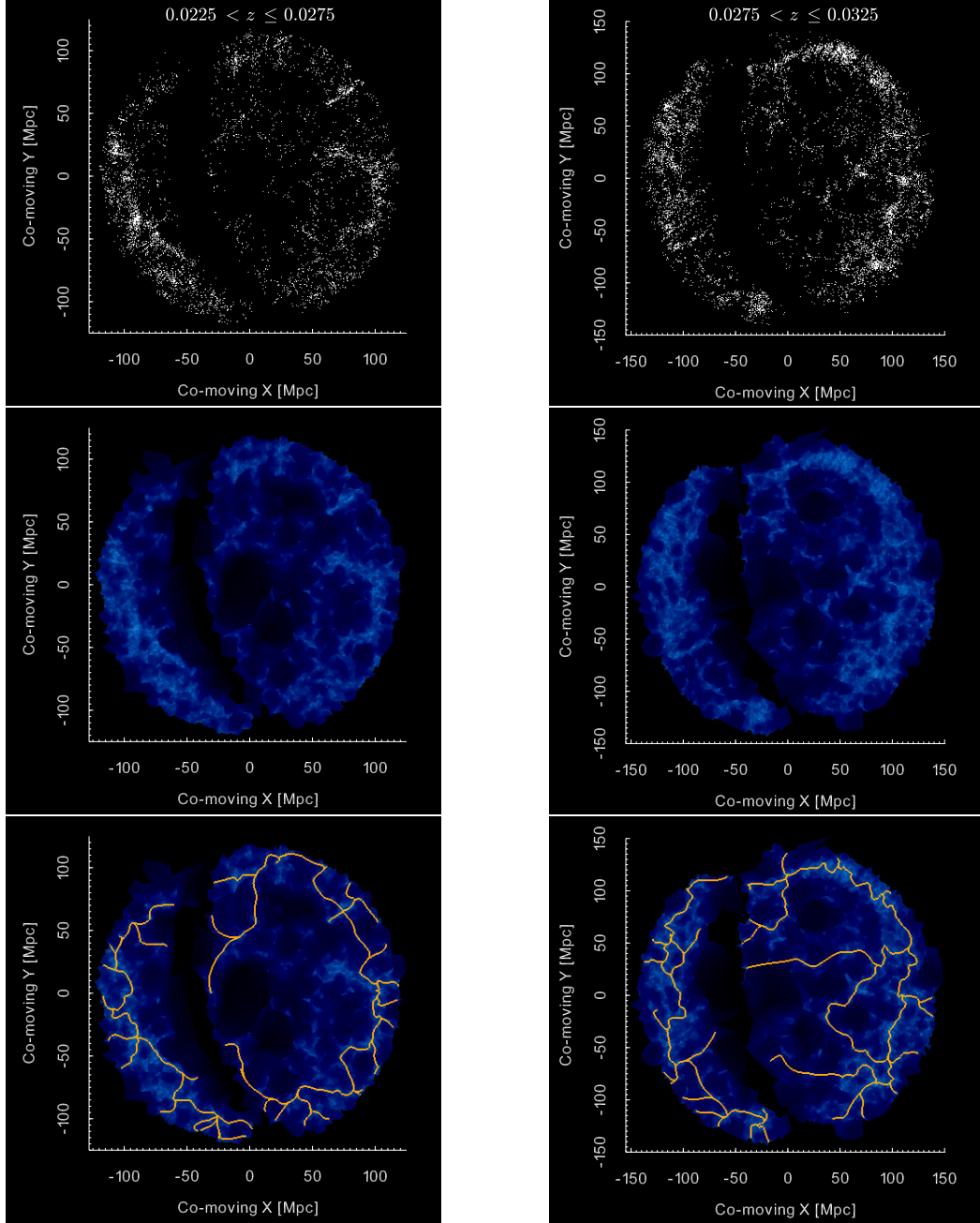
Fig. 4.10: Same as Fig. 4.8 for the redshift slices $0.0225 \leq z < 0.0275$ (left column) and $0.0275 \leq z < 0.00325$ (right column).
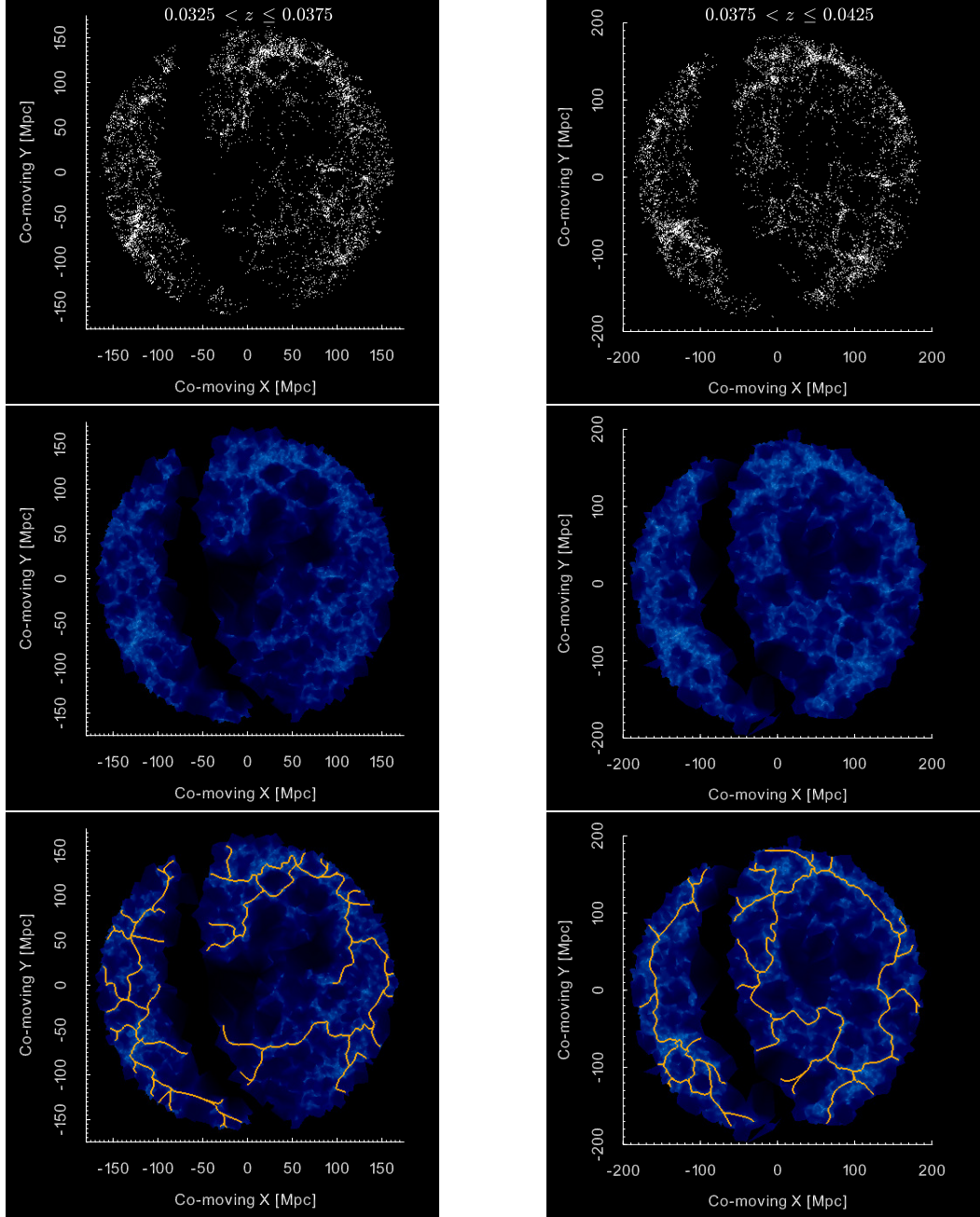
Fig. 4.11: Same as Fig. 4.8 for the redshift slices $0.0325 \leq z < 0.0375$ (left column) and $0.0375 \leq z < 0.0425$ (right column).

4.9 Appendix B: Comparison of two and three-dimensional filaments found with DisPerSE

In this appendix, we use the redshift slice $0.0375 < z \leq 0.0425$ to compare the filaments found with DisPerSE in two and three dimensions. This is the closest redshift slice in this work to the median redshift of 6dFGS and provides the optimal galaxy number density for classifying large scale structure.

Filaments found in two-dimensional data is described in section 4.3.2 and appendix 4.8. The filament backbones delineated in this way show good agreement with the visible cosmic web components and removes the dependance of falsely identifying spurious filaments in the z-direction from galaxies with large peculiar velocities.

To delineate filaments in three dimensions, an analogues method for the two dimensional case is used. The galaxies are split in to samples above and below the galactic plane, a Delaunay tessellation is produced from the three dimensional galaxy positions and filaments are extracted as the thin topologically significant features. This procedure is applied to all galaxies in 6dFGS within the HIPASS volume and Fig. 4.12 shows these steps for the galaxies, tessellation and filaments that exist between 0.0375 $< z \leq 0.0425$. Fig. 4.12 is the three-dimensional analogue of Fig. 4.11 (right panel). Filaments in both cases were extracted with the same persistence ratios ($\sigma_{pr} = 4.0$ and 4.8 for galaxies with $b > 10°$ and $b < $ -10°) and can therefore be directly compared to each other.

As the tessellation in Fig. 4.11 is two dimensional and the tessellation in Fig. 4.12 is three dimensional, we would not expect a one-to-one match of the topological features. However, they are a thin slice of the overall data and we expect the significant topological features to prevail in both tessellations. There is good agreement between the tessellations. For example, the high density ridges centred at (x,y) ≈ (-100, -80), (80, 150) and the large underdense region centred at (x,y) ≈ (70, 50) appear in both the two and three dimensional tessellations.

The filaments delineated in the two dimensional tessellation (Fig. 4.11 right bottom panel) clearly trace the thin density ridges that follow the network of the cosmic web. The filaments delineated in the three dimensional tessellation (Fig. 4.12 bottom panel) are in the general location of the thin density ridges but they are a poor match to the network of the cosmic web. There are many more filaments found in the three dimensional case and they appear to unnecessarily twist and turn. The three
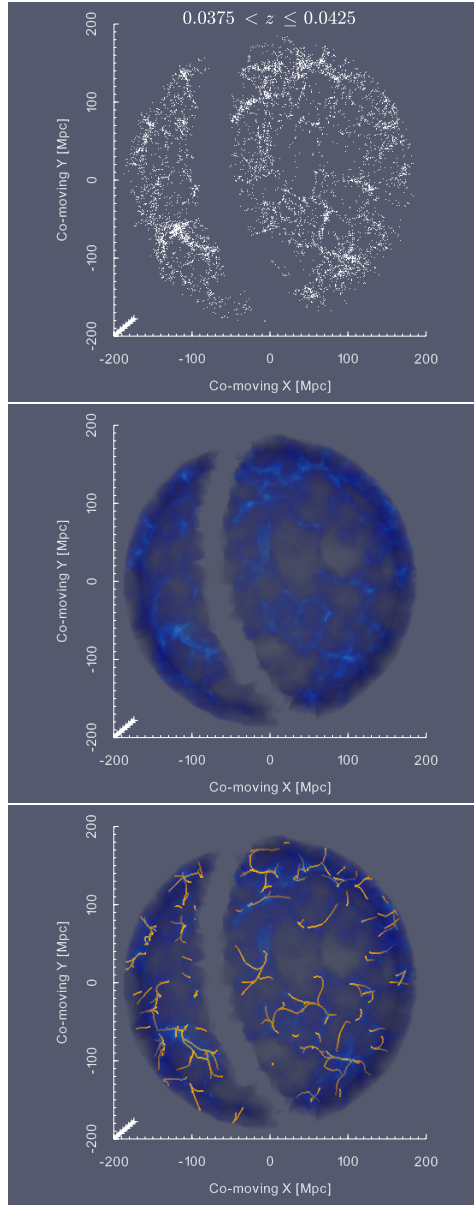
Fig. 4.12: The main steps of DisPerSE delineating filament backbones in three dimensions showing the results within $0.0375 \leq z < 0.0425$. The top panel shows all 6dFGS galaxies in the redshift range. The middle panel shows the corresponding Delaunay tessellation coloured by local density field with darker colours representing underdense regions and lighter colours highlighting the overdensities. The Delaunay tessellation in three dimensions is a volume compared to a surface in the two dimensional case (middle panel of each figure in appendix 4.8. The bottom panel overlays the filament backbones (orange lines) found by DisPerSE with persistence ratios σ_{pr} = 4.0 and 4.8 for galaxies above and below the galactic plane. This sequence is the three dimensional analogy of the right panel of Fig. 4.11. While the tessellations show similar topological features in two and three dimensions, the filaments found are significantly different. The filaments found in two dimensions (Fig. 4.11) trace the density ridges well, but the filaments in the three dimensions (bottom panel of this figure) appear unnecessarily complex and do not trace the thin features of the cosmic web.

dimensional filaments appear to preferentially circumscribe voids rather than trace the thin density ridges of the tessellation. While this may be an attempt at following the three-dimensional geometry of filaments, it defines numerous filaments in unrealistic regions and the reproduction of the cosmic web is unsatisfactory. Therefore, the filaments found in three dimensions do not match the two dimensions filaments defined in the same volume.

We create *near filament* samples from the filaments backbones to compare which galaxies would be included in this analysis using the two and three dimensional filament delineation (Fig. 4.13). The two dimensional sample is described in section 4.3.3 with galaxies being included if they are within 0.7 Mpc of filament backbones and a projected density of $\Sigma_5 < 3$ galaxies Mpc^{-2}. The three dimensional sample includes galaxies within 0.7 Mpc of filaments with no (projected) density restriction, making the number of galaxies included in this sample an upper limit. There are 1 011 and 735 galaxies in the two and three dimensional near filament samples. The two dimensional sample outlines the filamentary structures in that redshift range while the three dimensional does not coherently trace the filamentary structures. Analogous to the tessellations, we do not expect the galaxies samples to exactly match in number or geometry. However, we are comparing a thin redshift slice and expect the main geometry of the samples to match. This is a reasonable expectation as the width of the redshift slice include galaxies within $\pm$ 750 km s^{-1}, a velocity spread on the order of the Virgo clusters velocity dispersion. In this comparison, we find the galaxy distribution of the near filament samples in three dimensions does not reproduce the filaments of the cosmic web or match the main geometry of the two dimensional near filament sample.

As we have found a systematic and reliable technique for delineating filaments in the nearby Universe (section 4.3.2), it is beyond the scope of this work to fully determine the cause of the discrepancies between delineating filaments in two and three dimensions. We believe the following two factors are likely to be responsible for the discrepancies; i) The peculiar velocities of galaxies in the nearby Universe are too high to coherently trace the three dimensional geometry of filaments and ii) The requirement for filaments in DisPerSE to circumscribe voids over powers tracing the thin density ridges. Both of these factors can explain why the three dimensional delineation of filaments with DisPerSE was found to be unsatisfactory and we will determine the cause in a future study.
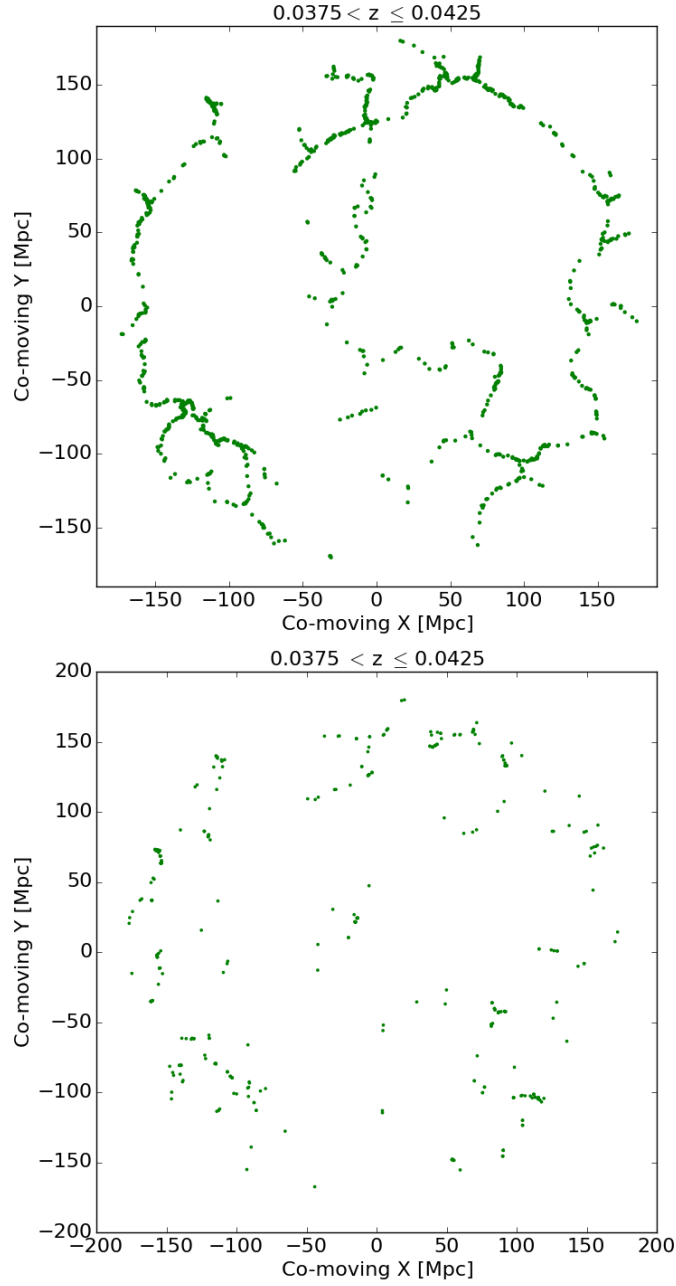
Fig. 4.13: A comparison of the galaxies (green points) contained in the near filament samples produced in two (top panel) and three (bottom panel) dimensions. The two dimensional sample consists of 1 011 galaxies and was defined as galaxies within 0.7 Mpc of a filament backbone and a projected density of $\Sigma_5 < 3$ galaxies Mpc^{-2}. The three dimensional sample consists of 735 galaxies and was defined as galaxies within 0.7 Mpc with no (projected) density restriction. The two dimensional near filament sample produces filamentary structures while the three dimensional near filament sample does not. We expect the main geometry of the samples to match as this is a comparison in a thin redshift slice. The three dimensional near filament sample does not produce a satisfactory sample of filament galaxies and we use the two dimensional sample definition in this work.

The technique used in this work to delineate filaments in two dimensions is analogous to the technique used by Chen et al. (2015b,a) who split SDSS in to thin redshift slices (same thickness of $\delta z = 0.005$ used in this work) to delineate filaments in two dimensions and study the optical properties of filament galaxies.

CHAPTER 5

The star forming fraction and efficiency of 6dFGS filament galaxies

5.1 Overview

In this chapter we extend our findings from Chapter 4 and connect the HI content to the star formation of filament galaxies. We extract photometry from the Wide-Field Infrared Survey Explore (WISE; Wright et al., 2010) that satisfies 3 photometric quality conditions and measure SFRs using the Cluver et al. (2014) relation for the near filament and control sample. Using the SFRs, we determine the star forming fraction and star formation efficiency (SFE) of galaxies in these two samples. The star forming fraction is defined using $\log(\text{SSFR} / \text{yr}^{-1}) > -11$, a relation only galaxies with at least an intermediate SSFR will satisfy (e.g. Schiminovich et al., 2007; Salim et al., 2007; Salim, 2014). The SFE is the SFR-to-HI-mass ratio and is a direct measure of how efficiently the galaxy is currently converting HI to stars. Consolidating these measures, we search for evidence of quenching in filament galaxies, a key question of this thesis.

After normalising the effects of stellar mass and projected density for the samples, we find the fraction of star forming galaxies to be indistinguishable between galaxies in the near filament and control sample. The SFE is found to be significantly lower in filament galaxies with $\log(M_\star / M_\odot) > 11$. In Chapter 4, the same galaxies were found to have higher HI fractions than the control sample and these results suggest filament galaxies are not as efficient at converting HI to stars than galaxies far from filaments. As both samples have the same fraction of star forming galaxies, the SFE is lower in filament galaxies as a result of the higher HI mass. There is no known mechanism that prevents HI gas from forming stars without heating or stripping it. Therefore, the most likely scenario to explain these findings is that the additional

Hɪ gas in filament galaxies is too diffuse and has not reached the critical density to collapse and form stars. This is consistent with our findings in Chapter 4 as the difference in Hɪ fractions was attributed to gas accretion from the IGM that is very diffuse (n $\lesssim 10^{18}$ cm^{-2}).

5.2 Introduction

As discussed in Chapter 1.2.2, the star formation of a galaxy is an essential component of galaxy evolution. It gives us direct insight to the stellar population of the galaxy and can be directly linked to internal processes regulating star formation, the dynamical state of the galaxy and its immediate environment (Kennicutt, 1998). The process of star formation is inextricably linked to the mass and immediate environment of the galaxy. Massive galaxies with large gravitational potentials can retain significant quantities of cold gas that can collapse and form new stars (e.g. Noeske et al., 2007). Galaxies build mass through mergers and accreting surrounding material (De Lucia & Blaizot, 2007). As this occurs, star formation can be quenched as gas in the galaxy is often stripped or heated (e.g. Gunn & Gott, 1972; White & Rees, 1978; Barnes & Hernquist, 1991; Crowl et al., 2005; Cen, 2011). Such quenching occurs in all local galaxy environments and is known to occur frequently in dense environments (e.g. Balogh et al., 2004; Kauffmann et al., 2004; Baldry et al., 2008). Quenching is required to reproduce the galaxy colour bimodality and a galaxy can have its star formation quenched if it is massive or in a high density environment (Benson et al., 2003; Croton et al., 2006). While massive galaxies have the ability to have a high SFR, they are often inefficient at forming new stars as a result of the physical process that build mass and their immediate environment.

While the relation between SFR, mass and immediate environment has been studied in detail (e.g. Baldry et al., 2006; Bamford et al., 2009; Peng et al., 2010; Sobral et al., 2011; Brough et al., 2013; Guglielmo et al., 2015), whether filaments of the cosmic web impact galaxy SFR has only been studied in the past few years. Recently, theoretical models and observational evidence for galaxy quenching occurring in filaments has been presented in the literature and we discuss their details in Chapter 1.4.2. The main findings from these studies are briefly described below.

The prevailing theoretical model is the cosmic web detachment (CWD) model. It is a comprehensive framework where galaxy quenching naturally occurs when non-linear

interactions sever its connection to the cosmic web (see Fig. 1.9 for three examples). Through observations of stellar mass, colour, morphology and SSFR, filament galaxies appear to be more quenched than non-filament galaxies (Chen et al., 2015b; Alpaslan et al., 2016; Poudel et al., 2016). It is possible that filaments regulate the star formation (and thus evolution) of galaxies although there is no current consensus on what the quenching mechanism(s) are and how efficiently they operate.

Previously, in Chapter 4 we found 6dFGS filament galaxies with $\log(M_\star / M_\odot) > 11$ have a higher HI fraction than non-filament galaxies. The discrepancy was best explained by filament galaxies accreting cold gas from the cosmic web to replenish their HI content. Our results support the CWD model (Aragon-Calvo et al., 2016) in a scenario where the high mass filament galaxies have not disconnected from the cosmic web. As high mass galaxies are typically gas poor with quenched star formation, another possibility is that the filament galaxies have more recently detached from the cosmic web compared to the non-filament galaxies. These scenarios show no clear evidence of quenching and the purpose of this chapter is to consolidate the HI content of filament galaxies with their SFR to search for quenching evidence. We use WISE photometry (Wright et al., 2010) to derive SFRs of 6dFGS filament and non-filament galaxies. The SFRs are combined with the HI masses from Chapter 4 to measure the star forming fraction and efficiency. Combining these two quantities to search for galaxy quenching in filaments is an unexplored area and we utilise this novel technique to address a key question of this thesis.

5.3   Measuring SFRs with WISE photometry

There are a variety of observational techniques used to estimate SFRs. They can directly measure emission from hot young stars or measure the effects of the emission in the immediate surroundings of the stars. The different techniques measure SFRs on different timescales and there is intrinsic scatter and uncertainty present in all estimates (Davies et al., 2015).

WISE is an IR telescope that has surveyed the whole sky in four infrared bands (W1-W4) centred on 3.4, 4.6, 12 and 22 μm (Wright et al., 2010). In the nearby ($z \sim 0$) Universe, WISE photometry is sensitive to warm dust that has been thermally heated by hot young stars and is largely unaffected by dust attenuation when estimating SFRs. The W3 band is commonly used to measure SFRs as it has better sensitivity

than the W4 band and is affected less by foreground stars than the W1 and W2 bands. The W3 band detects emission from warm HII regions (thermally heated by hot young stars) and polycyclic aromatic hydrocarbons (PAHs) that are found throughout molecular clouds (e.g. Jarrett et al., 2013; Cluver et al., 2014).

5.3.1 Sample selection

In order to extract WISE photometry for 6dFGS galaxies, we search the ALLWISE database[1] with a $6''$ aperture (which is the same size as the W3 band resolution) centred on the position of each 6dFGS galaxy. The ALLWISE database is a combination of improved multi-epoch photometry from the WISE and NeoWISE surveys (Wright et al., 2010). Galaxies with a one-to-one match to a WISE source are retained for this analysis as galaxies matched to multiple WISE sources have been shredded into multiple components, making their photometry unreliable and are consequently discarded. Shredding only occurs for nearby resolved (i.e. $\gg 6''$) galaxies that appear clumpy. The median redshift of 6dFGS is $z_{\frac{1}{2}} = 0.053$ meaning that only a few galaxies in our sample are very nearby and sufficiently well-resolved to show that they are shredded. Any unresolved source in 6dFGS is unresolved in the WISE W3 band as the 6dFGS fibre size ($6.7''$) is within $1''$ of the W3 resolution.

We use the same *near filament* and *control sample* constructed in Chapter 4. Briefly, filament backbones were delineated in 6dFGS using DisPerSE in thin ($\delta z = 0.005$) redshift slices between $0.0025 \leq z < 0.0425$. Near filament galaxies are chosen to be within 0.7 Mpc of a filament backbone with projected density $\Sigma_5 < 3$ galaxies Mpc^{-2} and control sample galaxies are chosen to be greater than 5 Mpc from filament backbones with projected density $\Sigma_5 < 3$ galaxies Mpc^{-2}.

There are a total of 4 543 near filament and 6 851 control sample galaxies with *reliable* WISE photometry, corresponding to 85% of the original samples used in Chapter 4. This is a lower limit as reliable WISE photometry meets a minimum photometric quality (discussed below) and will not removed from the samples. In contrast, galaxies are sometimes removed from the original samples in Chapter 4 due to having unreliable HI spectra.

---

[1] http://irsa.ipac.caltech.edu/cgi-bin/Gator/nph-dd

5.3.2 Photometry choice and quality

There are many different apertures used to measure WISE photometry in the ALL-WISE catalogue. The choice of aperture should reflect the nature of the sample, specifically the distance of the sources and whether they are point, extended or resolved.

Our galaxy samples reside within $z < 0.0425$ making the majority of them extended IR sources. The best choice of photometry is the elliptical (*gmag*) WISE photometry that we use when available. The *gmag* photometry is measured using apertures scaled from the 2MASS XSC (Jarrett et al., 2000) shape and captures the total surface brightness better than the standard WISE photometry. Most 6dFGS galaxies originate from the 2MASS XSC, making the *gmag* photometry the most applicable measurements to use in this analysis. For 6dFGS galaxies that do not have *gmag* photometry, we use the 11″ aperture photometry as that is the largest aperture in the ALLWISE catalogue and has the best chance of capturing a reasonable surface brightness profile for extended objects. At the furthest distance of our sample ($z = 0.0425$), 11″ corresponds to a distance of 9.3 kpc.

There exist many unwanted features (such as diffraction spikes, dead pixels or artefacts in the data reduction process, etc) that can contaminate photometric measurements. A number of WISE photometry quality flags are available in the ALLWISE catalogue and we ensure the photometry measured for our galaxies meet the following minimum standard to be considered reliable. Only galaxies that are unaffected by known artefacts (`cc_flg = 0`), with reliable pixels (`w3flg < 8`) and trusted photometry (`ph_qual` $\neq$ U, X or Z) are retained for this analysis[2]. There are more photometric quality flags available, but the combination of these three produced a CMR with no apparent systematics.

5.3.3 Measuring SFRs

To measure the SFR for each 6dFGS galaxy, we must first measure the W3 absolute magnitude:

$$M_{W3} = m_{W3} - 5 \log_{10} \left(\frac{D_L}{10} \right) - k_{W3} \ . \tag{5.1}$$

---

[2]For detailed explanations of these flags and other measures of WISE photometry, visit http://wise2.ipac.caltech.edu/docs/release/allwise/expsup/sec2_1a.html.

The apparent W3 magnitude (m_{W3}) is obtained from the *gmag* / aperture photometry, D_L is the luminosity distance to the galaxy in pc and k_{W3} is the k-correction for each galaxy that have been approximated using W3 – W2 colours based on the spectral energy distribution templates of Brown et al. (2014).

The W3 luminosity in units of solar luminosity ($L_\odot$) for each galaxy is found with

$$L_{W3} = \frac{L_0 10^{\left(\frac{-M_{W3}}{2.5}\right)}}{L_\odot} \ , \tag{5.2}$$

where $L_0 = 3.79 \times 10^{11}$ $L_\odot$ as it is the luminosity of an object with a W3 apparent magnitude of 0 at a distance of 10 pc, M_{W3} is the W3 absolute magnitude of the galaxy (obtained from equation 5.1) and $L_\odot = 3.84 \times 10^{26}$ W is the solar luminosity.

The SFR is derived for each 6dFGS galaxy with reliably matched WISE photometry using the relation defined in Cluver et al. (2014). This relation was calibrated with Hα derived SFRs (Gunawardhana et al., 2013), can be seen in Fig. 1.6 and is defined as

$$\log_{10}(\text{SFR}) = 1.13 \log_{10}(\nu L_{W3}) - 10.24 \ . \tag{5.3}$$

The SFR is measured in $M_\odot$ yr^{-1}, the effective W3 frequency $\nu = 2.48 \times 10^{13}$ Hz and L_{W3} is the luminosity in the W3 band of the galaxy measured in equation 5.2.

There is considerable scatter in this SFR estimate (Fig. 1.6) and some known systematics exist in the WISE photometry. PAH emission originate from star forming regions but strong PAH emission can be the primary cause of large scatter in this band (Smith et al., 2007). Additionally, WISE photometry is optimised for point sources. Even though there is photometry for extended sources (*gmags*), they are known to underestimate the flux for low surface brightness and resolved sources (Jarrett et al., 2013; Cluver et al., 2014). These systematic effects are minimised by using 6dFGS due to its brighter flux limits (~ 1 to 2 mags) relative to its parents 2MASS sample. Some underestimated fluxes for nearby resolved galaxies will be present in our analysis but they will exist in both the near filament and control sample opposed to preferentially existing in one sample. This analysis utilises a large statistical approach that does not require precision photometry as we search for physical differences by quantifying the relative difference between the near filament and control sample.

5.4 The star forming fraction of filament galaxies

Using the SFRs estimated from WISE photometry, we calculate the SSFR for each galaxy as

$$\mathrm{SSFR} = \frac{\mathrm{SFR}}{\mathrm{M}_\star} \ . \tag{5.4}$$

For each galaxy, the SSFR in yr^{-1} is obtained using the SFR from equation 5.3 and the stellar mass ($\mathrm{M}_\star$) in $\mathrm{M}_\odot$. A SSFR of $\log_{10}(\mathrm{SSFR} \ / \ \mathrm{yr}^{-1}) = -11$ is the threshold between low and intermediate star forming galaxies. Martínez et al. (2016) use $\log_{10}(\mathrm{SSFR} \ / \ \mathrm{yr}^{-1}) < -11$ to define a sample of low star forming galaxies and $\log_{10}(\mathrm{SSFR} \ / \ \mathrm{yr}^{-1}) = -11$ has previously been used to define galaxies with an intermediate SSFR (Schiminovich et al., 2007; Salim et al., 2007; Salim, 2014). Retaining consistency with these definitions, we define the fraction of star forming galaxies as

$$\mathrm{f_{SF}} = \frac{\mathrm{N}(\log_{10}(\mathrm{SSFR}) > -11)}{\mathrm{N}(\mathrm{sample})} \ , \tag{5.5}$$

where the numerator is the number of galaxies in the sample that satisfy $\log_{10}(\mathrm{SSFR} \ / \ \mathrm{yr}^{-1}) > -11$ and the denominator is the total number of galaxies in the sample. This measures the fraction of galaxies actively forming stars relative to its stellar mass, enabling a normalised comparison of star formation activity between galaxies with different stellar masses.

The stellar mass and local environment are known to affect the SFR of a galaxy (e.g. Balogh et al., 2004; Kauffmann et al., 2004; Poggianti et al., 2006; Baldry et al., 2006; Bamford et al., 2009; von der Linden et al., 2010; Lin et al., 2016) and we separate the near filament and control sample in to stellar mass and projected density samples (same as Chapter 4). By normalising our samples by these quantities, we use the fraction of active galaxies to search for quenching in filaments.

In Fig. 5.1 we present the fraction of star forming galaxies (defined in equation 5.5) for the near filament and control sample. The fraction of star forming galaxies as a function of projected density decreases with increasing stellar mass for both samples. Galaxies with $\log(\mathrm{M}_\star \ / \ \mathrm{M}_\odot) < 10$ have a mean star forming fraction of 0.78 ± 0.04 compared to the mean star forming fraction of 0.27 ± 0.03 for galaxies with $\log(\mathrm{M}_\star \ / \ \mathrm{M}_\odot) > 11$. There is a decrease in the star forming fraction with projected density but this trend is less significant compared to the fraction of star forming galaxy's

dependence on stellar mass. We do not observe any significant difference in the fraction of star forming galaxies between the near filament and control sample as a function of projected density in any stellar mass bin. Therefore, no quenching is observed using this measure of star formation activity.

5.5 The star formation efficiency of filament galaxies

Using the SFR, we measure the star formation efficiency (SFE) for a sample of galaxies as

$$SFE = \frac{SFR}{M_{HI}} \; , \tag{5.6}$$

where the SFR in $M_\odot$ yr^{-1} is measured from equation 5.3 and the H$\textsc{i}$ mass in $M_\odot$ is measured through spectral stacking described in Chapter 4. The SFE (in yr^{-1}) measures how efficiently an observed galaxy converts cold gas to stars (Schiminovich et al., 2010; Huang et al., 2012; Wong et al., 2016).

We split the near and filament samples in to subsamples of stellar mass and projected galaxy density in the same way as Fig. 4.7 and Fig. 5.1.

In Fig. 5.2 we show the SFE (defined in equation 5.6) for the near filament and control sample. The SFE as a function of projected density increases with higher stellar mass subsamples for both samples. Although, there is more scatter present in this trend than the fraction of star forming galaxies trend with stellar mass (Fig. 5.1). Essentially, this reflects that high mass convert the most cold gas into stars. The SFE as a function of project density displays no clear trend and appears flat at a 3σ level in both samples. While scatter is present in Fig. 5.1, there is suggestive evidence of a systematic offset in the SFE between the near filament and control sample for galaxies with $\log(M_\star \, / \, M_\odot) \geq 11$. In this mass range, the near filament sample has a lower SFE by 0.65 and 0.55 dex at project densities of 0.25 and 1.25 galaxies Mpc^{-2}. This offset is significant by 4.0 and 3.6σ at these projected densities. However, there is no statistical significance at the middle projected density of 0.7 galaxies Mpc^{-2}. We suggest the observed difference in the SFE between the near filament and control sample is a result of massive filament galaxies having their star formation quenched

Fig. 5.1: The fraction of star forming galaxies as a function of projected density for the near filament (green circles) and control sample (red triangles) in different stellar mass bins. The shaded regions signify 1σ uncertainties obtained from the binomial error measurement. For both samples, the fraction of star forming galaxies decrease with stellar mass and decrease less significantly with increasing projected density. There is no significant difference in the fraction of star forming galaxies as a function of projected density between the near filament and control sample in any stellar mass bin.

in comparison to galaxies with the same mass in the same local environment that are far from filaments.

5.6   Interpretation

A variety of recent studies favour the filamentary environment having a mild influence on a galaxy's star formation, that is second order to stellar mass and local galaxy density (Chen et al., 2015b; Guo et al., 2015; Alpaslan et al., 2016; Martínez et al., 2016; Aragon-Calvo et al., 2016). The work of Poudel et al. (2016) propose a far more efficient mechanism that operate in filaments and quench star formation. A consensus has not been made on the extent filaments can influence star formation and there is contention if filaments can influence the star formation of a galaxy at all (e.g. Alpaslan et al., 2015).

The fraction of star forming galaxies we measure as a function of projected density in different stellar mass bins (Fig. 5.1) adheres to the known relation between star formation, mass and environment (e.g. Baldry et al., 2006; Peng et al., 2010; Brough et al., 2013). In both the near filament and control sample, the fraction of star forming galaxies decrease with stellar mass and less significantly with projected density. Taking these trends into consideration, there is no significant difference in the fraction of star forming galaxies as a function of projected density between the near filament and control sample in any stellar mass bin. The trends in the fraction of star forming galaxies can be explained purely by stellar mass and local galaxy density and there is no evidence for filaments influencing this measure. Using the fraction of star forming galaxies, we do not observe any evidence of quenching occurring in filaments. While other studies (e.g. Chen et al., 2015b; Alpaslan et al., 2016; Martínez et al., 2016) find evidence for quenching in filaments, it is possible the fraction of star forming galaxies is not sensitive enough to show any significant evidence of quenching on this scale.

The SFE as a function of projected density (Fig. 5.2) increases with stellar mass for both the near filament and control sample. Despite galaxies with $\log(M_\star / M_\odot)$ < 10 being the most active, it is the galaxies with $\log(M_\star / M_\odot)$ > 11 that are the most efficient at converting cold gas to stars. Our SFEs are centred around $\sim \log(9.5)$ yr^{-1} and are consistent with previous SFE measures (Schiminovich et al., 2010; Huang et al., 2012; Wong et al., 2016). The SFE is inversely proportional to
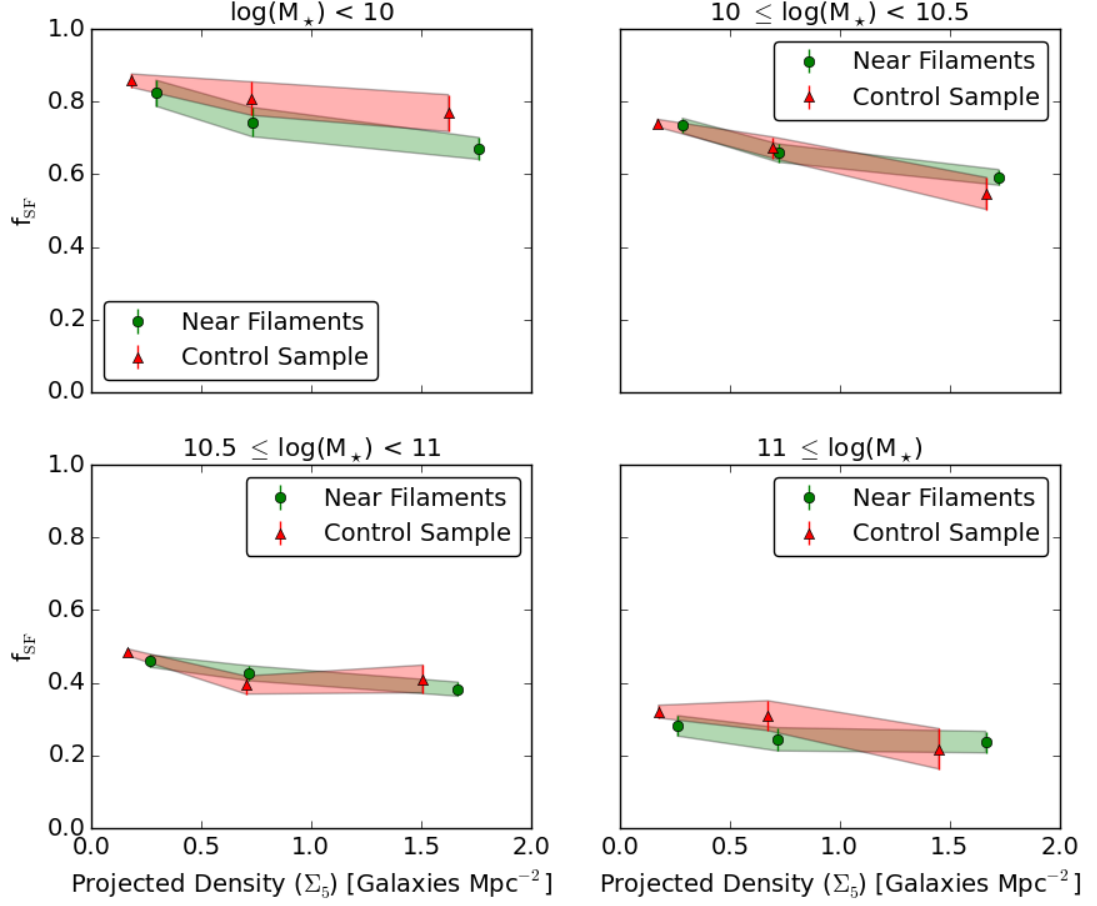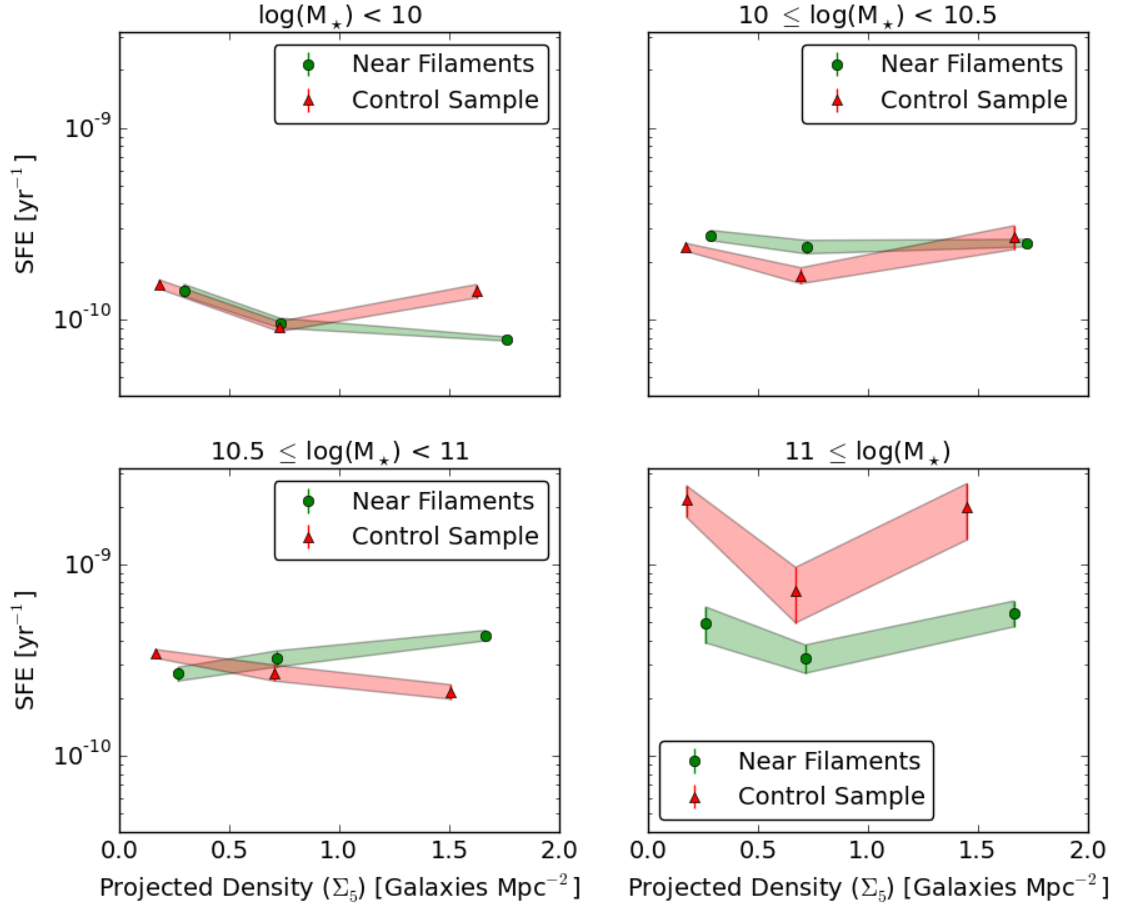
Fig. 5.2: The SFE as a function of projected density for the near filament (green circles) and control sample (red triangles) in different stellar mass bins. The shaded regions are the 1σ uncertainties that have been propagated from the H I mass uncertainty measured in Chapter 4.4. The SFE increases as a function of stellar mass, making the more massive galaxies the quickest at converting cold gas to stars in both samples. There is significant scatter between the SFE and projected density, showing no clear trend. In the stellar mass bin $\log(M_\star / M_\odot) \geq 11$, filament galaxies have a systematically lower SFE. This difference is significant by 4.0 and 3.6σ at projected densities of 0.25 and 1.25 galaxies Mpc^{-2}. We suggest this is evidence of massive filament galaxies having their star formation quenched.

Hı mass that can vary 4 orders of magnitude for a given stellar mass, reflecting the complexities that determine the Hı content of a galaxy (Maddox et al., 2015). This large scatter in Hı mass carries through to the ∼0.4 dex scatter of SFE and is most likely responsible for observing no trend in the SFE as a function of projected density.

For galaxies with $\log(M_\star / M_\odot) > 11$ the SFE as a function of projected density is systematically lower than the corresponding field galaxies. This is significant by 3.6 and 4.0σ at projected densities of 0.25 and 1.45 galaxies Mpc^{-2}. Either a low SFR or a high Hı mass (or combination of) can result in a low SFE. In Chapter 4, we find this subset of galaxies to have more Hı than the control sample. As the star forming fraction is the same for both samples, we attribute the lower SFE for galaxies near filaments to being richer in Hı than the control sample. This is consistent with the interpretation of high SFEs by Schiminovich et al. (2010).

In this mass range, galaxies near filaments have more gas but are actively forming stars at the same rate as the field galaxies. One interpretation is a subtle quenching mechanism operating in filaments that prevents some cold gas collapsing into stars, generally agreeing with the prior literature (Chen et al., 2015b; Guo et al., 2015; Alpaslan et al., 2016; Martínez et al., 2016). However, there is no known mechanism that prevents Hı gas from forming stars without heating or stripping it. Therefore, the most likely scenario to explain these findings is that the additional Hı gas in filament galaxies is too diffuse and has not reached the critical density to collapse and form stars. The extra Hı contained in the galaxies may require an external mechanism to trigger star formation. The scenario that best explains our results suggest that galaxies in filaments are attached to the cosmic web and have the ability to accrete cold gas from the IGM. With sufficient time in the filaments, this accretion can lead to a slight enhancement of diffuse cold gas. The gas does not collapse to form stars unless the galaxies experience a strong (e.g. tidal) interaction that could shock the gas. This would result in a brief starburst similar to those observed in filaments feeding clusters (e.g. Porter et al., 2008; Mahajan et al., 2012) and would naturally explain galaxies being pre-processed in groups prior to entering clusters (e.g. Mahajan, 2013; Hess & Wilcots, 2013; Haines et al., 2015). The interactions would be strong enough to detach the galaxy from the cosmic web, preventing further accretion of cold gas and resulting in its star formation being quenched (Aragon-Calvo et al., 2016).

5.7 Summary

Using 6dFGS and WISE we compare the fraction of star forming galaxies and the star formation efficiency of galaxies near filaments to galaxies in a control sample far from filaments. The two samples are the same as those created and used in Chapter 4 with a minimum of 85% successfully matched to detections in the ALLWISE catalogue with reliable photometry. SFRs used to measure the fraction of star forming galaxies originate from WISE *gmag* or $11''$ aperture photometry and this was combined with the H I masses from Chapter 4 to measure the star formation efficiency. Again, we separate the galaxies in to subsamples of stellar mass and projected density to disentangle the possible star formation quenching mechanisms. We find that:

- The fraction of star forming galaxies is strongly correlated with stellar mass, where low mass galaxies have high fractions of star forming galaxies compared to massive galaxies. This translates to low mass galaxies having the highest SFR relative to their mass. A less significant correlation is observed between the fraction of star forming galaxies and projected galaxy density, where the fraction of star forming galaxies decrease with increasing projected densities.

- We observe no difference in the fraction of star forming galaxies as a function of projected density between the near filament and control sample in all stellar mass bins. This implies the average SFR of these galaxies are uniform irrespective of large scale environment once stellar mass and local density are accounted for. Unlike the recent work in the literature, there is no evidence for quenching occurring in filaments. Typically, the quenching signature is weak in filaments and it is likely that the fraction of star forming galaxies does not have the required sensitivity to directly detect it.

- The SFE correlates with stellar mass but not with projected density. Low mass galaxies are not as efficient at converting cold gas to stars as high mass galaxies. The large scatter in the SFE is attributed to the wide range of the H I-to-stellar mass relation and is most likely responsible for no observed connection to a galaxay's local environment.

- Galaxies near filaments with a stellar masses $\log(M_\star) \geq 11$ $M_\odot$ have a systematically lower SFE as a function of projected density than the same mass galaxies in the control sample. This difference is most pronounced at projected

densities of $\Sigma_5 = 0.25$ and 1.45 galaxies Mpc^{-2}, where the statistical significance is 3.6 and 4.0σ. The lower SFE in filament galaxies is attributed to a higher Hı mass than field galaxies as both samples have the same fraction of star forming galaxies.

- We propose a scenario where filament galaxies attached to the cosmic web can accrete additional cold gas compared to field galaxies. The gas is too diffuse to form stars unless an external trigger, such as strong tidal interactions, shock the gas and cause a brief starburst. This scenario is consistent with pre-processing occurring in groups contained in filaments as the result of these interactions would detach the galaxies from the cosmic web and quench its star formation.

CHAPTER 6

Conclusions

The aim of this thesis was to determine the effect that cosmological environment has on the properties of galaxies. Specifically, we have identified signatures of galaxy pre-processing through interactions between the Hɪ content and star formation activity of galaxies with filaments. Using two separate but complementary approaches, we have studied the mechanisms driving galaxy evolution in the cosmic web beyond the known effects of stellar mass and local galaxy density.

The first approach asks:

- What are the properties of cluster galaxies during a minor merger?

- Can a minor merger transform cluster galaxies?

We addressed these questions in Chapter 2 by conducting a detailed case study of the galaxy cluster A1664, located at a cosmic web node.

From multi-wavelength observations of A1664, we use BRI photometry to measure the galaxy properties and X-ray imaging to quantify the ICM morphology. The asymmetric morphology of the ICM and cold front identified in the cluster core from the temperature map indicate strong evidence of a recent minor merger. Using adaptive smoothing on the 2D spatial distribution of the cluster galaxies, we identified the location of the remanent group. We applied a CAS, M_{20} and Gini morphological analysis to the cluster galaxies and find there are significantly (3.7σ) more asymmetric galaxies in the inner, dense region of the cluster. Radial colour profiles and blue fractions were measured for the cluster galaxies and the results are consistent with the morphology-density relation suggesting there is no unique environmental effect in A1664 that has enhanced galaxy transformations.

Our findings from Chapter 2 favour galaxy pre-processing. The higher fraction of asymmetric galaxies in the inner parts of the cluster suggests that galaxies are currently being morphologically transformed due to an increased rate of tidal interactions. If these galaxies contained cold gas we would expect them to be undergoing

a starburst. However, no measurement of blue fractions or colour profiles supported evidence of galaxies experiencing a starburst in the inner regions of the cluster. Therefore, all cluster galaxies must be gas poor and the star formation of the infalling group was quenched prior to interacting with the majority of the cluster galaxies. Overall, a minor cluster merger has little effect on the observable properties of cluster galaxies.

The second approach asks:

- Can we detect evidence for HI interactions between a galaxy and the gaseous medium of filaments?

- What role do filaments play with the galaxy HI reservoir?

- What fraction of filament galaxies are forming stars and how efficiently does it convert HI to stars?

In anticipation of extracting a group and filament catalogue to address these questions, we created two mock catalogues of 6dFGS in Chapter 3.

We used TAO to construct a SHAM and a SAGE mock catalogue of 6dFGS to calibrate the FoF linking lengths for extracting a group (and filament) catalogue. The mocks were constructed to mimic the 6dFGS selection function to account for the flux limits and completeness maps of the survey. Both mocks reproduce the magnitude and redshift distributions to an acceptable level. As the FoF algorithm quantifies galaxy groups through the positions and redshifts of individual galaxies, it is essential for the spatial distribution of the mocks to match the survey. We measured the projected clustering using the two-point correlation function and find the SHAM mock underestimates the clustering at all scales and turns over at a projected distance of $0.3\,\mathrm{Mpc}\,\mathrm{h}^{-1}$. The projected clustering of the SAGE mock matches 6dFGS at scales down to $0.3\,\mathrm{Mpc}\,\mathrm{h}^{-1}$ where it turns over and underestimates the clustering as well.

The outcomes from Chapter 3 have highlighted some important gaps between observations and simulations. Previous implementations of SHAM have reproduced the clustering that matched observations and it is unclear why the clustering of our SHAM mock is underestimated at all projected distances. The SAGE mock may be useable to calibrate the FoF linking lengths in its current state, although we need to understand why it is turning over at small scales. A technique that creates a successful mock and group 6dFGS catalogue can be directly applied to Taipan (da Cahuna et al. in prep) the most comprehensive spectroscopic survey ever undertaken in the southern hemisphere.

We then defined the cosmic web in 6dFGS using a geometric algorithm and we address the questions of the second approach in Chapter 4 and 5.

In Chapter 4 we delineated filament backbones in 6dFGS using DisPerSE and created a near filament and control sample of galaxies. Using the optical positions and redshifts, we extracted H$\textsc{i}$ spectra from HIPASS and measured the H$\textsc{i}$ fraction through spectral stacking. We then split the near filament and control samples in to stellar mass and projected density subsamples to normalise the effects they have on H$\textsc{i}$ to disentangle what influences cold gas in galaxies. For galaxies with stellar masses $\log(M_\star) \leq 11$ M$_\odot$, all H$\textsc{i}$ fractions as a function of projected density are statistically indistinguishable between galaxies near filaments and the control sample. Galaxies with stellar masses $\log(M_\star) > 11$ M$_\odot$ have a systematically higher H$\textsc{i}$ fraction near filaments than the control sample. The greatest difference is 0.75 dex, which is 5.5σ difference at mean projected densities of 1.45 galaxies Mpc^{-2}. We suggest this is evidence for massive galaxies accreting cold gas from IGM that gives them an elevated H$\textsc{i}$ content compared to galaxies that do not have access to this supply of cold gas. This supports cold mode accretion where filament galaxies with a large gravitational potential can draw gas from the IGM as they have not (or have more recently) detached from the cosmic web.

The additional H$\textsc{i}$ in massive filament galaxies is best explained as a diffuse component of the H$\textsc{i}$ reservoir. The diffuse H$\textsc{i}$ may not be able to collapse and form stars without an external mechanism to initiate the process. As filaments predominately host groups of galaxies, it is likely that strong tidal interactions with other galaxies could shock the diffuse H$\textsc{i}$, triggering a rapid starburst. This scenario is consistent with previous studies that observe galaxies undergoing a starburst on the outskirts of clusters or in filaments that feed clusters (e.g. Porter et al., 2008; Mahajan et al., 2012).

In Chapter 5 we used WISE photometry to measure SFRs for the same near filament and control samples. The fraction of star forming galaxies and star formation efficiencies were defined as galaxies that satisfy an intermediate SSFR with $\log(\text{SSFR}) > 11$ yr^{-1} and the SFR-to-H$\textsc{i}$-mass ratio respectively. After normalising the effects stellar mass and projected density have the SFR, we used the fraction of star forming galaxies and the SFE to search for evidence of quenching in filament galaxies. In all stellar mass bins, we find the fraction of star forming galaxies as a function of projected density to be statistically indistinguishable from each other between the near filament and control sample. Therefore, no quenching is observed using the fraction

of star forming galaxies. However, quenching in filament galaxies is second-order to stellar mass and projected density effects, meaning the fraction of star forming galaxies may not be sensitive enough to observe any significant difference. For galaxies with stellar masses $\log(M_\star) \leq 11$ M$_\odot$, all SFEs as a function of projected density are statistically indistinguishable between galaxies near filaments and the control sample. Galaxies near filaments with stellar masses $\log(M_\star) > 11$ M$_\odot$ have a systematically lower SFE. The greatest difference is significant by 4.0σ at a mean projected density of 0.25 galaxies Mpc^{-2}. The lower SFE is a result of a higher Hi mass opposed to a lower SFR. The near filament galaxies were previously shown to be Hi rich in comparison to the control sample and both samples have the same fraction of star forming galaxies.

To explain these results, we must consider the Hi content, SFR of a galaxy and the mechanisms that effect them. There is no known mechanism preventing Hi gas from forming stars without heating or stripping. Therefore, filament galaxies are attached to the cosmic web and accrete diffuse gas from the IGM. Quenching occurs when an external mechanism, such as strong tidal interactions from other galaxies, shocks the gas into a starburst and subsequently detaches the galaxy from the cosmic web. As this occurs in filaments, the galaxy would be pre-processed by having its star formation quenched prior to be deposited onto a cluster.

6.1   Future work

There are two components of this work that would benefit from follow up. The first is fully understanding the features of the projected clustering in the TAO mock catalogues. The other is gaining more insight in to our proposed scenario of gas accretion for filament galaxies.

The main attraction of using SHAM is that it has good agreement with the clustering of observational data. However, we find that it underestimates the projected clustering at all projected distances. Low mass galaxies are more weakly clustered than massive galaxies, and it is possible that SHAM is placing under-luminous galaxies in the halos. However, it would need to clarified if this is the cause and why this is occurring. Another possibility is the improper treatment of subhalos as they fall into bigger halos in the simulation. If the circular velocity of a subhalo is used when it has already merged with a bigger halo, the subhalo can be populated with an

144

under-luminous galaxy. We do not believe this is the cause as we used the circular velocity of a subhalo at infall but the details of how subhalos are treated in the simulation will need to be followed up. The common feature in the SHAM and SAGE projected clustering is the turn over at the projected distance of 0.3 Mpc h^{-1}. As this is present in both the mocks and not 6dFGS, we believe this is a feature of the simulation. The spatial resolution of the simulation will be compared to this projected distance to determine if it is responsible for the turn over. If it is, we need to determine if a projected distance of 0.3 Mpc h^{-1} is acceptable minimum distance for measuring groups of galaxies. If the spatial resolution is the cause, then the SAGE mock may be useable in its current form. However, the turn over needs to be understood before we proceed. Another possibility is how the simulation treats mergers. If this is the scale where mergers dominate, how they occur in the simulation may be very different to what happens observationally. All of these avenues need to be investigated to determine what is causing these features in the projected correlation functions. Once understood, one could create a group catalogue from 6dFGS and test pre-processing mechanisms for groups in filaments. This would be achieved by measuring the properties of central and satellite galaxies of groups in filaments and comparing to groups not in filaments. This work can be directly extended to creating mocks for the future Taipan survey.

The other direction for future work lies in more detailed observations of the gas accretion with future instruments. The scenario that we have proposed for filament galaxies accreting diffuse gas from the IGM falls within the framework of the CWD model. It naturally explains galaxy pre-processing in the group environment, however, our evidence is suggestive and more observations are needed. HIPASS has good sensitivity to diffuse gas but has very limited ($\sim$ 15 arcmin) resolution. Ideally, one would use the SKA pathfinders (ASKAP and MeerKAT) to observe a subset of filament and non-filament galaxies. The telescopes being used to test the SKA pathfinders (e.g. BETA and KAT-7) have already shown to be excellent instruments for detecting gas between galaxies in the group environment (e.g. Lucero et al., 2015; Serra et al., 2015; Hess et al., 2015). One could search for more rigorous evidence of IGM gas accretion and test if it is purely a high mass mechanism. Once ASKAP and MeerKAT are fully operational, surveys such as WALLABY (Koribalski, 2012) could be used to apply a similar technique of measuring the average H<small>I</small> content of filament and non-filament galaxies. Building on the work done in this thesis, these instruments will provide more direct detections and better resolution than our current work. These could also be used at higher redshifts to search for cosmic evolution

of gas accretion from filaments. However, a different technique (such as Hα emitters used in Cantalupo et al., 2014) would be required to define filament and non-filament galaxies.

Bibliography

Abadi, M. G., Moore, B., & Bower, R. G. 1999, MNRAS, 308, 947 20

Abazajian, K. N., et al. 2009, ApJS, 182, 543 22, 55, 90

Abell, G. O., Corwin, Jr., H. G., & Olowin, R. P. 1989, ApJS, 70, 1 32

Abraham, R. G., Tanvir, N. R., Santiago, B. X., Ellis, R. S., Glazebrook, K., & van
den Bergh, S. 1996, MNRAS, 279, L47 44

Abraham, R. G., Valdes, F., Yee, H. K. C., & van den Bergh, S. 1994, ApJ, 432, 75
6

Abramson, A., Kenney, J. D. P., Crowl, H. H., Chung, A., van Gorkom, J. H.,
Vollmer, B., & Schiminovich, D. 2011, AJ, 141, 164 20

Aguerri, J. A. L., & González-García, A. C. 2009, A&A, 494, 891 19

Allen, S. W., Fabian, A. C., Edge, A. C., Bohringer, H., & White, D. A. 1995,
MNRAS, 275, 741 32

Allen, S. W., et al. 1992, MNRAS, 259, 67 33

Allison, J. R., Sadler, E. M., & Meekin, A. M. 2014, MNRAS, 440, 696 92

Alpaslan, M., et al. 2014, MNRAS, 438, 177 24, 54, 55, 90, 96

—. 2015, MNRAS, 451, 3249 15, 91, 114, 136

—. 2016, MNRAS, 457, 2287 25, 91, 114, 129, 136, 138

Angulo, R. E., Springel, V., White, S. D. M., Jenkins, A., Baugh, C. M., & Frenk,
C. S. 2012, MNRAS, 426, 2046 22, 90

Aragon-Calvo, M. A., Neyrinck, M. C., & Silk, J. 2016, ArXiv e-prints xi, 25, 26, 92,
111, 113, 116, 129, 136, 138

Aragón-Calvo, M. A., Platen, E., van de Weygaert, R., & Szalay, A. S. 2010a, ApJ,
723, 364 24, 55, 90, 97

Aragón-Calvo, M. A., van de Weygaert, R., Araya-Melo, P. A., Platen, E., & Szalay, A. S. 2010b, MNRAS, 404, L89 22, 90

Aragón-Calvo, M. A., van de Weygaert, R., & Jones, B. J. T. 2010c, MNRAS, 408, 2163 55, 90

Arnaud, K. A. 1996, in Astronomical Society of the Pacific Conference Series, Vol. 101, Astronomical Data Analysis Software and Systems V, ed. G. H. Jacoby & J. Barnes, 17 40

Ascasibar, Y., & Markevitch, M. 2006, ApJ, 650, 102 33

Baldry, I. K., Balogh, M. L., Bower, R. G., Glazebrook, K., Nichol, R. C., Bamford, S. P., & Budavari, T. 2006, MNRAS, 373, 469 1, 8, 15, 18, 90, 128, 133, 136

Baldry, I. K., Glazebrook, K., Brinkmann, J., Ivezić, Ž., Lupton, R. H., Nichol, R. C., & Szalay, A. S. 2004, ApJ, 600, 681 8

Baldry, I. K., Glazebrook, K., & Driver, S. P. 2008, MNRAS, 388, 945 12, 93, 111, 128

Balogh, M., et al. 2004, MNRAS, 348, 1355 1, 8, 15, 18, 21, 31, 90, 101, 128, 133

Bamford, S. P., et al. 2009, MNRAS, 393, 1324 1, 12, 15, 91, 128, 133

Barnes, D. G., et al. 2001, MNRAS, 322, 486 12, 92, 93, 94, 95

Barnes, J. E. 1992, ApJ, 393, 484 19

Barnes, J. E., & Hernquist, L. E. 1991, ApJL, 370, L65 19, 21, 31, 128

Bekki, K. 1999, ApJL, 510, L15 21, 32

Bekki, K., Couch, W. J., & Shioya, Y. 2001, PASJ, 53, 395 19

Bekki, K., Owers, M. S., & Couch, W. J. 2010, ApJL, 718, L27 20

Bell, E. F., & de Jong, R. S. 2001, ApJ, 550, 212 95

Bell, E. F., McIntosh, D. H., Katz, N., & Weinberg, M. D. 2003, ApJS, 149, 289 13

Bell, E. F., et al. 2004, ApJ, 608, 752 8

Benson, A. J., Bower, R. G., Frenk, C. S., Lacey, C. G., Baugh, C. M., & Cole, S. 2003, ApJ, 599, 38 128

148

Berlind, A. A., et al. 2006, ApJS, 167, 1 xiii, 55, 56, 58, 59

Bernyk, M., et al. 2016, ApJS, 223, 9 60

Berrier, J. C., Stewart, K. R., Bullock, J. S., Purcell, C. W., Barton, E. J., & Wechsler, R. H. 2009, ApJ, 690, 1292 32

Bertin, E., & Arnouts, S. 1996, A&AS, 117, 393 35

Bertin, E., Mellier, Y., Radovich, M., Missonnier, G., Didelon, P., & Morin, B. 2002, in Astronomical Society of the Pacific Conference Series, Vol. 281, Astronomical Data Analysis Software and Systems XI, ed. D. A. Bohlender, D. Durand, & T. H. Handley, 228 36

Beutler, F., et al. 2013, MNRAS, 429, 3604 95, 103

Birnboim, Y., & Dekel, A. 2003, MNRAS, 345, 349 18

Biviano, A., Fadda, D., Durret, F., Edwards, L. O. V., & Marleau, F. 2011, A&A, 532, A77 21, 31

Blanton, M. R., & Roweis, S. 2007, AJ, 133, 734 65

Blumenthal, G. R., Faber, S. M., Primack, J. R., & Rees, M. J. 1984, Nature, 311, 517 2

Bond, J. R., Kofman, L., & Pogosyan, D. 1996, Nature, 380, 603 22, 90

Brammer, G. B., et al. 2009, ApJL, 706, L173 8

Brough, S., et al. 2013, MNRAS, 435, 2903 101, 128, 136

Brown, M. J. I., et al. 2014, ApJS, 212, 18 132

Brown, T., Catinella, B., Cortese, L., Kilborn, V., Haynes, M. P., & Giovanelli, R. 2015, MNRAS, 452, 2479 10, 12, 92, 93, 111

Brown, T., et al. 2016, ArXiv e-prints 12

Bruzual, G., & Charlot, S. 1993, ApJ, 405, 538 95

—. 2003, MNRAS, 344, 1000 8, 61

Butcher, H., & Oemler, Jr., A. 1978, ApJ, 219, 18 47

—. 1984, ApJ, 285, 426 47

Caldwell, N., & Rose, J. A. 1997, AJ, 113, 492 21, 32

Calzetti, D. 2001, PASP, 113, 1449 13

—. 2013, Star Formation Rate Indicators, ed. J. Falcón-Barroso & J. H. Knapen, 419
13

Cantalupo, S., Arrigoni-Battaia, F., Prochaska, J. X., Hennawi, J. F., & Madau, P.
2014, Nature, 506, 63 24, 91, 146

Catinella, B., et al. 2010, MNRAS, 403, 683 10, 12, 92, 93, 111

—. 2013, MNRAS, 436, 34 10, 11, 92, 113

Cautun, M., van de Weygaert, R., & Jones, B. J. T. 2013, MNRAS, 429, 1286 24, 97

Cayatte, V., van Gorkom, J. H., Balkowski, C., & Kotanyi, C. 1990, AJ, 100, 604 20

Cen, R. 2011, ApJ, 741, 99 18, 128

Chen, Y.-C., Ho, S., Freeman, P. E., Genovese, C. R., & Wasserman, L. 2015a,
MNRAS, 454, 1140 24, 55, 90, 91, 97, 114, 126

Chen, Y.-C., et al. 2015b, ArXiv e-prints 25, 91, 98, 114, 126, 129, 136, 138

Chung, S. M., Gonzalez, A. H., Clowe, D., Zaritsky, D., Markevitch, M., & Jones,
C. 2009, ApJ, 691, 963 11, 21, 45, 47

Cluver, M. E., et al. 2014, ApJ, 782, 90 xi, 14, 15, 127, 130, 132

Coil, A. L., et al. 2008, ApJ, 672, 153 80

Colless, M., et al. 2001, MNRAS, 328, 1039 22, 55, 90, 94

Committee for a Decadal Survey of Astronomy and Astrophysics. 2010, New Worlds,
New Horizons in Astronomy and Astrophysics (National Academies Press) 1

Condon, J. J. 1992, ARA&A, 30, 575 13

Conroy, C., Gunn, J. E., & White, M. 2009, ApJ, 699, 486 61

Conroy, C., & Wechsler, R. H. 2009, ApJ, 696, 620 62

Conroy, C., Wechsler, R. H., & Kravtsov, A. V. 2006, ApJ, 647, 201 62, 85

Conselice, C. J. 2003, ApJS, 147, 1 x, 6, 7, 44, 50

Cortese, L., Catinella, B., Boissier, S., Boselli, A., & Heinis, S. 2011, MNRAS, 415, 1797 10, 11, 12, 92, 93, 111, 113

Cortese, L., et al. 2016, MNRAS, 463, 170 15

Cowie, L. L., Songaila, A., Hu, E. M., & Cohen, J. G. 1996, AJ, 112, 839 8

Croton, D. J., et al. 2006, MNRAS, 365, 11 17, 128

—. 2016, ApJS, 222, 22 61

Crowl, H. H., Kenney, J. D. P., van Gorkom, J. H., & Vollmer, B. 2005, AJ, 130, 65 20, 128

Davies, L. J. M., et al. 2015, MNRAS, 452, 616 14, 129

de Lapparent, V., Geller, M. J., & Huchra, J. P. 1986, ApJL, 302, L1 90

De Lucia, G., & Blaizot, J. 2007, MNRAS, 375, 2 128

de Vaucouleurs, G. 1959, Handbuch der Physik, 53, 275 4

Dehghan, S., & Johnston-Hollitt, M. 2014, AJ, 147, 52 24, 55

Dekel, A., & Birnboim, Y. 2006, MNRAS, 368, 2 18

Delhaize, J., Meyer, M. J., Staveley-Smith, L., & Boyle, B. J. 2013, MNRAS, 433, 1398 93, 106, 107, 108

Dénes, H., Kilborn, V. A., & Koribalski, B. S. 2014, MNRAS, 444, 667 10, 92, 108

Dénes, H., Kilborn, V. A., Koribalski, B. S., & Wong, O. I. 2016, MNRAS, 455, 1294 10, 92

Devriendt, J. E. G., Guiderdoni, B., & Sadat, R. 1999, A&A, 350, 381 61

Dickey, J. M., & Lockman, F. J. 1990, ARA&A, 28, 215 39

Dolley, T., et al. 2014, ApJ, 797, 125 79

Doyle, M. T., & Drinkwater, M. J. 2006, MNRAS, 372, 977 10, 92, 113

Doyle, M. T., et al. 2005, MNRAS, 361, 34 92, 107, 108

Dressler, A. 1980, ApJS, 42, 565 18, 21, 25, 31, 47, 51, 91

Driver, S. P., et al. 2011, MNRAS, 413, 971 22, 55, 90

Duffy, A. R., Meyer, M. J., Staveley-Smith, L., Bernyk, M., Croton, D. J., Koribalski, B. S., Gerstmann, D., & Westerlund, S. 2012, MNRAS, 426, 3385 115

Edwards, L. O. V., Fadda, D., Frayer, D. T., Lima Neto, G. B., & Durret, F. 2010, AJ, 140, 1891 21, 31

Eke, V. R., et al. 2004, MNRAS, 348, 866 55, 56, 57, 58

Evoli, C., Salucci, P., Lapi, A., & Danese, L. 2011, ApJ, 743, 45 12, 90

Fabello, S., Catinella, B., Giovanelli, R., Kauffmann, G., Haynes, M. P., Heckman, T. M., & Schiminovich, D. 2011a, MNRAS, 411, 993 10, 92, 93

Fabello, S., Kauffmann, G., Catinella, B., Giovanelli, R., Haynes, M. P., Heckman, T. M., & Schiminovich, D. 2011b, MNRAS, 416, 1739 93

Fabello, S., Kauffmann, G., Catinella, B., Li, C., Giovanelli, R., & Haynes, M. P. 2012, MNRAS, 427, 2841 93

Faber, S. M., et al. 2007, ApJ, 665, 265 8, 10

Fabian, A. C. 2012, ARA&A, 50, 455 17

Fabian, A. C., Johnstone, R. M., & Daines, S. J. 1994, MNRAS, 271, 737 17

Fall, S. M., & Efstathiou, G. 1980, MNRAS, 193, 189 18

Fisher, K. B., Davis, M., Strauss, M. A., Yahil, A., & Huchra, J. P. 1994, MNRAS, 267, 927 80

Forero-Romero, J. E., Hoffman, Y., Gottlöber, S., Klypin, A., & Yepes, G. 2009, MNRAS, 396, 1815 55, 90

Forman, R. 1998, Adv, Math. (134, 90) 99

—. 2002, Sém. Lothar. Combin., 48, Art (B48c, 35 pp. (electronic) 2, 7,10, 13, 23) 99

Fraser-McKelvie, A., Brown, M. J. I., Pimbblet, K. A., Dolley, T., Crossett, J. P., & Bonne, N. J. 2016, MNRAS, 462, L11 10

Fruscione, A., et al. 2006, in SPIE Proc., Vol. 6270, Society of Photo-Optical Instrumentation Engineers (SPIE) Conference Series, 62701V 39

Gallagher, III, J. S. 1972, AJ, 77, 568 11

Geha, M., Blanton, M. R., Yan, R., & Tinker, J. L. 2012, ApJ, 757, 85 17

Geréb, K., Morganti, R., Oosterloo, T. A., Guglielmino, G., & Prandoni, I. 2013, A&A, 558, A54 93

Geréb, K., Morganti, R., Oosterloo, T. A., Hoppmann, L., & Staveley-Smith, L. 2015, A&A, 580, A43 93

Gini, C. 1912, Variabilità e mutabilità 6

Giovanelli, R., & Haynes, M. P. 1985, ApJ, 292, 404 11

Giovanelli, R., et al. 2005, AJ, 130, 2598 12

Gómez, P. L., et al. 2003, ApJ, 584, 210 21, 31, 91

Gouguenheim, L. 1969, A&A, 3, 281 11

Guglielmo, V., Poggianti, B. M., Moretti, A., Fritz, J., Calvi, R., Vulcani, B., Fasano, G., & Paccagnella, A. 2015, MNRAS, 450, 2749 128

Gunawardhana, M. L. P., et al. 2013, MNRAS, 433, 2764 xi, 14, 132

Gunn, J. E., & Gott, III, J. R. 1972, ApJ, 176, 1 19, 20, 21, 31, 128

Guo, Q., Tempel, E., & Libeskind, N. I. 2015, ApJ, 800, 112 114, 136, 138

Habib, S., et al. 2012, ArXiv e-prints 90

Hahn, O., Carollo, C. M., Porciani, C., & Dekel, A. 2007, MNRAS, 381, 41 24, 90, 97

Haider, M., Steinhauser, D., Vogelsberger, M., Genel, S., Springel, V., Torrey, P., & Hernquist, L. 2016, MNRAS, 457, 3024 xi, 23

Haines, C. P., et al. 2011, MNRAS, 417, 2831 91

—. 2013, ApJ, 775, 126 32

—. 2015, ApJ, 806, 101 56, 138

Hambly, N. C., Davenhall, A. C., Irwin, M. J., & MacGillivray, H. T. 2001a, MNRAS, 326, 1315 56, 94

Hambly, N. C., Irwin, M. J., & MacGillivray, H. T. 2001b, MNRAS, 326, 1295 56, 94

Heavens, A., Panter, B., Jimenez, R., & Dunlop, J. 2004, Nature, 428, 625 12

Hess, K. M., Jarrett, T. H., Carignan, C., Passmoor, S. S., & Goedhart, S. 2015, MNRAS, 452, 1617 145

Hess, K. M., & Wilcots, E. M. 2013, AJ, 146, 124 11, 138

Hogg, D. W., et al. 2003, ApJL, 585, L5 8

Holwerda, B. W., Pirzkal, N., Cox, T. J., de Blok, W. J. G., Weniger, J., Bouchard, A., Blyth, S.-L., & van der Heyden, K. J. 2011, MNRAS, 416, 2426 xix, 10, 45, 47, 52, 92

Hopkins, A. M., Colless, M., Blake, C., Mould, J. R., Brown, M. J. I., Croom, S. M., Spitler, L., & Tinney, C. 2014, AAO Observer, 8 55

Hopkins, A. M., et al. 2003, ApJ, 599, 971 13

Hopkins, P. F., Somerville, R. S., Hernquist, L., Cox, T. J., Robertson, B., & Li, Y. 2006, ApJ, 652, 864 19

Hopkins, P. F., et al. 2010, ApJ, 715, 202 19

Hotan, A. W., et al. 2014, PASA, 31, e041 12

Huang, S., Haynes, M. P., Giovanelli, R., Brinchmann, J., Stierwalt, S., & Neff, S. G. 2012, AJ, 143, 133 134, 136

Hubble, E. P. 1926, ApJ, 64, 321 1

—. 1936, Realm of the Nebulae x, 1, 4, 5

Huchra, J., Davis, M., Latham, D., & Tonry, J. 1983, ApJS, 52, 89 90

Huchra, J. P., & Geller, M. J. 1982, ApJ, 257, 423 54, 55, 56

Huchra, J. P., et al. 2012, ApJS, 199, 26 22, 90

Hwang, H. S., & Lee, M. G. 2009, MNRAS, 397, 2111 21, 32

Jarrett, T. H., Chester, T., Cutri, R., Schneider, S., Skrutskie, M., & Huchra, J. P. 2000, AJ, 119, 2498 56, 94, 131

Jarrett, T. H., et al. 2013, AJ, 145, 6 14, 130, 132

Johnston, S., et al. 2008, Experimental Astronomy, 22, 151 12

Jonas, J. L. 2009, IEEE Proceedings, 97, 1522 12

Jones, D. H., Peterson, B. A., Colless, M., & Saunders, W. 2006, MNRAS, 369, 25 xiii, 62, 64

Jones, D. H., et al. 2004, MNRAS, 355, 747 55, 94, 95

—. 2009, MNRAS, 399, 683 22, 54, 55, 66, 90, 93, 94, 95

Kaastra, J. S. 1992, Internal SRON-Leiden report, updated version 2 40

Kaiser, N. 1987, MNRAS, 227, 1 24

Kauffmann, G., White, S. D. M., & Guiderdoni, B. 1993, MNRAS, 264, 201 17

Kauffmann, G., White, S. D. M., Heckman, T. M., Ménard, B., Brinchmann, J., Charlot, S., Tremonti, C., & Brinkmann, J. 2004, MNRAS, 353, 713 1, 15, 90, 128, 133

Kauffmann, G., et al. 2003, MNRAS, 341, 33 8, 17

Kennicutt, Jr., R. C. 1998, ARA&A, 36, 189 12, 13, 128

Kennicutt, Jr., R. C., Tamblyn, P., & Congdon, C. E. 1994, ApJ, 435, 22 12, 13

Kereš, D., Katz, N., Fardal, M., Davé, R., & Weinberg, D. H. 2009, MNRAS, 395, 160 18, 24

Kereš, D., Katz, N., Weinberg, D. H., & Davé, R. 2005, MNRAS, 363, 2 18, 24, 92, 111, 113, 116

Kilborn, V. A., Forbes, D. A., Barnes, D. G., Koribalski, B. S., Brough, S., & Kern, K. 2009, MNRAS, 400, 1962 11

Kirkpatrick, C. C., et al. 2009, ApJ, 697, 867 33, 36, 39, 41

Kleiner, D., Pimbblet, K. A., Jones, D. H., Koribalski, B. S., & Serra, P. 2017, MNRAS, 466, 4692 iv, 88

Kleiner, D., Pimbblet, K. A., Owers, M. S., Jones, D. H., & Stephenson, A. P. 2014, MNRAS, 439, 2755 iv, 21, 29

Klypin, A. A., Trujillo-Gomez, S., & Primack, J. 2011, ApJ, 740, 102 61

Knapp, G. R., Kerr, F. J., & Williams, B. A. 1978, ApJ, 222, 800 11

Komatsu, E., et al. 2011, ApJS, 192, 18 2, 94

Konstantopoulos, I. S., et al. 2013, ApJ, 770, 114 21, 56

Koribalski, B., & Dickey, J. M. 2004, MNRAS, 348, 1255 10, 92

Koribalski, B. S. 2012, PASA, 29, 359 12, 93, 115, 116, 145

Koribalski, B. S., et al. 2004, AJ, 128, 16 92

Kormendy, J., & Kennicutt, Jr., R. C. 2004, ARA&A, 42, 603 xi, 15, 16

Lagos, C. d. P., Theuns, T., Stevens, A. R. H., Cortese, L., Padilla, N. D., Davis, T. A., Contreras, S., & Croton, D. 2017, MNRAS, 464, 3850 15

Lah, P., et al. 2007, MNRAS, 376, 1357 12, 93

—. 2009, MNRAS, 399, 1447 12, 93

Landolt, A. U. 1992, AJ, 104, 340 35

Landy, S. D., & Szalay, A. S. 1993, ApJ, 412, 64 80

Larson, R. B., Tinsley, B. M., & Caldwell, C. N. 1980, ApJ, 237, 692 20, 21, 31, 37

Leclercq, F., Jasche, J., & Wandelt, B. 2015, A&A, 576, L17 24, 55, 90, 97

Lemonias, J. J., Schiminovich, D., Catinella, B., Heckman, T. M., & Moran, S. M. 2013, ApJ, 776, 74 12, 18, 90

156

Lewis, I., et al. 2002, MNRAS, 334, 673 21, 31, 91

Liedahl, D. A., Osterheld, A. L., & Goldstein, W. H. 1995, ApJL, 438, L115 40

Lin, L., et al. 2016, ApJ, 817, 97 12, 90, 133

Lintott, C. J., et al. 2008, MNRAS, 389, 1179 6

Lotz, J. M., Jonsson, P., Cox, T. J., & Primack, J. R. 2010, MNRAS, 404, 590 45

Lotz, J. M., Primack, J., & Madau, P. 2004, AJ, 128, 163 6, 44, 50

Lu, T., Gilbank, D. G., Balogh, M. L., & Bognat, A. 2009, MNRAS, 399, 1858 37

Lu, T., Gilbank, D. G., McGee, S. L., Balogh, M. L., & Gallagher, S. 2012, MNRAS, 420, 126 21, 31, 32

Lucero, D. M., Carignan, C., Elson, E. C., Randriamampandry, T. H., Jarrett, T. H., Oosterloo, T. A., & Heald, G. H. 2015, MNRAS, 450, 3935 145

Madau, P., Pozzetti, L., & Dickinson, M. 1998, ApJ, 498, 106 13

Maddox, N., Hess, K. M., Obreschkow, D., Jarvis, M. J., & Blyth, S.-L. 2015, MN-RAS, 447, 1610 12, 138

Mahajan, S. 2013, MNRAS, 431, L117 56, 91, 113, 138

Mahajan, S., Raychaudhury, S., & Pimbblet, K. A. 2012, MNRAS, 427, 1252 21, 31, 91, 138, 143

Maraston, C. 2005, MNRAS, 362, 799 61

Markevitch, M., Sarazin, C. L., & Vikhlinin, A. 1999, ApJ, 521, 526 21, 32

Martínez, H. J., Muriel, H., & Coenda, V. 2016, MNRAS, 455, 127 25, 91, 114, 133, 136, 138

Masters, K. L., et al. 2010, MNRAS, 405, 783 8

McGee, S. L., Balogh, M. L., Bower, R. G., Font, A. S., & McCarthy, I. G. 2009, MNRAS, 400, 937 21, 31, 32

McIntosh, D. H., et al. 2014, MNRAS, 442, 533 8

Mendel, J. T., Ellison, S. L., Simard, L., Patton, D. R., & McConnachie, A. W. 2011, MNRAS, 418, 1409 56

Mendez, A. J., Coil, A. L., Lotz, J., Salim, S., Moustakas, J., & Simard, L. 2011, ApJ, 736, 110 8

Messier, C. 1781, Catalogue des Nébuleuses & des amas d'Étoiles (Catalog of Nebulae and Star Clusters), Tech. rep. 1

Mewe, R., Gronenschild, E. H. B. M., & van den Oord, G. H. J. 1985, A&AS, 62, 197 40

Mewe, R., Lemen, J. R., & van den Oord, G. H. J. 1986, A&AS, 65, 511 40

Meyer, M. J., Zwaan, M. A., Webster, R. L., Schneider, S., & Staveley-Smith, L. 2008, MNRAS, 391, 1712 92

Meyer, M. J., et al. 2004, MNRAS, 350, 1195 92

Meyer, S. A., Meyer, M., Obreschkow, D., & Staveley-Smith, L. 2016, MNRAS, 455, 3136 93

Mihos, J. C., & Hernquist, L. 1996, ApJ, 464, 641 19

Miley, G. K., Perola, G. C., van der Kruit, P. C., & van der Laan, H. 1972, Nature, 237, 269 20

Monet, D. G., et al. 2003, AJ, 125, 984 35

Moore, B., Katz, N., Lake, G., Dressler, A., & Oemler, A. 1996, Nature, 379, 613 19, 31

Moore, B., Lake, G., & Katz, N. 1998, ApJ, 495, 139 19

Muldrew, S. I., et al. 2012, MNRAS, 419, 2670 18

Murphy, D. N. A., Eke, V. R., & Frenk, C. S. 2011, MNRAS, 413, 2288 24, 54, 55, 56, 87, 90, 96

Mutch, S. J., Croton, D. J., & Poole, G. B. 2011, ApJ, 736, 84 10

National Committee for Astronomy. 2016, Australia in the era of global astronomy (Australian Academy of Science) 1

Nelson, D., et al. 2015, Astronomy and Computing, 13, 12 22

Neyrinck, M. C. 2008, MNRAS, 386, 2101 90

Noeske, K. G., et al. 2007, ApJL, 660, L43 8, 12, 128

Novikov, D., Colombi, S., & Doré, O. 2006, MNRAS, 366, 1201 55, 90

Nulsen, P. E. J. 1982, MNRAS, 198, 1007 19, 21, 31

Obreschkow, D., Ma, X., Meyer, M., Power, C., Zwaan, M., Staveley-Smith, L., & Drinkwater, M. J. 2013, ApJ, 766, 137 108

Odekon, M. C., et al. 2016, ApJ, 824, 110 56

Owers, M. S., Couch, W. J., Nulsen, P. E. J., & Randall, S. W. 2012, ApJL, 750, L23 20, 21, 32

Owers, M. S., Nulsen, P. E. J., Couch, W. J., & Markevitch, M. 2009, ApJ, 704, 1349 33

Owers, M. S., Randall, S. W., Nulsen, P. E. J., Couch, W. J., David, L. P., & Kempner, J. C. 2011, ApJ, 728, 27 21, 32

Owers, M. S., et al. 2013, ApJ, 772, 104 40, 41

Palamara, D. P., et al. 2013, ApJ, 764, 31 79

Park, C., Choi, Y.-Y., Vogeley, M. S., Gott, III, J. R., Blanton, M. R., & SDSS Collaboration. 2007, ApJ, 658, 898 1, 12, 15, 91

Peebles, P. J. E. 1980, The large-scale structure of the universe (Princeton: N. J., Princeton Univ. Press) 79

Pen, U.-L., Staveley-Smith, L., Peterson, J. B., & Chang, T.-C. 2009, MNRAS, 394, L6 12, 93

Peng, Y., Maiolino, R., & Cochrane, R. 2015, Nature, 521, 192 20

Peng, Y.-j., et al. 2010, ApJ, 721, 193 17, 128, 136

Pimbblet, K. A. 2005, MNRAS, 358, 256 24, 55, 90

Pimbblet, K. A., Drinkwater, M. J., & Hawkrigg, M. C. 2004, MNRAS, 354, L61 90

Pimbblet, K. A., & Jensen, P. C. 2012, MNRAS, 426, 1632 15, 90

Pimbblet, K. A., Smail, I., Edge, A. C., Couch, W. J., O'Hely, E., & Zabludoff, A. I. 2001, MNRAS, 327, 588 36

Pimbblet, K. A., Smail, I., Edge, A. C., O'Hely, E., Couch, W. J., & Zabludoff, A. I. 2006, MNRAS, 366, 645 32, 36, 37

Pimbblet, K. A., Smail, I., Kodama, T., Couch, W. J., Edge, A. C., Zabludoff, A. I., & O'Hely, E. 2002, MNRAS, 331, 333 37, 39

Platen, E., van de Weygaert, R., & Jones, B. J. T. 2007, MNRAS, 380, 551 24, 55, 90, 97

Poggianti, B. M., Bridges, T. J., Komiyama, Y., Yagi, M., Carter, D., Mobasher, B., Okamura, S., & Kashikawa, N. 2004, ApJ, 601, 197 21, 32

Poggianti, B. M., Smail, I., Dressler, A., Couch, W. J., Barger, A. J., Butcher, H., Ellis, R. S., & Oemler, Jr., A. 1999, ApJ, 518, 576 65

Poggianti, B. M., et al. 2006, ApJ, 642, 188 1, 15, 21, 31, 90, 133

Poole, G. B., et al. 2015, MNRAS, 449, 1454 90

Popping, A., & Braun, R. 2011, A&A, 533, A122 92

Popping, A., Davé, R., Braun, R., & Oppenheimer, B. D. 2009, A&A, 504, 15 22, 90, 91

Porter, S. C., & Raychaudhury, S. 2007, MNRAS, 375, 1409 21, 31

Porter, S. C., Raychaudhury, S., Pimbblet, K. A., & Drinkwater, M. J. 2008, MNRAS, 388, 1152 32, 91, 113, 138, 143

Poudel, A., Heinämäki, P., Tempel, E., Einasto, M., Lietzen, H., & Nurmi, P. 2016, ArXiv e-prints 25, 129, 136

Press, W. H., & Schechter, P. 1974, ApJ, 187, 425 2

Quilis, V., Moore, B., & Bower, R. 2000, Science, 288, 1617 20

Rasmussen, J., Mulchaey, J. S., Bai, L., Ponman, T. J., Raychaudhury, S., & Dariush, A. 2012a, ApJ, 757, 122 31

Rasmussen, J., Ponman, T. J., & Mulchaey, J. S. 2006, MNRAS, 370, 453 20

Rasmussen, J., et al. 2012b, ApJ, 747, 31 11, 21

Reynolds, J. H. 1920, MNRAS, 80, 746 1

Rines, K., Geller, M. J., Kurtz, M. J., & Diaferio, A. 2005, AJ, 130, 1482 21, 31

Roberts, M. S., & Rots, A. H. 1973, A&A, 26, 483 11

Robotham, A. S. G., et al. 2011, MNRAS, 416, 2640 55, 56

Rogstad, D. H., & Shostak, G. S. 1972, ApJ, 176, 315 11

Rohde, D. J., Gallagher, M. R., Drinkwater, M. J., & Pimbblet, K. A. 2006, MNRAS, 369, 2 107

Salim, S. 2014, Serbian Astronomical Journal, 189, 1 127, 133

Salim, S., et al. 2007, ApJS, 173, 267 13, 127, 133

Sandage, A. 1986, A&A, 161, 89 12

Sandage, A., & Visvanathan, N. 1978, ApJ, 225, 742 37

Sauvage, M., Tuffs, R. J., & Popescu, C. C. 2005, SSRv, 119, 313 14

Scannapieco, C., Tissera, P. B., White, S. D. M., & Springel, V. 2008, MNRAS, 389, 1137 17

Schawinski, K., et al. 2014, MNRAS, 440, 889 x, 8, 9, 10

Schaye, J., et al. 2015, MNRAS, 446, 521 22

Schechter, P. 1976, ApJ, 203, 297 2

Schiminovich, D., et al. 2007, ApJS, 173, 315 8, 127, 133

—. 2010, MNRAS, 408, 919 134, 136, 138

Searle, L., Sargent, W. L. W., & Bagnuolo, W. G. 1973, ApJ, 179, 427 12

Serra, P., et al. 2012, MNRAS, 422, 1835 11, 113

—. 2015, MNRAS, 452, 2680 145

Sérsic, J. L. 1963, Boletin de la Asociacion Argentina de Astronomia La Plata Argentina, 6, 41 6

Silk, J. 2011, in IAU Symposium, Vol. 277, Tracing the Ancestry of Galaxies, ed. C. Carignan, F. Combes, & K. C. Freeman, 273–281 2

Silk, J., & Mamon, G. A. 2012, Research in Astronomy and Astrophysics, 12, 917 2

Smith, A. G., Hopkins, A. M., Hunstead, R. W., & Pimbblet, K. A. 2012, MNRAS, 422, 25 55, 90

Smith, J. D. T., et al. 2007, ApJ, 656, 770 14, 132

Smith, R., Davies, J. I., & Nelson, A. H. 2010, MNRAS, 405, 1723 19

Smoot, G. F., et al. 1992, ApJL, 396, L1 22

Sobral, D., Best, P. N., Smail, I., Geach, J. E., Cirasuolo, M., Garn, T., & Dalton, G. B. 2011, MNRAS, 411, 675 128

Sousbie, T. 2011, MNRAS, 414, 350 24, 55, 90, 97, 98

Sousbie, T., Pichon, C., & Kawahara, H. 2011, MNRAS, 414, 384 90, 98

Springel, V., Di Matteo, T., & Hernquist, L. 2005a, MNRAS, 361, 776 2

Springel, V., Frenk, C. S., & White, S. D. M. 2006, Nature, 440, 1137 22, 90

Springel, V., & Hernquist, L. 2003, MNRAS, 339, 312 17

Springel, V., et al. 2005b, Nature, 435, 629 61

Staveley-Smith, L., et al. 1996, PASA, 13, 243 12, 92, 94, 95

Stoica, R. S., Martínez, V. J., Mateu, J., & Saar, E. 2005, A&A, 434, 423 55, 90

Stoica, R. S., Martínez, V. J., & Saar, E. 2010, A&A, 510, A38 90

Swinbank, A. M., et al. 2017, MNRAS, 467, 3140 15

Tabor, G., & Binney, J. 1993, MNRAS, 263, 323 17

Taylor, E. N., et al. 2011, MNRAS, 418, 1587 8

—. 2015, MNRAS, 446, 2144 8, 10

Tempel, E., Kipper, R., Saar, E., Bussov, M., Hektor, A., & Pelt, J. 2014a, A&A, 572, A8 22

Tempel, E., Stoica, R. S., Martínez, V. J., Liivamägi, L. J., Castellan, G., & Saar, E. 2014b, MNRAS, 438, 3465 24, 55, 90, 97, 101

Tielens, A. G. G. M., Peeters, E., Bakes, E. L. O., Spoon, H. W. W., & Hony, S. 2004, in Astronomical Society of the Pacific Conference Series, Vol. 323, Star Formation in the Interstellar Medium: In Honor of David Hollenbach, ed. D. Johnstone, F. C. Adams, D. N. C. Lin, D. A. Neufeeld, & E. C. Ostriker, 135 13

Tinsley, B. M. 1968, ApJ, 151, 547 12

Tonini, C., Bernyk, M., Croton, D., Maraston, C., & Thomas, D. 2012, ApJ, 759, 43 61

Toomre, A., & Toomre, J. 1972, ApJ, 178, 623 19, 21, 31

Treu, T., Ellis, R. S., Kneib, J.-P., Dressler, A., Smail, I., Czoske, O., Oemler, A., & Natarajan, P. 2003, ApJ, 591, 53 20

Verdugo, M., Lerchster, M., Böhringer, H., Hildebrandt, H., Ziegler, B. L., Erben, T., Finoguenov, A., & Chon, G. 2012, MNRAS, 421, 1949 21, 31

Vijayaraghavan, R., & Ricker, P. M. 2013, MNRAS, 435, 2713 21, 32, 50, 52, 56

Visvanathan, N., & Sandage, A. 1977, ApJ, 216, 214 8

Vollmer, B., Cayatte, V., Boselli, A., Balkowski, C., & Duschl, W. J. 1999, A&A, 349, 411 20

von der Linden, A., Best, P. N., Kauffmann, G., & White, S. D. M. 2007, MNRAS, 379, 867 21

von der Linden, A., Wild, V., Kauffmann, G., White, S. D. M., & Weinmann, S. 2010, MNRAS, 404, 1231 1, 12, 15, 18, 32, 90, 133

Wang, J., et al. 2015, MNRAS, 453, 2399 113

Warren, B. E., Jerjen, H., & Koribalski, B. S. 2004, AJ, 128, 1152 10

Weinmann, S. M., van den Bosch, F. C., Yang, X., & Mo, H. J. 2006, MNRAS, 366, 2 20

White, S. D. M., & Rees, M. J. 1978, MNRAS, 183, 341 2, 18, 128

Wolf, C., et al. 2009, MNRAS, 393, 1302 21, 31

Wolf, M. 1908, Publikationen des Astrophysikalischen Instituts Koenigstuhl-Heidelberg, 3, 109 1

Wong, O. I., Meurer, G. R., Zheng, Z., Heckman, T. M., Thilker, D. A., & Zwaan, M. A. 2016, MNRAS, 460, 1106 134, 136

Wong, O. I., Webster, R. L., Kilborn, V. A., Waugh, M., & Staveley-Smith, L. 2009, MNRAS, 399, 2264 92

Wong, O. I., et al. 2006, MNRAS, 371, 1855 92, 95

Wright, E. L., et al. 2010, AJ, 140, 1868 13, 127, 129, 130

Wyder, T. K., et al. 2007, ApJS, 173, 293 8

Wyithe, J. S. B., & Loeb, A. 2003, ApJ, 595, 614 17

Young, L. M., et al. 2014, MNRAS, 444, 3408 11

Yun, M. S., Ho, P. T. P., & Lo, K. Y. 1994, Nature, 372, 530 xi, 11

Zwaan, M. A., Meyer, M. J., Staveley-Smith, L., & Webster, R. L. 2005, MNRAS, 359, L30 12, 92

Zwaan, M. A., et al. 2004, MNRAS, 350, 1210 92